Dissertation

Supernova Neutrino Spectra and Applications to Flavor Oscillations

by

Mathias Thorsten Keil

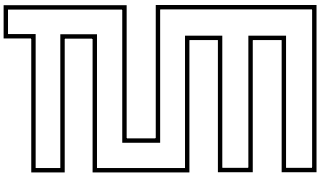

TECHNISCHE
UNIVERSITÄT
MÜNCHEN

Institut für Theoretische Physik T30
Univ.-Prof. Dr. Manfred Lindner

Max-Planck-Institut für Physik
(Werner-Heisenberg-Institut)
Advisor: Dr. habil. Georg G. Raffelt

supported by the grant SFB 375

MAX-PLANCK-GESELLSCHAFT

Institut für Theoretische Physik T30, Univ.-Prof. Dr. Manfred Lindner

Supernova Neutrino Spectra and Applications to Flavor Oscillations

Mathias Thorsten Keil

Vollständiger Abdruck der von der Fakultät für Physik der Technischen Universität München zur Erlangung des akademischen Grades eines Doktors der Naturwissenschaften (Dr. rer. nat.) genehmigten Dissertation.

Vorsitzender:		Univ.-Prof. Dr. F. v. Feilitzsch
Prüfer der Dissertation:	1.	Univ.-Prof. Dr. M. Lindner
	2.	Univ.-Prof. Dr. M. Drees

Die Dissertation wurde am 27.05.2003 bei der Technischen Universität München eingereicht und durch die Fakultät für Physik am 25.06.2003 angenommen.

Summary

We study the flavor-dependent neutrino spectra formation in the core of a supernova (SN) by means of Monte Carlo simulations. Several neutrino detectors around the world are able to detect a high-statistics signal from a galactic SN. From such a signal one may extract information that severely constrains the parameter space for neutrino oscillations. Therefore, reliable predictions for flavor-dependent fluxes and spectra are urgently needed.

In all hydrodynamic simulations the treatment of $\nu_{\mu,\tau}$ and $\bar{\nu}_{\mu,\tau}$ is rather schematic, with the exception of the most recent Garching-Group simulation, where the interaction processes were updated partly based on our results. The interactions commonly included in traditional simulations are iso-energetic scattering on nucleons $\mathrm{N}\nu \rightarrow \nu\mathrm{N}$, scattering on electrons and positrons $\mathrm{e}^{\pm}\nu \rightarrow \nu\mathrm{e}^{\pm}$, and electron-positron pair annihilation $\mathrm{e}^{+}\mathrm{e}^{-} \rightarrow \nu_{\mu,\tau}\bar{\nu}_{\mu,\tau}$. In our Monte Carlo simulations we vary the static stellar background models in addition to systematically switching on and off our set of interaction processes, i.e., recoil and weak magnetism in $\mathrm{N}\nu \rightarrow \nu\mathrm{N}$, scattering on $\mathrm{e}^{\pm}$ and $\nu_{\mathrm{e}}/\bar{\nu}_{\mathrm{e}}$, $\mathrm{e}^{+}\mathrm{e}^{-}$ and $\nu_{\mathrm{e}}\bar{\nu}_{\mathrm{e}}$ annihilation into $\nu_{\mu,\tau}\bar{\nu}_{\mu,\tau}$ pairs, and neutrino bremsstrahlung off nucleons $\mathrm{NN} \rightarrow \mathrm{NN}\nu\bar{\nu}$. As $\nu_{\mu,\tau}$ and $\bar{\nu}_{\mu,\tau}$ sources, $\mathrm{NN} \rightarrow \mathrm{NN}\nu\bar{\nu}$ and $\nu_{\mathrm{e}}\bar{\nu}_{\mathrm{e}} \rightarrow \nu_{\mu,\tau}\bar{\nu}_{\mu,\tau}$ dominate. The latter process has never been studied before in the context of SNe and turns out to be always more important than the traditional $\mathrm{e}^{+}\mathrm{e}^{-}$ annihilation process by a factor of 2–3. For energy transfer, the most important reactions are $\mathrm{N}\nu \rightarrow \nu\mathrm{N}$ with recoil, and scattering on $\mathrm{e}^{\pm}$. Weak magnetism has a very small effect and scattering on ν_{e} and $\bar{\nu}_{\mathrm{e}}$ is negligible.

The charged current reactions $\mathrm{e}^{-}\mathrm{p} \rightarrow \nu_{\mathrm{e}}\mathrm{n}$ and $\mathrm{e}^{+}\mathrm{n} \rightarrow \bar{\nu}_{\mathrm{e}}\mathrm{p}$ dominate for ν_{e} and $\bar{\nu}_{\mathrm{e}}$. In comparing our numerical results for all flavors we find the standard hierarchy of mean energies $\langle\epsilon_{\nu_{\mathrm{e}}}\rangle < \langle\epsilon_{\bar{\nu}_{\mathrm{e}}}\rangle \lesssim \langle\epsilon_{\nu_{\mu,\tau}}\rangle$, with, however, very similar values for $\nu_{\mu,\tau}$ and $\bar{\nu}_{\mathrm{e}}$. The luminosities of $\nu_{\mu,\tau}$ and $\bar{\nu}_{\mathrm{e}}$ can differ by up to a factor of 2 from $L_{\bar{\nu}_{\mathrm{e}}} \approx L_{\nu_{\mathrm{e}}}$. The Garching Group obtains similar results from their self-consistent simulation with the full set of interactions. These results are almost orthogonal to the previous standard picture of exactly equal luminosities of all flavors and differences in mean energies of up to a factor of 2.

Existing concepts for identifying oscillation effects in a SN neutrino signal need to be revised. We present two methods for detecting the earth-matter effect that are rather independent of predictions from SN simulations. An earth-induced flux difference can be measured by the future IceCube detector in Antarctica and a co-detector like Super- or Hyper-Kamiokande. At a single detector with high energy resolution the Fourier transform of the inverse-energy spectrum can reveal the modulations of the spectrum. Both methods are sensitive to the small mixing angle θ_{13} and the neutrino mass hierarchy.

Für meine Eltern

Acknowledgments

Many people contributed to this dissertation with their advice, support, patience, and kindness. I express my gratitude to everyone who helped making this work come true.

Foremost I am indebted to my advisor, Georg Raffelt, not only for proposing the project and thereby getting me into Astroparticle Physics, but even more for his great support and advice in so many ways. I benefited very much from our close and very inspiring collaboration. Also for the proofreading and uncountable valuable suggestions on the manuscript I am very grateful.

The numerical part of this work was only possible with the code that Hans-Thomas Janka had developed and kindly introduced me to. I enjoyed the collaboration with Thomas and appreciate his patience with my questions and his exhaustive answers on all kinds of code- and supernova-related questions. Thomas and his Garching Supernova Group, i.e., Robert Buras and Markus Rampp, contributed very valuable results from their hydrodynamic simulations. I also thank Robert for our many long discussions and his valuable suggestions on parts of the manuscript.

With Amol Dighe I had a wonderful collaboration on the neutrino-oscillation part. But also for all other questions and discussions I found Amol's door wide open. In addition, I thank Amol for improving parts of the manuscript by his proofreading and suggestions. Also for discussions with Michael Kachelrieß, Sergio Pastor, Dimitry Semikoz, and Ricard Tomás I am very grateful.

As important as the support at the institute were all those friends and my family who supported and encouraged me throughout all the years, even when I was far away. For their love and support in any possible way I owe my deepest thanks to my parents as well as my brother and sister. Christoph even fitted some proofreading into his busy conference schedule, thank you.

For your love, support, and encouragement, your patience, your smiles, and everything you did for me, words cannot express my gratitude and love for you, Meike.

Parts of this dissertation have already been published as:

- M. T. Keil, G. G. Raffelt, and H. T. Janka,
  "Monte Carlo study of supernova neutrino spectra formation,"
  Astrophys. J. in press,
  astro-ph/0208035.

- R. Buras, H. T. Janka, M. T. Keil, G. G. Raffelt, and M. Rampp,
  "Electron-neutrino pair annihilation: A new source for muon and tau neutrinos in supernovae,"
  Astrophys. J. **587** (2003) 320 [astro-ph/0205006].

- M. T. Keil, G. G. Raffelt, and H. T. Janka,
  "Supernova Neutrino Spectra Formation,"
  Nucl. Phys. B Proc. Suppl. **118** (2003) 506.

- G. G. Raffelt, M. T. Keil, R. Buras, H. T. Janka, and M. Rampp,
  "Supernova neutrinos: Flavor-dependent fluxes and spectra,"
  astro-ph/0303226.

- A. S. Dighe, M. T. Keil, and G. G. Raffelt,
  "Detecting the neutrino mass hierarchy with a supernova at IceCube,"
  JCAP, in press (2003), hep-ph/0303210.

- A. S. Dighe, M. T. Keil, and G. G. Raffelt,
  "Identifying earth matter effects on supernova neutrinos at a single detector,"
  hep-ph/0304150.

Contents

1 Introduction **1**

2 The Core-Collapse Paradigm **7**
2.1 The Life of a Star: Balancing Forces 7
2.2 The Death of a Massive Star: Core Collapse 10
2.3 Reincarnation: A Proto-Neutron Star Emerges 11
2.4 Self-Consistent Simulations 13
2.5 Flavor-Dependent Neutrino Emission 16

3 Neutrino Interactions **21**
3.1 Beta-Processes 21
3.2 Neutrino-Nucleon Scattering 23
3.3 Weak Magnetism 26
3.4 Bremsstrahlung 27
3.5 Pair Annihilation 28
3.6 Scattering on Electrons and Electron Neutrinos 32
3.7 Other Reactions 34

4 Setting the Stage for Neutrino Transport **35**
4.1 Characterizing Proto-Neutron Stars 35
4.2 Proto-Neutron-Star Profiles 36
4.3 Optical Depth vs. Thermalization Depth 39
4.4 Thermalization Depths in Our Stellar Models 42

5 Characterizing Non-Thermal Neutrino Spectra **49**
5.1 Global Parameters 49
5.2 Analytic Fits 51

6 Relative Importance of Neutral-Current Reactions **57**
6.1 Monte Carlo Setup 57
6.2 Accretion-Phase Model I 59

6.3 Steep Power Law 62
6.4 Shallow Power Law 64
6.5 Summary 64

7 Comparison of All Flavors **67**
7.1 Results from Our Monte Carlo Study 67
7.2 Previous Literature 74
7.3 Spectral Shape 79
7.4 Summary 80

8 Detecting Oscillations of SN Neutrinos **85**
8.1 Oscillations of SN Neutrinos 85
8.2 Detecting Oscillations With Two Distant Detectors 89
8.2.1 The Basic Principle 89
8.2.2 The SN Signal at IceCube 89
8.2.3 The Oscillation Signal at Ice Cube 93
8.2.4 Super- or Hyper-Kamiokande and IceCube 99
8.3 Detecting the Earth-Matter Effect at a Single Detector 101
8.4 Summary 102

9 Discussion and Summary **105**

A Abbreviations **109**

B Monte Carlo Code **111**
B.1 General Concept 111
B.2 Structure of the Code 113

Chapter 1

Introduction

The physics of neutrino oscillations has received tremendous attention during the past years and today oscillations are thought to be established. A large number of experiments has contributed to our present knowledge of the mixing schemes and parameters. For several of the mixing parameters the allowed ranges are known. Within the next few decades the magnitude of the small mixing angle θ_{13} and the question whether the neutrino mass hierarchy is normal or inverted will remain open and can be settled only by future precision measurements at dedicated long-baseline oscillation experiments (Barger et al. 2001, Cervera et al. 2000, Freund, Huber, & Lindner 2001) or the observation of a future galactic supernova (SN).

Along with the interest in neutrino oscillations developed the branch of neutrino astronomy. For the early experiments Raymond Davis Jr. and Masatoshi Koshiba received last year's Physics Nobel Prize "for pioneering contributions to astrophysics, in particular for the detection of cosmic neutrinos" (Nobel e-Museum, 2002). Current and planned experiments will be able to record some 10,000–100,000 neutrinos from a future galactic SN and therefore would provide valuable information on SN physics and neutrino properties (Barger, Marfatia, & Wood 2001, Minakata et al. 2002).

There exists a large number of publications addressing the question, what the neutrino signal of a galactic SN will tell us about neutrino oscillations. With the measurement of such a neutrino signal it would be possible to differentiate between existing oscillation scenarios (Chiu & Kuo 2000, Dighe & Smirnov 2000, Dutta et al. 2000, Fuller, Haxton, & McLaughlin 1999, Lunardini & Smirnov 2001b, 2003, Minakata & Nunokawa 2001, Takahashi & Sato 2002). At the same time, an understanding of neutrino oscillations is crucial for interpreting a recorded signal.

In 1987 neutrinos from a SN were detected for the first and only time (Bionta et al. 1987, Hirata et al. 1987). This signal from SN1987A in the

Large Magellanic Cloud was analyzed taking neutrino oscillations into account (Jegerlehner, Neubig, & Raffelt 1996, Kachelriess et al. 2002, Lunardini & Smirnov 2001a, Smirnov, Spergel, & Bahcall 1994). However, the neutrino detectors that were operational at that time measured only about 20 events connected to SN1987A. With such low statistics, determining SN and neutrino parameters was difficult, but some limits could be obtained.

For the analysis of a SN neutrino signal it would be helpful to have a firm prediction for the neutrino spectra emitted by the core of the SN. Oscillation effects in a neutrino signal depend on the spectral differences between the various flavors. Such spectral differences are obtained by neutrino-transport simulations coupled to self consistent hydrodynamic calculations. In order to get reliable neutrino spectra the way neutrinos are transported in these simulations plays a crucial role. In the past, the transport of ν_μ was very schematic (here and in the following ν_μ stands for either muon or tau neutrinos, or anti-neutrinos, unless stated differently). Spectra obtained for ν_μ in these simulations therefore inherit large uncertainties. However, these uncertainties barely affect the dynamics of the explosion. From the SN model builders point of view, details of ν_μ spectra formation do therefore not play a crucial role. The greatest challenge for numerical models still is to understand how SNe explode. The most elaborate simulations agree rather well on the early stages of the SN mechanism, but do not show explosions.

According to the commonly accepted "delayed-explosion scenario" a massive star with a mass greater than about $8M_\odot$ eventually becomes a core-collapse SN. At the end of its life, such a star has accumulated an iron core of about 1.5 $M_\odot$, close to the Chandrasekhar limit. Once the core mass is greater than the stability limit it collapses within some hundred milliseconds to a proto-neutron star. Due to this collapse a large amount of gravitational binding energy is liberated, but particles cannot escape the dense medium. A shock wave that formed at the edge of the proto-neutron star travels outwards and plows through the still infalling outer layers of the iron core. The disintegration of these infalling iron nuclei consumes the kinetic energy of the shock wave and finally causes it to stall after a few 100 ms. Neutrino emission drains energy from the proto-neutron star and at the same time heats up the region behind the stalled shock wave. This energy transfer causes the shock wave to regain velocity and finally blow off the envelope of the star.

In a crude approximation the proto-neutron star is a blackbody source for neutrinos of all flavors. The flavor dependent differences, that are most important for oscillations, arise due to the flavor dependence of the neutrino-matter interactions. For the case of electron neutrinos (ν_e) and electron anti-neutrinos ($\bar{\nu}_\mathrm{e}$) the dominant reactions are the charged-current interactions with nucleons $\mathrm{e}^- \mathrm{p} \leftrightarrow \nu_\mathrm{e} \mathrm{n}$ and $\mathrm{e}^+ \mathrm{n} \leftrightarrow \bar{\nu}_\mathrm{e} \mathrm{p}$. Since there are more neutrons

than protons in a proto-neutron star, the interactions are more efficient for $\nu_{\rm e}$ and keep $\nu_{\rm e}$ in local thermal equilibrium (LTE) up to larger radii than $\bar{\nu}_{\rm e}$. Therefore the emerging $\bar{\nu}_{\rm e}$ are hotter than the $\nu_{\rm e}$. The other flavors undergo various types of neutral-current interactions that each are of comparable importance. The detailed interplay of these reactions in the context of SNe has been studied for the first time in the present work.

Traditionally, the ν_μ-matter interactions that are implemented in numerical simulations are iso-energetic scattering with nucleons, scattering on electrons and positrons, and electron-positron pair annihilation into $\nu_\mu\bar{\nu}_\mu$ pairs. For several years there have been suggestions on improving these rates. Burrows & Sawyer (1998) and Reddy et al. (1999) calculated the effect of many-body correlations that change the neutrino-nucleon interactions. Weak magnetism even causes different rates for ν_μ and $\bar{\nu}_\mu$ (Horowitz & Li 2000, Horowitz 2002, Vogel & Beacom 1999). A standard simplification in numerical simulations was to take the nucleon mass to be infinite for neutrino-nucleon scattering. However, it has been known for some time that the influence of nucleon recoils in these scattering reactions was not negligible (Janka et al. 1996, Raffelt 2001). An important source term for ν_μ is nucleon bremsstrahlung ${\rm NN} \rightarrow {\rm NN}\nu_\mu\bar{\nu}_\mu$ that even dominates for low energies (Hannestad & Raffelt 1998, Suzuki 1991,1993, Thompson, Burrows, & Horvath 2000). The traditionally included source for ν_μ in hydrodynamic simulations, ${\rm e}^+{\rm e}^- \rightarrow \nu_\mu\bar{\nu}_\mu$, turns out to be rather unimportant. For the first time we showed that electron-neutrino pair annihilation $\nu_{\rm e}\bar{\nu}_{\rm e} \rightarrow \nu_\mu\bar{\nu}_\mu$ is always a factor of 2–3 more important than this traditional process.

In order to study the relative importance of all possible interaction processes and their dependence on a reasonable range of stellar background models we have adapted the Monte Carlo code of Janka (1987, 1991) and added new microphysics to it. We go beyond the work of Janka & Hillebrandt (1989a,b) in that we include the bremsstrahlung process, nucleon recoils and weak magnetism, $\nu_{\rm e}\bar{\nu}_{\rm e}$ pair annihilation into $\nu_\mu\bar{\nu}_\mu$, and scattering of ν_μ on $\nu_{\rm e}$ and $\bar{\nu}_{\rm e}$. With these extensions we investigate the neutrino transport systematically for a variety of medium profiles that are representative for different SN phases. Raffelt (2001) has recently studied the ν_μ spectra-formation problem with the limitation to nucleonic processes (elastic and inelastic scattering, recoils, bremsstrahlung), to Maxwell-Boltzmann statistics for the neutrinos, and plane-parallel geometry. Our present study complements this more schematic work by including the leptonic processes, Fermi-Dirac statistics, and spherical geometry. In addition we apply our Monte Carlo code to the transport of $\nu_{\rm e}$ and $\bar{\nu}_{\rm e}$ and thus are able to compare the flavor-dependent fluxes and spectra.

With the complete set of neutrino interactions we find a situation that

is almost orthogonal to what has been assumed so far. The standard picture concerning SN neutrino fluxes and spectra was an exact equipartition of the neutrino luminosity among all flavors and a strong hierarchy of the mean energies of the different neutrino flavors $\langle\epsilon_{\nu_\mu}\rangle > \langle\epsilon_{\bar{\nu}_e}\rangle > \langle\epsilon_{\nu_e}\rangle$ with a difference of up to a factor of 2 between $\langle\epsilon_{\bar{\nu}_e}\rangle$ and $\langle\epsilon_{\nu_\mu}\rangle$. These assumptions in turn lead to strong oscillation effects in the predicted signal of a galactic SN. Our findings suggest that the difference between $\langle\epsilon_{\bar{\nu}_e}\rangle$ and $\langle\epsilon_{\nu_\mu}\rangle$ is about 10% or less, but the luminosities can differ by a factor of 2 in either direction, depending on the explosion phase.

This new picture is also supported by all hydrodynamic simulations including Boltzmann solvers for the transport of neutrinos. If these simulations use the traditional set of neutrino interactions they find differences between $\langle\epsilon_{\bar{\nu}_e}\rangle$ and $\langle\epsilon_{\nu_\mu}\rangle$ around 20–30%. Very recently the Garching group implemented what we found to be the relevant set of interactions in their two-dimensional hydrodynamic simulation (Buras et al. 2003b). Their findings are equivalent to the results of our Monte Carlo simulation.

For studies of neutrino-oscillation effects in SN neutrino spectra these findings mean a fundamental change of paradigm, because the main focus of these studies are the effects on $\bar{\nu}_e$ and $\bar{\nu}_\mu$. Available detectors will record only $\bar{\nu}_e$ with high statistics. The basic idea was to identify an oscillation effect by comparing characteristics of the observed and the predicted $\bar{\nu}_e$ spectrum. If oscillations were present, one would observe deviations, because the $\bar{\nu}_e$ and $\bar{\nu}_\mu$ spectra would mix. In addition to the fact that the predictions have large uncertainties, these concepts fail once the new findings are taken into account. Therefore different methods are needed.

According to our findings and the most recent results of self-consistent SN simulations, a concept for inferring neutrino-oscillation parameters from the signal of a galactic SN should be based on the flux differences between $\bar{\nu}_e$ and $\bar{\nu}_\mu$ rather than differences in mean energies. With a SN rate in our galaxy of a few per century the concept needs to involve detectors that will be operational for several decades.

With such methods one might be able to determine oscillation parameters that are difficult to obtain by earth-based experiments. If the currently discussed "neutrino factories" and "super beams" are built they will be able to determine neutrino parameters in great detail (Apollonio et al. 2002, Barger et al. 2001, Cervera et al. 2000, Freund, Huber, & Lindner, 2001, Huber et al. 2003, Huber, Lindner, & Winter 2002). Today, it is not clear whether such experiments will become reality. Both concepts can benefit from one another, because detectors being built for earth bases experiments can also serve as SN detectors and results obtained from one concept can be used to improve the other.

In view of our findings, we developed two methods for identifying the earth matter effect in a SN neutrino signal that only depend on robust features of simulation results rather than detailed predictions. The first method involves two neutrino detectors at different sites, such that for one the neutrino path goes through the earth and the other sees the signal "from above." The energy deposited in one detector differs from that in the other if the earth-matter effect is present, due to different original $\bar{\nu}_{\rm e}$ and $\bar{\nu}_{\mu}$ fluxes. Surprisingly, the future high-energy neutrino telescope IceCube at the South Pole, that will begin taking data from 2005, will yield the most accurate signal (Dighe, Keil, & Raffelt 2003a). Due to its unique location, with a co-detector on the northern hemisphere, e.g., in Japan, the setup covers most of the sky. Alternatively, with a single detector one can identify the modulations of the energy spectrum that are induced by the earth-matter effect with the help of a Fourier transform (Dighe, Keil, & Raffelt 2003b). This is a difficult task with the size and energy resolution of available detectors. However, with a detector like Hyper-Kamiokande or a large scintillation detector this is a powerful procedure.

This dissertation is structured as follows. In Chapter 2 we explain the current explosion paradigm that we believe is realized in nature. We then discuss the neutrino-matter interactions that are relevant inside the proto-neutron star in Chapter 3. We put special emphasis on the $\nu_{\rm e}\bar{\nu}_{\rm e}$ process that has never been studied before in the context of SNe. In Chapter 4 we present the stellar profiles that we use in our numerical simulations. We introduce the concept of a "thermalization depth" and apply it to our stellar profiles in order to estimate the relative importance of the interaction processes. For describing the spectra that we obtain from our calculations we use the characteristic quantities and fits that we explicate in Chapter 5. With all the necessary tools in hand we then first describe our numerical results for ν_{μ} in Chapter 6 and then move on to the comparison of all flavors in Chapter 7, where we also give an overview of the previous literature. As an application of our findings we show in Chapter 8 how to identify the earth-matter effect in a detected SN neutrino signal. And finally we summarize our findings in Chapter 9.

Chapter 2

The Core-Collapse Paradigm

Massive stars accumulate iron in their center after several stages of nuclear burning. The iron core becomes unstable once it reaches a certain mass limit and collapses. According to the so called "delayed-explosion mechanism," the collapse is inverted into an explosion and a shock wave travels outwards powered by the energy deposition of the neutrino flux. The neutrinos are emitted by the proto-neutron star that formed in the center.

There exist a number of numerical simulations. Even the most elaborate among these simulations, however, fail to produce explosions. It is an unsettled issue what the missing ingredients are.

With a focus on the neutrino emission, we discuss the various stages of the explosion. Flavor dependent differences in the emitted neutrino spectra arise due to neutrino-matter interactions. Electron neutrinos and electron anti-neutrinos are dominantly produced by charged-current processes. Several neutral current processes govern the transport of the other flavors.

2.1 The Life of a Star: Balancing Forces

During its whole life a star has to balance two possibly fatal effects that work in opposite directions. On one side, there is the gravitational pull, that tries to collapse the star, on the other side the thermal pressure that expands the star. The connection of thermal and gravitational energy is given by the virial theorem. For the time-averaged kinetic energy $\langle E_{\rm kin}\rangle$ and gravitational energy $\langle E_{\rm G}\rangle$ of an atom inside the star the virial theorem is

$$\langle E_{\rm kin}\rangle = -\frac{1}{2}\langle E_{\rm G}\rangle \ . \tag{2.1}$$

By making the star more compact, $\langle E_{\rm G}\rangle$ becomes more negative. Since the temperature is proportional to $\langle E_{\rm kin}\rangle$, it rises as the star's radius shrinks.

Shrinking the star by heating it up, or vice versa, corresponds to a negative heat capacity and stabilizes the star. For a certain stellar radius the gravitational pull is balanced by the thermal pressure.

A star radiates photons and therefore loses energy. By burning just enough of its fuel in order to produce the energy radiated away, the star becomes a stable object. Initially, this fuel is hydrogen, that produces energy in nuclear-fusion reactions to helium. The stronger the gravitational pull, the hotter the star's interior and the more energy is radiated away. Therefore more massive stars burn fuel at a higher rate.

Due to the nuclear-fusion reactions more and more helium collects in the central region. When hydrogen is depleted at the center, the helium eventually reaches high enough density and temperature in order to ignite. Due to the strong temperature dependence of nuclear fusion reactions, helium burning in the central region is spatially well separated from the hydrogen burning that can still continue at the edge of the helium core. The helium fusion process produces again heavier elements that can also start fusion reactions at a later stage. Since the star has to be denser and hotter to ignite the burning of heavier elements it becomes brighter and loses more energy at this stage. Additionally, these burning processes liberate less energy in each reaction. The reaction rate rises drastically. While hydrogen burning can last millions or even billions of years the silicon burning stage usually takes less than a day (see e.g. Herant et al. 1997).

After several stages of nuclear burning the initial composition of helium and hydrogen transformed into an onion-shell structure with heavier elements up to iron-group nuclei forming the star's core (Figure 2.1). For stars with a mass greater than about 8 $M_\odot$ the core mainly consists of ^{56}Fe and ^{56}Ni. Due to silicon burning the iron core eventually reaches a mass close to its Chandrasekhar limit of 1.2–1.5$M_\odot$. Iron cannot ignite and further fuse to heavier elements since it is already the most tightly bound element.

The Chandrasekhar limit is a stability criterion for compact objects like white dwarfs or the iron core of a massive star. Such objects are stabilized by electron degeneracy pressure. The following very basic explanation of the Chandrasekhar limit can be found in Shapiro & Teukolsky (1983). The gravitational energy of a particular electron at radius R is $E_\mathrm{G} \propto -NR^{-1}$ for N gravitating particles. By moving to the center the electron gets lower gravitational energy and therefore occupies an energetically favored state. As long as the electron is non-relativistic its Fermi energy E_F is proportional to the Fermi momentum p_F squared. Therefore, when the electron moves towards the center, $E_\mathrm{F} \propto p_\mathrm{F}^2 \propto N^{2/3}R^{-2}$ rises faster than the potential energy falls. For some radius the total energy $E_\mathrm{G} + E_\mathrm{F}$ assumes a minimum value and the star is in a stable state. When the mass rises and thus the gravitational

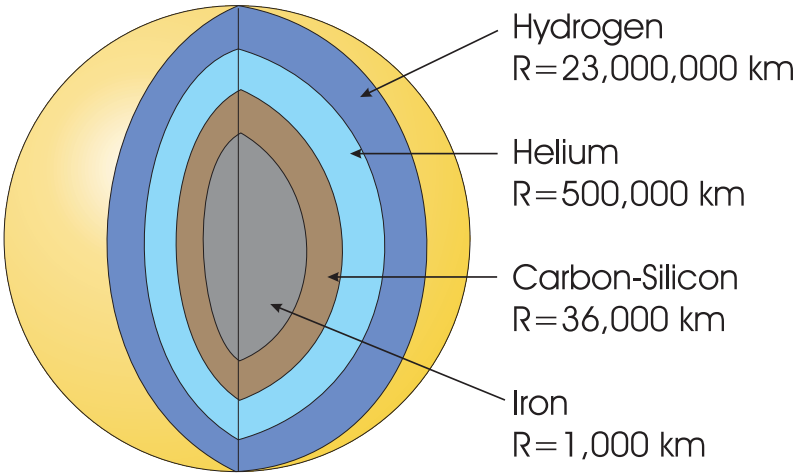

Fig. 2.1.— Schematic picture of a typical progenitor's onion structure (not drawn to scale).

potential gets deeper, also $p_{\rm F}$ has to rise and more and more electrons become relativistic. For relativistic electrons, however, $E_{\rm F} \propto p_{\rm F} \propto N^{1/3}R^{-1}$. The minimum in the total energy disappears. Depending on its mass being above or below the Chandrasekhar limit at that time the star can have two distinct destinies.

- If the mass, $M \propto N$, of the star is below the Chandrasekhar limit the total energy is positive. Therefore the star lowers its energy by expanding, which in turn lowers $p_{\rm F}$, electrons become non-relativistic and the star is stable again.

- For a mass above the Chandrasekhar limit the total energy becomes more and more negative by lowering the radius and the star starts to collapse.

The number of nucleons determines the mass of the iron core. Up to details of the chemical composition of the star, $M = Nm_{\rm nucleon}$. The Chandrasekhar limit is then obtained by solving $E_{\rm F} = E_{\rm G}$ for relativistic electrons and yields $1.5M_{\odot}$.

2.2 The Death of a Massive Star: Core Collapse

As soon as the iron core of a SN progenitor reaches its Chandrasekhar limit the gravitational pull wins over the internal pressure and the core starts to collapse. The rise in density and temperature due to the collapse sets the stage for processes speeding up the infall. Electron captures on nuclei and protons,

$$\begin{aligned} \mathrm{e}^-(Z,A) &\rightarrow \nu_\mathrm{e}\,(Z-1,A) \\ \mathrm{e}^-\mathrm{p} &\rightarrow \nu_\mathrm{e}\,\mathrm{n}\,, \end{aligned} \tag{2.2}$$

become more and more efficient and do not only take away degeneracy pressure, but also drain energy due to the emitted neutrinos that escape the iron core unhindered. Another energy sink is photo disintegration of iron nuclei. Due to the rising temperature inside the core photons start to disintegrate iron nuclei. Within milliseconds the photo disintegration undoes parts of the work of the nuclear-fusion processes, and therefore takes away energy and thermal pressure.

As the collapse of the iron core speeds up, two distinct regions develop (Figure 2.2 left, Figure 2.3 R_ic in phase 1):

- the homologously infalling inner part where the speed is sub-sonic and proportional to radius (Bruenn 1985). This region contracts, keeping its relative density profile, until it reaches nuclear density where the equation of state stiffens drastically. With its enormous inertia the core contracts even beyond the new equilibrium and slightly expands again, usually referred to as the "core bounce."

- the super-sonically infalling outer part. Due to the lower sound speed at larger radii, the matter assumes super-sonic speeds. The infall corresponds therefore basically to a free fall.

A shock wave forms at the interface of the two regions due to the slight reexpansion of the inner core. The core bounce triggers the explosion.

The collapse happens on a time scale of some 100 ms (first phase in Figure 2.3). Therefore, the outer part of the iron core is still infalling and the star's envelope has "not even noticed" that the core collapsed.

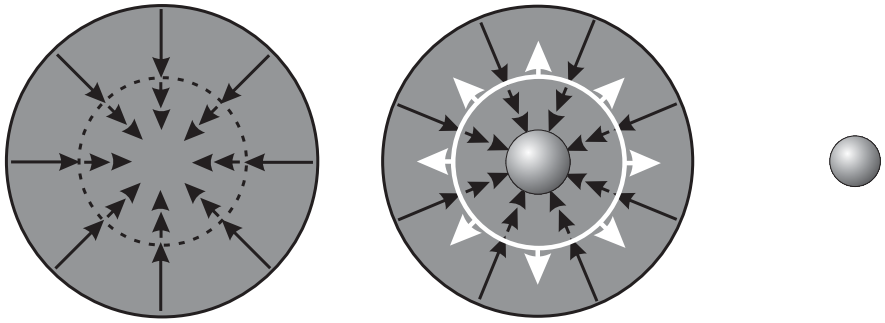

Fig. 2.2.— Cartoon of a collapsing star. *Left:* The initial stage, with the inner homologous and the outer super-sonically infalling region. *Middle:* A hard core has formed, the shock (white) has bounced and travels outwards. The outer layers are still infalling, passing through the shock wave, and then dropping at a slower rate. *Right:* The shock wave has blown off the outer layers of the star; the naked proto-neutron star contracts and cools by neutrino emission.

2.3 Reincarnation: A Proto-Neutron Star Emerges

The shock wave moves outwards through the infalling outer layers of the iron core and loses energy by disintegrating the nuclei it plows through. The nuclear binding energy of $0.1 M_\odot$ of iron is about 1.7×10^{51} erg, comparable to the explosion energy, i.e., approximately 1% of the released 10^{53} erg of gravitational binding energy. The dissociation of iron also liberates protons that capture electrons, and in turn emit electron neutrinos. In the central region of the core, these neutrinos are trapped by the surrounding material. Diffusion is slow compared to the dynamic time scale. As shown in Figure 2.3, the region of neutrino trapping below R_ν builds up during collapse. As long as the shock wave has not passed R_ν neutrino trapping is very efficient, because there are still iron nuclei around and due to coherence effects the cross section for neutrino scattering on nuclei is large compared to that for scattering on nucleons.

Then we enter the second phase of Figure 2.3. The shock passes R_ν and disintegrates the still infalling iron nuclei in the vicinity of R_ν. Suddenly, there are no longer iron nuclei around. Therefore, instead of neutrinos scattering on nuclei, only scattering on free nucleons takes place with a much lower cross section. At the same time, the free protons capture electrons and emit electron neutrinos. These neutrinos in the vicinity of the shock can escape

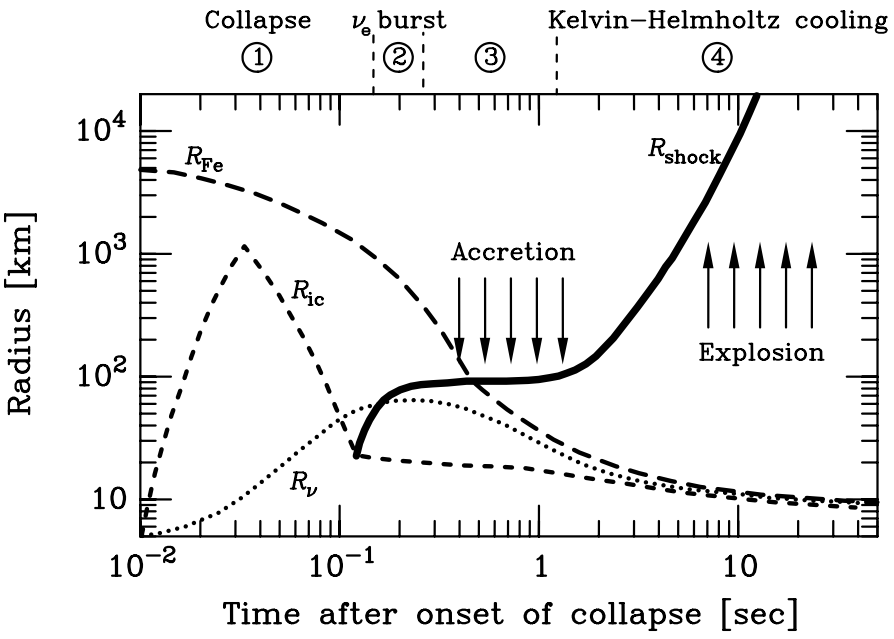

Fig. 2.3.— Schematic plot of the time evolution for various radial zones within the radius of the original iron core. The evolution is divided in four phases: 1. Collapse of the iron core, 2. prompt ν_e burst, 3. accretion phase, and 4. Kelvin-Helmholtz cooling of the proto-neutron star. As long dashes the radius of the iron core (R_{Fe}) is shown, short dashes represent the interface to the inner core (R_{ic}), and dots to the radius below that neutrinos are trapped (R_ν). The solid line, starting shortly after 0.1 s shows the position of the shock (R_{shock}). Adapted from Janka (1993).

freely and cause a sudden peak in the electron-neutrino flux. The luminosity briefly rises to around 10^{54} erg s^{-1}, referred to as the prompt neutrino burst. This also weakens the shock.

Lepton number is approximately conserved inside the core because neutrinos are trapped in the dense matter mainly due to neutrino-nucleon scattering. The processes of Equations (2.2) cause a β equilibrium to develop and a Fermi sea of ν_e builds up. Most of the gravitational binding energy is now stored in the Fermi seas of electrons and electron neutrinos.

During the third stage in Figure 2.3, at a radius of a few 100 km, only about a few 100 ms after bounce, the shock wave stalls due to its energy loss caused by the disintegration of iron nuclei and neutrino emission. Still infalling matter from outer layers of the iron core passes through the standing shock onto the newly formed proto-neutron star, also shown in the middle

panel of Figure 2.2. The edge of the proto-neutron star is at $R_{\rm ic}$ in Figure 2.3, what used to be the interface between the homologously and super-sonically infalling regions of the iron core.

Contraction of the proto-neutron star and the accretion of matter still cause the temperature to rise and the neutrino luminosity increases. In the region between R_ν and the standing shock wave convection takes place. The neutrinos cool the surface of the proto-neutron star. In the last stage of Figure 2.3 the stalled shock wave is revived by the energy that a fraction of the outgoing neutrinos deposit in the region just behind the shock. If only a few per cent of the liberated 10^{53} erg gravitational binding energy are absorbed by the matter behind the standing shock wave, the shock will move outwards again. Finally, this powerful explosion blows off the whole envelope of the star. The naked proto-neutron star remains in the center and cools by neutrino emission. The Kelvin-Helmholtz-cooling phase is displayed as the last phase in Figure 2.3 and the right panel of Figure 2.2.

Due to the initially stalled and afterwards revived shock wave, this mechanism is referred to as a delayed explosion. It was first suggested by Bethe and Wilson (1985). Over the years more and more refined numerical simulations have been developed. The most elaborate among them agree in their result that no explosions are obtained (Buras et al. 2003a, Liebendörfer et al. 2001, Mezzacappa et al. 2001, Rampp & Janka 2000, Thompson, Burrows, & Pinto 2002). It has been stressed by Buras et al. (2003a) that some crucial piece in the game might be missing.

Even if the standard picture is correct, there are also cases when no neutron star is born by the SN explosion. If the progenitor star has a large mass, say greater than 20 $M_\odot$, the evolution of the proto-neutron star can find a sudden end. Due to accretion the mass of the proto-neutron star can exceed its Chandrasekhar limit. The proto-neutron star then collapses and ends up as a black hole, terminating neutrino emission almost at an instant. The details depend on the nuclear equation of state and matter accretion, issues that are not yet settled. A discussion can be found in Beacom, Boyd, & Mezzacappa (2001) and references therein.

2.4 Self-Consistent Simulations

There have been numerical simulations of SNe showing delayed explosions for almost two decades now (Bethe & Wilson 1985, Wilson 1985). These pioneering works obtained robust explosions. With increasing computer power and refined input physics the previous explosions could not be confirmed by other groups. Up to now, only the Livermore group obtains robust explo-

sions (Totani et al. 1998). However, they have to include convection inside the proto-neutron star just below the neutrino spheres by a parameterization of neutron-finger instabilities in order to get explosions (Wilson & Mayle 1988, 1993). This treatment of convection has the effect of enhancing the early neutrino luminosities, which in turn causes more energy to be deposited behind the shock. By neutron-finger convection the neutron rich outer part of the proto-neutron star mixes with the inner part in analogy to salt-finger convection in hot salt water and cold fresh water. However it is controversial whether convection is realized in an actual SN (Burrows 1987, Bruenn, Mezzacappa, & Dineva 1995, Keil, Janka, & Müller 1996, Mezzacappa et al. 1998, Pons et al. 1999). In their two-dimensional simulations, Buras et al. (2003b) find convection of Ledoux type.

All groups performing computer simulations of the hydrodynamics of SNe with a state-of-the-art treatment of the neutrino transport, i.e., Boltzmann solvers, do not get explosions at all (Liebendörfer et al. 2001, Mezzacappa et al. 2001, Rampp & Janka 2000, Thompson, Burrows, & Pinto 2002). Even the most elaborate SN simulations with multi-dimensional hydrodynamics and all relevant microphysics in the neutrino interactions included fail to explode (Buras et al. 2003b). The reason for the models not to explode is obscure.

The delayed-explosion mechanism described in the previous section is in principle found by numerical simulations. The collapse sets in, a shock wave forms, bounces and moves outwards. On its way it loses energy mainly due to the disintegration of nuclei and finally stalls. The simulations also show the appearance of a cooling region above the neutrino sphere where energy is lost due to neutrino radiation. Behind the shock these neutrinos heat the matter, as described above. In the simulations, however, the heating is not sufficient for reviving the shock. Instead it falls back and no explosion takes place. Quite naturally, the main focus of model builders is to find the missing input physics in order to obtain an explosion.

In spite of the numerical failure of obtaining explosions, there are good reasons to believe in the delayed-explosion scenario. Observational hints suggest that the core collapse paradigm should, at least to some extent, be realized in nature. We know that SNe occur after stars have reached their final stage of nuclear burning. For example, SN1987A was a blue supergiant before it exploded. There were neutrinos observed from SN1987A (Bionta et al. 1987, Hirata et al. 1987) about three hours before the first photons were seen, which is a clear evidence for a core collapse. Although there has not been a neutron star identified at the site of SN1987A, for other SN remnants neutron stars have been observed. While the details of the explosion mechanism are still under debate, basic features appear to be robust. If a core

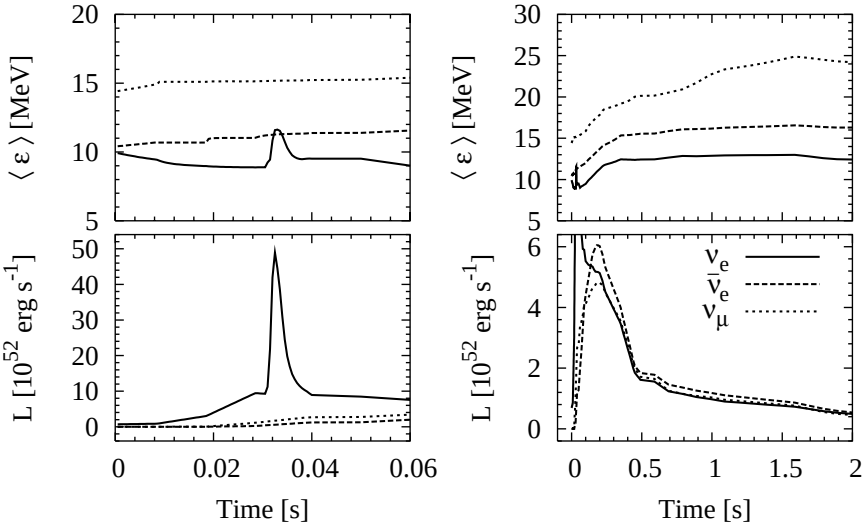

Fig. 2.4.— Numerical results of the first 2 s after core bounce taken from Totani et al. (1998). *Top left:* Only the mean energy of $\nu_{\rm e}$ is affected by the prompt burst. *Top right:* The evolution of mean energies shows the traditional hierarchy. *Bottom left:* The prompt $\nu_{\rm e}$ burst lasting for a few milliseconds. *Bottom right:* Time evolution of the neutrino luminosities, scaled on both axes as compared to the left panel.

collapse occurs the rise of neutrino luminosity and also the prompt neutrino burst are unavoidable as long as the collapse does not continue to form a black hole immediately. An ongoing neutrino emission for several seconds by the proto-neutron star is also not doubted. Throughout this thesis we will assume that the delayed-explosion mechanism is realized in nature.

All numerical simulations agree on this qualitative behavior. An example that we took from Totani et al. (1998) is given in Figure 2.4. Neutrino mean energies and luminosities are shown as functions of time post bounce. Solid lines represent $\nu_{\rm e}$, dashed $\bar{\nu}_{\rm e}$, and dotted ν_{μ}. In the bottom-left panel we show a prominent feature, namely the prompt $\nu_{\rm e}$ burst right after the bounce. The mean energy of $\nu_{\rm e}$ in the top-left panel shows a short rise during the prompt burst. The left panels show the mean energies and luminosities during the first 60 ms and the right panels during the first 2 s after core bounce. Right after the prompt $\nu_{\rm e}$ burst the accretion phase takes over, visible in the rise and fall of luminosities. After the end of the accretion phase deleptonization and cooling of the proto-neutron star powers the neutrino emission. The cooling phase starts at 0.5 s. How the flavor-dependent differences arise is the topic of the next section.

2.5 Flavor-Dependent Neutrino Emission

As soon as the collapse starts the neutrino luminosity increases. In this early stage only electron neutrinos are produced in large amounts due to electron captures on free protons. The protons originate from photo-disintegrated iron nuclei. Since these processes happen most frequently in the dense inner core the major part of the released electron neutrinos is trapped. This trapping is the reason for the Fermi sea of ν_e to develop. When the shock wave passes the region where the star becomes transparent to neutrinos, i.e., the "neutrino sphere," the trapped ν_e can escape. Additionally, the infalling iron nuclei are disintegrated and the electron capture rate in the vicinity of the neutrino sphere goes up. Altogether, this results in the prompt ν_e burst (left panels Figure 2.4).

Neutrinos below the neutrino sphere are still trapped. During the accretion phase, lasting for a few 100 ms, infalling matter deposits energy on the surface of the proto-neutron star, increasing the neutrino luminosities (bottom right panel Figure 2.4). Afterwards, the proto-neutron star still gains energy by contraction. The Fermi seas of electrons and ν_e have a huge amount of energy stored. The star releases this energy over a timescale of several seconds. For the calculation of the Livermore group (Totani et al. 1998) we plotted the deleptonization in Figure 2.5. The lower panel shows the number of leptons per nucleon (Y_L) as a function of radius. From top to bottom the lines correspond to 0.5, 1, 3, 5, 10, and 15 s after bounce. Accordingly, the top panel shows the temperature profile at these times. The maximum moves to lower radii as time increases. At the same time the innermost part heats up.

Even though neutrinos are trapped below their neutrino spheres, due to the steep gradient in Y_L they diffuse outwards. Since electrons are very degenerate in this region, even more degenerate than ν_e, neutrinos will scatter towards regions of lower electron degeneracy. Additionally, when scattering on electrons, neutrinos will always lose energy, since the electron has to end up with an energy above the surface of the electrons' Fermi sea. By this down scattering the electron-neutrino- and electron-degeneracy energy is mainly released as heat. Therefore the temperature maximum follows the deleptonization (see e.g. Raffelt 1996).

The reason why neutrinos are trapped is their frequent interaction with the surrounding matter via various interaction processes. The medium basically consists of neutrons, protons, electrons, positrons, and of course neutrinos. Due to the presence of electrons and positrons, ν_e and $\bar{\nu}_e$ can undergo charged current reactions that are absent for all other flavors. Qualitatively the transport of ν_e and $\bar{\nu}_e$ is therefore different from the transport of ν_μ and

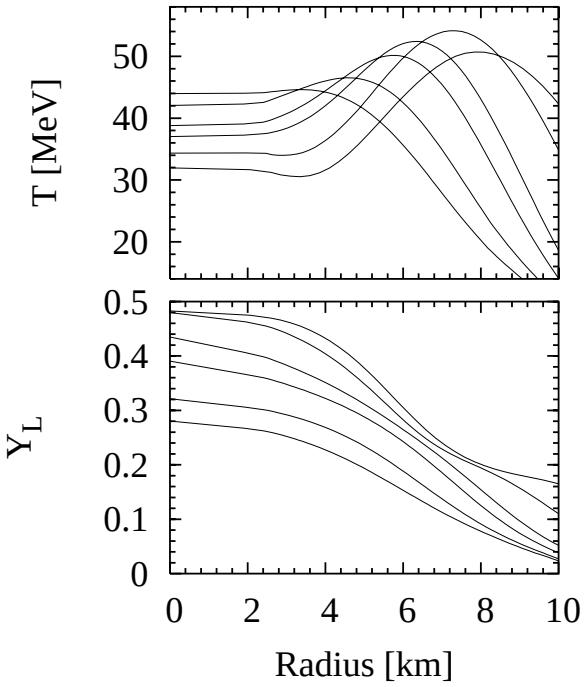

Fig. 2.5.— Deleptonization of a proto-neutron star as obtained by the Livermore group (Totani et al. 1998). *Top:* We show the temperature as a function of radius at 0.5, 1, 3, 5, 10, and 15 s after bounce. With increasing time the peak moves to lower radii. *Bottom:* For the same times we give the lepton number per nucleon. As time increases lepton number gets lower.

ν_τ. To be exact, there is also a small population of muons and anti-muons present. In central regions, where the temperature is maximal, the muon mass is twice the temperature. Since for a non-degenerate particle the mean energy is roughly three times the temperature , $\langle\epsilon\rangle \approx 3\,T$, there is a thermal distribution of muons present in the inner core. However, in the vicinity of the neutrino sphere of ν_μ and $\bar{\nu}_\mu$, where muons would affect the emerging neutrino spectra, the temperature is about 1/10 of the muon mass. Thus muons are strongly suppressed and do not affect the neutrino emission.

Schematically, the emission of $\nu_{\rm e}$ and $\bar{\nu}_{\rm e}$ is displayed in Figure 2.6. In the central region of the proto-neutron star, corresponding to the black shaded area on the left hand side of Figure 2.6, β-processes keep $\nu_{\rm e}$ and $\bar{\nu}_{\rm e}$ in LTE. Due to the decreasing density this reaction becomes inefficient at some radius, defining the neutrino sphere. From that radius neutrinos start streaming freely. Since the β-cross section depends on neutrino energy also the radial position of the neutrino sphere is energy dependent. Therefore it is not pos-

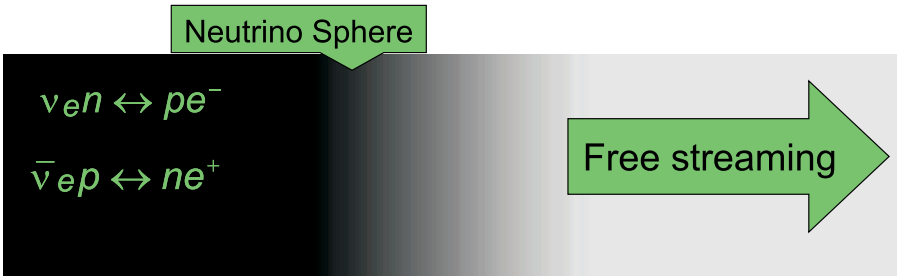

Fig. 2.6.— Schematic picture of the ν_e and $\bar{\nu}_e$ spheres in a proto-neutron star.

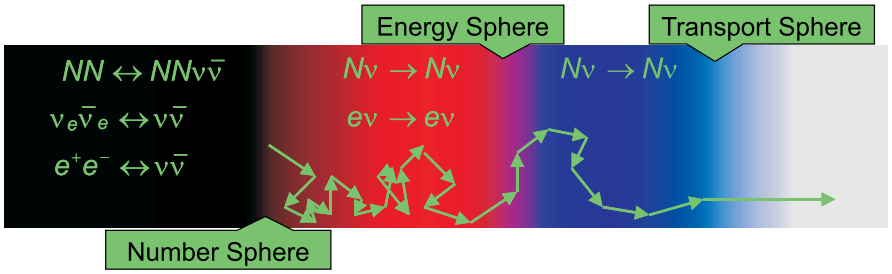

Fig. 2.7.— Same as Figure 2.6 but for ν_μ.

sible to define a unique neutrino-sphere radius. Depending on their energy neutrinos decouple from the proto-neutron star at different radii and therefore different local temperatures. For this reason the spectrum of neutrinos leaving the star does not represent a thermal distribution with a temperature corresponding to the medium temperature at the neutrino sphere that is, anyway, not well defined.

The energy dependence of the interaction processes of ν_e and $\bar{\nu}_e$ is exactly the same. The proto-neutron star, however, contains more neutrons than protons, which leads to a higher absorption rate for ν_e than for $\bar{\nu}_e$. Therefore, the ν_e sphere lies at a larger radius than the $\bar{\nu}_e$ sphere. Since this is true for all neutrino energies the mean energy of emitted ν_e is always less than the mean energy of $\bar{\nu}_e$.

For rough estimates, the neutrino sphere can be considered a blackbody radiating neutrinos. The surface area is thus proportional to the number of emitted neutrinos. Again, the energy dependence of the neutrino-sphere radius makes a more reliable estimate very difficult.

In Figure 2.7 we show a schematic view of the ν_μ transport. Comparing Figures 2.7 and 2.6 tells us that the transport of ν_μ is more complicated. There are no charged current interactions of ν_μ with the medium. Instead,

there is a variety of neutral current interactions that qualitatively differ from one another and, at the same time, are of comparable importance for the transport process. Naively, one would expect that ν_μ decouple deeper inside the star than $\bar{\nu}_\mathrm{e}$, because the neutral-current interaction rates are lower. Then, the mean energy of emerging ν_μ would be higher compared to $\bar{\nu}_\mathrm{e}$ and the flux lower. In reality, the situation is more subtle.

In the inner-most region the ν_μ are kept in LTE by energy exchanging scattering processes and the following pair processes:

- Bremsstrahlung $\mathrm{NN} \leftrightarrow \mathrm{NN}\nu_\mu\bar{\nu}_\mu$
- Neutrino-pair annihilation $\nu_\mathrm{e}\bar{\nu}_\mathrm{e} \leftrightarrow \nu_\mu\bar{\nu}_\mu$
- Electron-positron-pair annihilation $\mathrm{e}^+\mathrm{e}^- \leftrightarrow \nu_\mu\bar{\nu}_\mu$

The radius where these reactions become inefficient defines the number sphere. Outside this sphere no particle creation or annihilation takes place and ν_μ can no longer be in LTE.

Due to the scattering reactions

- $\mathrm{N}\nu_\mu \rightarrow \mathrm{N}\nu_\mu$
- $\mathrm{e}^\pm\nu_\mu \rightarrow \mathrm{e}^\pm\nu_\mu$

there is still energy exchange with the medium. However, the two processes are qualitatively very different. Scattering on $\mathrm{e}^\pm$ is less frequent since there are less $\mathrm{e}^\pm$ than nucleons. On the other hand the amount of energy exchanged in each interaction with $\mathrm{e}^\pm$ is very large compared to the small recoil of nucleons. At the radius, where scattering on $\mathrm{e}^\pm$ freezes out lies the energy sphere. A diffusive regime starts, where neutrinos only scatter on nucleons and therefore exchange little energy in each reaction. This regime is terminated by the transport sphere, defined by the radius at which also scattering on nucleons becomes ineffective and the ν_μ start streaming freely.

Even if we assume that nucleon scattering happens iso-energetically, i.e., no energy can be exchanged outside the thermalization sphere, the mean energy of neutrinos escaping the star is only about 50–60% of those close to the thermalization sphere. Due to its dependence on the square of neutrino energy the nucleon scattering cross section has a filter effect, because it tends to scatter high energy neutrinos more frequently (Raffelt 2001). If one were to specify a neutrino sphere according to the crude approximation of a blackbody radiating neutrinos, it would coincide with the number sphere. Neutrinos leave LTE at the number sphere. The position of the number sphere determines the flux, because neutrino creation is not effective beyond that

radius. The ν_μ flux that passes the number sphere is conserved. On the other hand, the mean energy of ν_μ in this area is still significantly lowered due to scattering processes before the ν_μ leave the star. The mean energy of ν_μ emerging the star is usually found to be larger than that of $\bar{\nu}_\mathrm{e}$. Simulations that include the ν_μ interactions only very approximate obtain a large hierarchy in the mean energies (Figure 2.4). The systematic study of all interaction processes is a major part of this work. Our findings show that the transport of ν_μ is more subtle than previously assumed. Once all interaction processes are taken into account, the mean energies of ν_μ and $\bar{\nu}_\mathrm{e}$ are very similar and might even cross over. The number fluxes can differ by large amounts.

Chapter 3

Neutrino Interactions

We discuss neutrino interactions with the stellar medium that we assume to consist of protons, neutrons, electrons, positrons, and neutrinos of all flavors. The most important reactions for electron neutrinos and electron antineutrinos are charged current processes on nucleons (β-processes). All other flavors undergo neutral-current interactions only.

The neutral-current processes fall into three qualitatively different groups. True LTE is only obtained by the pair creation and annihilation processes, i.e., bremsstrahlung, the $\nu_e\bar{\nu}_e$, and e^+e^- pair processes. Scattering on $e^\pm$ and ν_e, $\bar{\nu}_e$ exchanges large amounts of energy in a single reaction. Neutrino-nucleon scattering qualitatively differs from the other scattering reactions in being more frequent but at the same time exchanging only small amounts of energy in each reaction. Going beyond the traditional iso-energetic nucleon scattering we introduce recoil and weak magnetism.

For the first time, we have investigated the $\nu_e\bar{\nu}_e$ pair process in detail and were able to show that it is far more important than the traditional e^+e^- process. By crossing symmetry the $\nu_e\bar{\nu}_e$ pair process is related to $\nu_\mu\nu_e$ scattering. This scattering process, however, is negligible compared to $e^\pm$ scattering. We have presented these results in a similar form in our publication:
R. Buras, H. T. Janka, M. T. Keil, G. G. Raffelt, and M. Rampp, "Electron-neutrino pair annihilation: A new source for muon and tau neutrinos in supernovae," Astrophys. J. **587** (2003) 320.

3.1 Beta-Processes

For electron neutrinos, the most important neutrino-matter interactions are the β-processes $\nu_e n \leftrightarrow e^- p$ and $\bar{\nu}_e p \leftrightarrow e^+ p$. In principle, also ν_μ can undergo charged current reactions. The central region of the SN core certainly

contains muons, but their presence is commonly neglected in hydrodynamic simulations. In the vicinity of the neutrino sphere the temperature is too low for a thermal distribution of muons. For our simulations it is therefore justified to neglect the charged current reactions of ν_μ.

The squared spin-summed matrix element for neutrino absorption by neutrons is given by (Yueh & Buchler 1976b)

$$\begin{aligned}\sum_{\text{spins}} |\mathcal{M}|^2 &= 32\, G_{\text{F}}^2 \Big[(\alpha+1)^2\, (k_2\cdot k_1)(k_4\cdot k_3) \\ &+ (\alpha-1)^2 (k_2\cdot k_3)(k_4\cdot k_1) + (\alpha^2-1)\, m_{\text{n}}\, m_{\text{p}} (k_1\cdot k_3)\Big]\,. \end{aligned} \tag{3.1}$$

The momenta k_1, k_2, k_3, and k_4 are assigned to the corresponding particles as shown in Figure 3.1; G_{F} is the Fermi coupling constant, $\alpha = C_A/C_V = 1.26$, and m_{n} and m_{p} the masses of the neutron and proton, respectively. Together with phase-space blocking and the phase-space integrations, Equation (3.1) yields the absorption rate or equivalently the inverse of the mean free path (mfp)

$$\begin{aligned}\lambda^{-1} &= \frac{n_{\text{n}}}{(2\pi)^5 2\epsilon_1} \int \frac{d^3k_2}{2\epsilon_2}\frac{d^3k_4}{2\epsilon_4}\frac{d^3k_3}{2\epsilon_3} \sum_{\text{spins}} |\mathcal{M}|^2 \\ &\times f_{\text{n}}(\epsilon_2)\,(1-f_{\text{p}}(\epsilon_4))\,(1-f_{\text{e}}(\epsilon_3))\,\delta^4(k_1+k_2-k_3-k_4)\,, \end{aligned} \tag{3.2}$$

where n_{n} is the neutron density, ϵ_j the energy of particle j, and $f_{\text{n}}(\epsilon_2)$, $f_{\text{p}}(\epsilon_4)$, and $f_{\text{e}}(\epsilon_3)$ are the occupation numbers of neutrons, protons, and electrons, respectively.

For anti-neutrinos we have to interchange neutrons and protons and replace electrons by positrons. For the reverse rate one has to replace blocking factors and the occupation numbers appropriately.

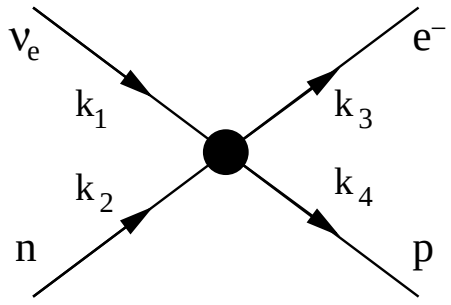

Fig. 3.1.— Feynman diagram for ν_{e} absorption.

Since there are more neutrons than protons present in the SN core, the β-rates for $\nu_{\rm e}$ are always higher than for $\bar{\nu}_{\rm e}$. All interaction processes presented in the remaining sections of this chapter are neutral-current interactions. Due to the smaller coupling constants they are sub-dominant for electron neutrinos. The following sections are more relevant to ν_μ, because charged current reactions do not contribute to the spectra formation of ν_μ. (If not stated differently, ν_μ always refers to $\nu_{\mu,\tau}$ and $\bar{\nu}_{\mu,\tau}$.)

3.2 Neutrino-Nucleon Scattering

The most frequent neutral-current process is neutrino-nucleon scattering and therefore the dominant opacity source for ν_μ. For a neutrino with initial energy ϵ_1 and final energy ϵ_2, the differential cross section is given by

$$\frac{d\sigma}{d\epsilon_2\, d\cos\theta} = \frac{C_A^2(3-\cos\theta)}{2\pi}\, G_{\rm F}^2\, \epsilon_2^2\, \frac{S(\omega,k)}{2\pi}\,, \tag{3.3}$$

with $\omega = \epsilon_1 - \epsilon_2$, k the modulus of the momentum transfer to the medium, and θ the scattering angle. $S(\omega,k)$ represents the dynamical structure function that parameterizes the response of the nuclear medium.

The dynamical structure function includes all effects that change the behavior of the nucleon in the medium, like fluctuations, correlations, and degeneracy effects. The full dynamic structure function covers the whole (ω,k) plane. Therefore it does not only describe neutrino scattering on nucleons but also neutrino bremsstrahlung off nucleons. Both processes are related by crossing symmetry as shown in Figure 3.2, where the grey shaded blob represents the nuclear medium. However, the full structure function is unknown. Common approximations treat the space-like ($\omega^2 \leq k^2$) and time-like ($\omega^2 \geq k^2$) domains on a different footing.

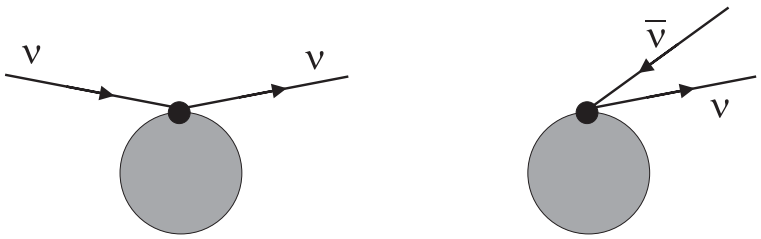

Fig. 3.2.— *Left:* Diagram of neutrino nucleon scattering. The grey shaded blob represents the nuclear medium. *Right:* Bremsstrahlung is obtained by crossing one neutrino leg.

The common simplification of the neutrino-nucleon scattering cross section in traditional SN simulations was to assume that the reaction is isoenergetic, i.e., the nucleons have an "infinite mass" and therefore cannot absorb energy but arbitrary amounts of momentum. In this approximation the structure function is

$$S_{\mathrm{no-recoil}}(\omega, k) = 2\pi\delta(\omega) \; . \tag{3.4}$$

The only multi-particle effect that is usually taken into account is final-state blocking due to the nucleon degeneracy.

More elaborate recent approximations include correlated nucleons and a finite nucleon mass. (Burrows and Sawyer 1998, Reddy, Prakash, and Lattimer 1998, Reddy et al. 1999). These results were calculated in the random-phase approximation, that includes nucleon-spin correlations but not nucleon-spin fluctuations. Therefore, bremsstrahlung is not allowed, because neutrinos couple to the nucleon spin and the emission of a neutrino pair requires a spin flip. In the recent simulations by the Garching group (Rampp and Janka 2002), the correlation effects were taken into account together with recoil.

Some different aspects of multi-particle effects are taken into account by nucleon excitations. The diagrammatic structure is given in Figure 3.3. Raffelt (2001) developed a schematic structure function in this spirit for bremsstrahlung. By crossing a neutrino leg one obtains inelastic scattering, that allows for an energy transfer unrelated to nucleon recoil. Even though, this energy transfer is of the same size as nucleon recoil, the quadratic density dependence of the inelastic scattering process yields lower rates in more dilute regions, where recoil is still effective. In a detailed study Raffelt (2001) shows that once recoil is included in a SN simulation the inelastic scattering contribution can be neglected. For the implementation of ν_μ-nucleon scatter-

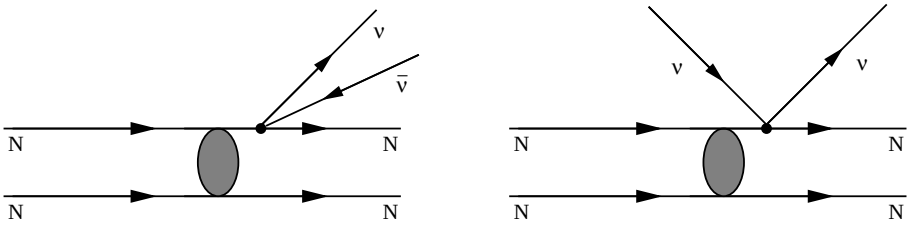

Fig. 3.3.— *Left:* Diagram of neutrino bremsstrahlung off nucleons. This process is subdominant for energy exchange compared to recoil (Raffelt 2001). *Right:* The "crossed process" corresponds to inelastic neutrino-nucleon scattering.

ing Raffelt (2001) provides a structure function for recoiling nucleons that we adapted to our code.

We do not distinguish between protons and neutrons. Since for non-relativistic nucleons the scattering cross section is proportional to $C_V^2 + 3C_A^2$, the vector current ($C_V = -\frac{1}{2}$ for neutrons and $\frac{1}{2} - 2\sin^2\theta_{\rm W}$ for protons) is small compared to the axial component, where we use $|C_A| = 1.26/2$. Neglecting the vector part simplifies the calculations significantly, since otherwise, there are different structure functions for the axial current, the vector current, and the mixed term.

Ignoring nucleon degeneracy effects, the structure function that incorporates nucleon recoils is (Raffelt 2001)

$$S_{\rm recoil}(\omega, k) = \sqrt{\frac{\pi}{\omega_k T}} \exp\left(-\frac{\omega - \omega_k}{4T\omega_k}\right) , \tag{3.5}$$

with $\omega_k = k^2/2m$, m the nucleon mass, and T the medium temperature.

Multiplying Equation (3.3) with the density of nucleons and ignoring phase-space blocking of the essentially non-degenerate nucleons yields the differential rates that can be integrated for obtaining the required energy and angular differential rates. In the case of recoil the numerical integrations are rather tricky because Equation (3.3) is strongly forward peaked, cf. Figure 3.4. In our code we employ the "rejection method" for obtaining the integrated rates (Press et al. 1992).

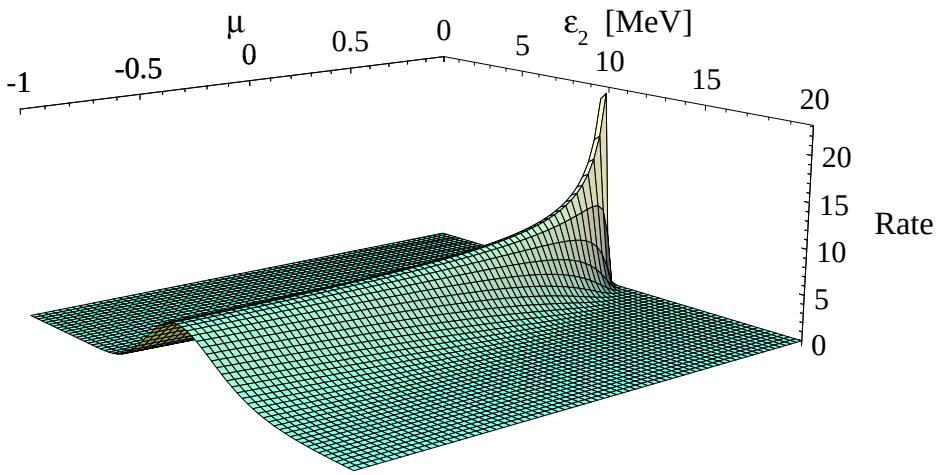

Fig. 3.4.— The differential interaction rate for νN scattering according to Equations (3.3) and (3.5) for initial energy $\epsilon_1 = 10$ MeV as a function of the outgoing energy ϵ_2 and scattering angle $\mu = \cos\theta$.

In the case of ν_e and $\bar{\nu}_e$, scattering on nucleons is less important than the β-processes. Therefore we left the original implementation of our code in the electron-neutrino sector unchanged. The implementation follows Tubbs & Schramm (1975) and can be found in Janka (1987). It basically corresponds to using the structure function given in Equation (3.4).

3.3 Weak Magnetism

Weak magnetism arises as a correction to nucleon scattering due to our schematic treatment of the dynamical structure function. The complete structure function would, of course, contain weak magnetism. The effect is absent if we use the "traditional" approximation of infinite nucleon mass.

As mentioned earlier, there are essentially no muons or taus present in the vicinity of the neutrino sphere. Therefore, ν_μ and $\bar{\nu}_\mu$ are usually treated in the same way. However, the neutrino-nucleon cross section is different for neutrinos and anti-neutrinos once weak magnetism is included. The contributions to the cross section from the anomalous magnetic moment of nucleons and the interference term of the axial and vector current have different signs for neutrinos and anti-neutrinos due to parity violation in the standard model (Horowitz 2002). The interaction rate is higher for neutrinos than for anti-neutrinos.

Neutrinos in the relevant regime of the proto-neutron star have energies on the order of several 10 MeV. To first order in ϵ/m, where ϵ is the neutrino energy and m the nucleon mass, the correction factor to the neutrino-nucleon cross section due to weak magnetism is (Horowitz 2002)

$$1 \pm \frac{4C_A(C_V + F_2)}{C_A^2(3 - \cos\theta)} \frac{k}{m}\,, \tag{3.6}$$

where k is the momentum transfer, F_2 a structure function parameterizing the structure of nucleons. For neutrino-proton scattering $F_2 = \frac{1}{2}(\mu_p - \mu_n) - 2\sin^2(\theta_w)\mu_p \approx 1.019$, where $\mu_{p,n}$ are the magnetic moments of neutron and proton, respectively, and θ_w is the weak mixing angle. For neutrino-neutron scattering, the indices n and p have to be interchanged yielding $F_2 = -0.963$. The upper sign in Equation (3.6) is to be used for neutrinos and the lower sign for anti-neutrinos.

In order to be consistent with Equation (3.3) we keep terms $\propto C_A^2$ and neglect terms $\propto C_V^2$. In addition, we substituted $\epsilon_1 \cos\theta$, taken at the rest frame of the nucleon, by our momentum transfer k. This is correct for forward and backward scattering but only an approximation for other angles. It does not change the angular dependence by much, but in order to keep

our structure-function prescription of the cross section, we cannot multiply factors that depend on k.

The first-order correction factor has the disadvantage that it becomes negative for large momentum transfer. In order to avoid numerical problems we use

$$\left(1 \pm \frac{4C_A(C_V + F_2)}{C_A^2(3 - \cos\theta)} \frac{k}{2m}\right)^2 \tag{3.7}$$

instead, which corresponds to Equation (3.6) up to first order in k/m. For neutrino momenta in the region of the neutrino sphere this approximation induces an error of less than 1%.

3.4 Bremsstrahlung

Neutrino bremsstrahlung off nucleons inside the stellar medium is related to neutrino nucleon scattering by crossing symmetry (Section 3.2). Raffelt (2001) showed that the emerging neutrino spectra from a SN do not sensitively depend on the detailed rate, a fact that we confirm in our simulations. A schematic approach is therefore well justified. Since bremsstrahlung only plays a crucial role for ν_μ we do not consider ν_e and $\bar{\nu}_\mathrm{e}$. We adopt the approach given in Raffelt (2001). The rate for the absorption of a ν_μ by inverse bremsstrahlung $\mathrm{NN}\nu_\mu\bar{\nu}_\mu \rightarrow \mathrm{NN}$ is given by

$$\lambda^{-1} = \frac{C_A^2 G_\mathrm{F}^2}{2} n_B \frac{1}{2\epsilon} \int \frac{d^3\bar{k}}{2\bar{\epsilon}\,(2\pi)^3} f(\bar{\epsilon})\, 24\, \epsilon\, \bar{\epsilon}\, S(\omega)\,, \tag{3.8}$$

where $\omega = \epsilon + \bar{\epsilon}$, n_B is the nucleon density, and $|C_A| = 1.26/2$ as in the scattering case. The over-barred quantities belong to the $\bar{\nu}_\mu$ that is absorbed together with the primary ν_μ.

The energy-differential rate for emission of bremsstrahlung is obtained by adjusting the phase-space blocking:

$$\frac{\mathrm{d}\dot{n}}{\mathrm{d}\epsilon} = \frac{C_A^2 G_\mathrm{F}^2}{2} n_B \frac{\epsilon^2}{2\pi^2} [1 - f(\epsilon)] \int \frac{d^3\bar{k}}{2\bar{\epsilon}\,(2\pi)^3} [1 - f(\bar{\epsilon})]\, 24\, \epsilon\, \bar{\epsilon}\, S(-\omega) \tag{3.9}$$

The heuristic ansatz for $S(\omega)$ given by Raffelt (2001) has the form of a Lorentzian

$$S(\omega) = \frac{2\Gamma}{\omega^2 + \Gamma^2} \frac{2}{1 + \exp(-\omega/T)}\,, \quad \Gamma = \frac{\sqrt{\pi}\,\alpha_\pi^2 n_B\, T}{m^2\sqrt{mT + m_\pi^2}}\,, \tag{3.10}$$

with the constant $\alpha_\pi \approx (2m/m_\pi)^2/4\pi$, where m is the nucleon mass and m_π the pion mass. For carrying out the integration in Equations (3.8) and (3.9) the Γ^2 in the denominator of S can be neglected. A very detailed analysis of this bremsstrahlung rate can be found in Raffelt (2001).

3.5 Pair Annihilation

We now turn to the leptonic source reactions for $\nu_\mu\bar{\nu}_\mu$ pairs, $e^+e^- \rightarrow \nu_\mu\bar{\nu}_\mu$ and $\nu_e\bar{\nu}_e \rightarrow \nu_\mu\bar{\nu}_\mu$. Traditionally, only e^+e^- pair annihilation was implemented in SN simulations. As one part of this dissertation we have for the first time investigated the importance of $\nu_e\bar{\nu}_e$ pair annihilation that turns out to be a factor of 2–3 more important (Buras, Janka, Keil, Raffelt, & Rampp 2003a).

The matrix elements for both processes are identical up to coupling constants while the phase-space integrations only differ by the chemical potentials. After summing over all spins and neglecting the rest masses, the squared matrix element is

$$\sum_{\text{spins}} |\mathcal{M}|^2 = 8\, G_{\text{F}}^2 \left[(C_V + C_A)^2 u^2 + (C_V - C_A)^2 t^2 \right] \tag{3.11}$$

with the Mandelstam variables $t = -2k_1 \cdot k_3$ and $u = -2k_1 \cdot k_4$. The momenta are assigned to the particles as indicated in Figure 3.5. The weak interaction constants for e^+e^- annihilation are

$$C_V = -\frac{1}{2} + 2\sin^2\theta_{\text{W}}\,, \quad C_A = -\frac{1}{2} \tag{3.12}$$

while for $\nu_e\bar{\nu}_e$ annihilation they are

$$C_A = C_V = \frac{1}{2}\,. \tag{3.13}$$

For the interaction rates we have to perform the phase-space integrations, using blocking factors for the final states and occupation numbers for initial-state particles (Hannestad & Madsen 1995, Yueh & Buchler 1976a). Three integrations remain that can not be carried out analytically.

In order to perform the phase-space integrals we have to specify chemical potentials for all interacting particles. Mu- and tau-leptons are almost

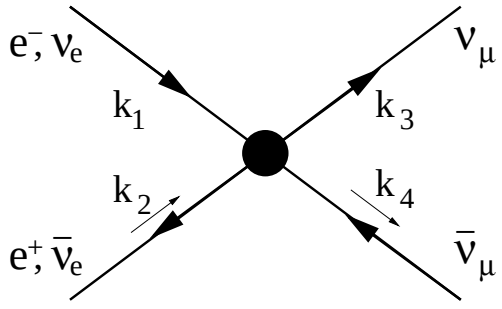

Fig. 3.5.— Pair annihilation processes producing $\nu_\mu\bar{\nu}_\mu$ pairs.

absent in proto-neutron star atmospheres, therefore, chemical potentials of the corresponding neutrinos can only arise due to differences in the neutrino and anti-neutrino interactions, i.e., weak magnetism. This chemical potential builds up dynamically, because anti-neutrinos escape more easily than neutrinos. For the e^+e^- reactions the local value of μ_e can be obtained from ρ, T, and Y_e by inverting

$$\frac{n_{e^-}(\mu_e) - n_{e^+}(-\mu_e)}{n_{\rm baryons}} = Y_e \,, \tag{3.14}$$

where $n_{e^-}(\mu_e)$ and $n_{e^+}(-\mu_e)$ are the number densities of electrons and positrons, respectively. The baryon number density is

$$n_{\rm baryons} = \frac{\rho}{m_n(1-Y_e) + m_p Y_e} \,. \tag{3.15}$$

For ν_e and $\bar{\nu}_e$ the chemical potential is obtained by the relation

$$\mu_{\nu_e} = \mu_e + \mu_p - \mu_n \,, \tag{3.16}$$

with the chemical potentials μ_p and μ_n of protons and neutrons, respectively.

The reason why the $\nu_e\bar{\nu}_e$ pair process is an important source for $\nu_\mu\bar{\nu}_\mu$ pairs is that below the ν_μ number sphere, ν_e and $\bar{\nu}_e$ are basically a part of the stellar medium like $e^\pm$. The energy sphere of ν_μ lies always deeper inside the star than the ν_e and $\bar{\nu}_e$ spheres (Section 4.4). Thus ν_e and $\bar{\nu}_e$ are in LTE and are part of the medium as far as the transport of ν_μ is concerned.

Until very recently e^+e^- annihilation was considered to be the most important leptonic source for ν_μ. In most numerical simulations it is still the only included creation mechanism for the ν_μ flavors. Comparing the rates for SN conditions it is obvious that $\nu_e\bar{\nu}_e$ pairs are more important. In Figure 3.6 we show both leptonic pair rates as a function of their respective degeneracy parameters. The chemical potential of ν_μ was set to zero and ν_e, $\bar{\nu}_e$, and $e^\pm$ are assumed to be in LTE. In the region below the neutrino spheres the degeneracy parameters obey $\eta_{\nu_e} = \eta_e + \eta_p - \eta_n < \eta_e$ and therefore the neutrino pair process is always more important than e^+e^- annihilation.

Another qualitative difference of both rates becomes apparent by looking at the energy-differential production rate. In the case of vanishing degeneracy of $e^\pm$ and ν_e, $\bar{\nu}_e$ the differential production rate $d^2n/d\epsilon dt$ is equal for both ν_μ and $\bar{\nu}_\mu$, as shown in Figure 3.7. In general, however, electrons and electron neutrinos will be significantly degenerate. For the extreme case $\eta_e = \eta_{\nu_e} = 10$ we show the differential production rates in Figure 3.8. In the upper panel both ν_μ and $\bar{\nu}_\mu$ creation rates are very similar for e^+e^- annihilation. This represents the fact that the prefactors u^2 and t^2 in Equation (3.11) are similar,

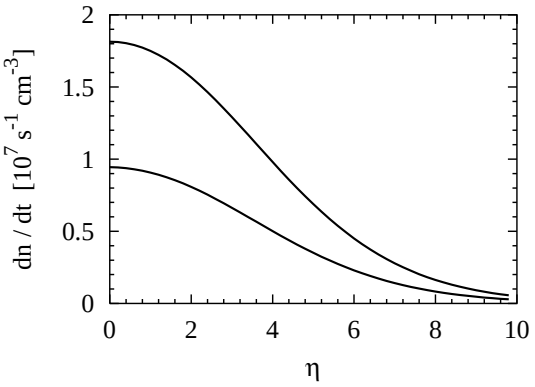

Fig. 3.6.— Pair production rates by the process $\nu_e\bar{\nu}_e \to \nu_\mu\bar{\nu}_\mu$ as a function of η_{ν_e} (upper line) and $e^+e^- \to \nu_\mu\bar{\nu}_\mu$ as a function of η_e (lower line). We used $T = 12$ MeV and $\eta_{\nu_\mu} = 0$.

namely $(C_V + C_A)^2 \approx 0.54^2$ and $(C_V - C_A)^2 \approx 0.46^2$. Comparing the rates for ν_μ and $\bar{\nu}_\mu$, which corresponds to exchanging u and t, then has no big effect.

For the $\nu_e\bar{\nu}_e$ process the situation is different. In this case $(C_V + C_A)^2 = 1$ and $(C_V - C_A)^2 = 0$ and only u^2 contributes. Interchanging $\bar{\nu}_\mu$ with ν_μ corresponds to replacing u^2 by t^2. Therefore, the kinematics for particles and anti-particles are different. Since in the case of $\eta_{\nu_e} \neq 0$ also the distribution functions of particles and anti-particles are different this leads to a difference in the energy dependence of the ν_μ and $\bar{\nu}_\mu$ production rate. The lower panel of Figure 3.8 displays both rates. The numbers of produced ν_μ and $\bar{\nu}_\mu$ are equal, of course.

The reason for the average energy of ν_μ to be larger than of $\bar{\nu}_\mu$ can be understood by looking at the reaction $\nu_e\bar{\nu}_e \to \nu_\mu\bar{\nu}_\mu$ in the center of momentum (CM) frame. The differential cross section is

$$\frac{d\sigma}{d\cos\theta} = \frac{G_F^2}{4\pi}\,\epsilon^2(1+\cos\theta)^2\,, \tag{3.17}$$

where θ is the angle between the ingoing ν_e and the outgoing ν_μ, or equivalently, between the ingoing $\bar{\nu}_e$ and the outgoing $\bar{\nu}_\mu$. Put another way, forward scattering is favored and backward scattering forbidden. This is due to angular momentum conservation. The ingoing ν_e and $\bar{\nu}_e$ have opposite helicities and, in the CM frame, opposite momenta, so that their combined spins add up to 1. The same is true for the outgoing particles so that backward scattering would violate angular momentum conservation. In the rest frame of the medium the ingoing ν_e tends to have energies of the order of its Fermi energy, while the ingoing $\bar{\nu}_e$ tends to have energies of order T. Because for-

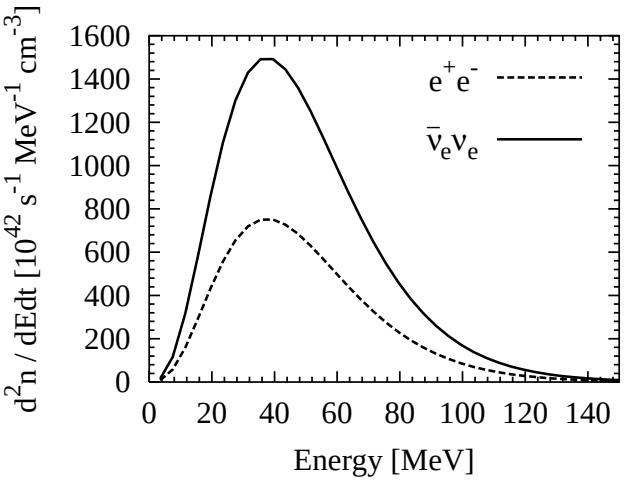

Fig. 3.7.— Differential ν_μ and $\bar{\nu}_\mu$ production rates $\mathrm{d}^2n/\mathrm{d}\epsilon\mathrm{d}t$ vs. neutrino energy for $\eta_\mathrm{e} = \eta_{\nu_\mathrm{e}} = 0$ and $T = 12$ MeV.

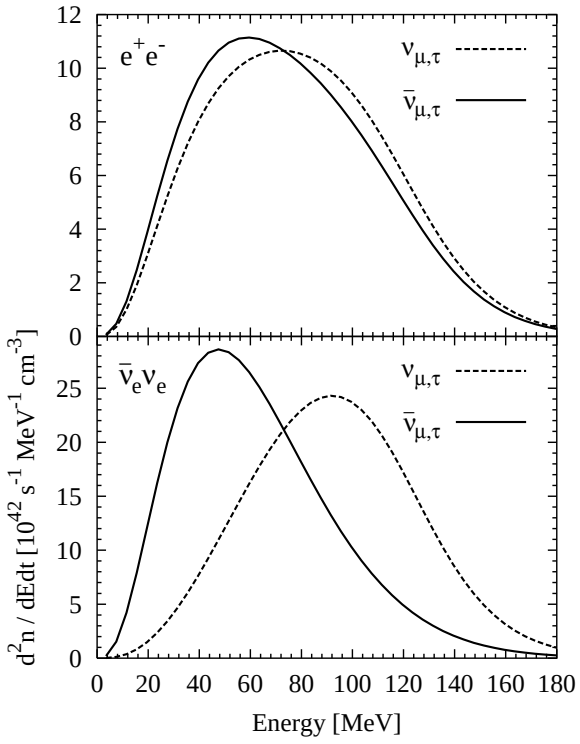

Fig. 3.8.— Differential ν_μ and $\bar{\nu}_\mu$ production rates $\mathrm{d}^2n/\mathrm{d}\epsilon\mathrm{d}t$ for $\eta_\mathrm{e} = \eta_{\nu_\mathrm{e}} = 10$ and $T = 12$ MeV. Upper panel for $\mathrm{e}^+\mathrm{e}^- \to \nu_\mu\bar{\nu}_\mu$, lower panel for $\nu_\mathrm{e}\bar{\nu}_\mathrm{e} \to \nu_\mu\bar{\nu}_\mu$.

ward scattering is favored, the outgoing ν_μ tends to inherit the larger energy of the ingoing ν_e.

The differences of the source spectra, however, do not translate into significant spectral differences of the ν_μ and $\bar{\nu}_\mu$ fluxes emitted from the SN core. While pair annihilations and nucleon bremsstrahlung are responsible for producing or absorbing neutrino pairs and thus their equilibration with the stellar medium below the "neutrino-energy sphere," other processes, notably $\nu_\mu e^\pm$ scattering and nucleon recoils, are more efficient for the exchange of energy between neutrinos and the medium between the equilibration and transport spheres. In our numerical runs we will find in fact that adding the new process to a SN simulation primarily modifies the flux with only minor modifications of the spectrum.

The numerical implementation is vastly simplified by exploiting the fact that ν_e and $\bar{\nu}_e$ are in LTE in the region where the pair processes are effective. Instead of using the actual neutrino distributions in the phase-space integration we can use the equilibrium distribution with the local medium temperature. This approximation breaks down at larger radii where the $\nu_e\bar{\nu}_e$ process is unimportant anyway.

In order to further reduce computation time one of the remaining three phase-space integrations can be approximated by the analytic expressions given in Takahashi, El Eid, & Hillebrandt (1978). This also requires simplifying the blocking factors. With $\mu_e = -\mu_{e^+} \geq 0$ we can approximate the positron occupation number by a Maxwell-Boltzmann distribution. For $\mu_e/T \gtrsim 2$ this holds to very good accuracy. The greatest deviation is at $\mu_e/T = 0$ and yields blocking factors too low by about 10%. However, e^- and ν_e are always degenerate in the relevant regions.

3.6 Scattering on Electrons and Electron Neutrinos

Even though the scattering reactions on $e^\pm$ and on ν_e, $\bar{\nu}_e$ are closely related to the pair annihilations discussed in the previous section, scattering on $e^\pm$ is more important than on ν_e or $\bar{\nu}_e$. The matrix elements for these reactions are just the crossed versions of the leptonic pair processes,

$$\sum_{\text{spins}} |\mathcal{M}|^2 = 8\, G_F^2 \Big[(C_V + C_A)^2 s^2 + (C_V - C_A)^2 u^2 \Big] \tag{3.18}$$

with the weak interaction coefficients of Equations (3.12) or (3.13) for scattering on e^- or on ν_e, respectively. For $s = 2k_1 \cdot k_2$ and $u = -2k_1 \cdot k_4$ the momenta are assigned to the particles according to Figure 3.9. Crossing the

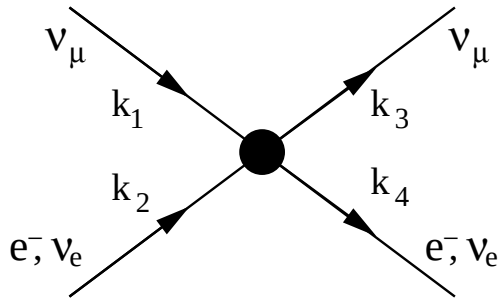

Fig. 3.9.— Leptonic scattering processes.

matrix element Equation (3.18) again by interchanging $u \leftrightarrow t$, we obtain scattering on e^+ or $\bar{\nu}_e$. This is also true for scattering of $\bar{\nu}_\mu$ on e^- or ν_e; scattering of $\bar{\nu}_\mu$ on e^+ or $\bar{\nu}_e$ brings us back to Equation (3.18). The numerical procedure for calculating the rates is the same as for the pair-annihilation processes, given in the previous section.

In contrast to the pair rates of the previous section, the differential scattering rates are monotonically rising functions of the degeneracy. In Figure 3.10 we show the rates for ν_μ scattering on $e^\pm$ (lower line) and the rates for ν_μ scattering on ν_e or $\bar{\nu}_e$, normalized to the latter rate. Scattering on ν_e and $\bar{\nu}_e$ is always more frequent than scattering on $e^\pm$ in case of $\eta_{\nu_e} = \eta_e$. However, for realistic situations with $\eta_{\nu_e} < \eta_e$ we expect that scattering on $e^\pm$ has 1–2 times the rate of scattering on ν_e and $\bar{\nu}_e$. Therefore, neutrino-neutrino scattering is expected to be a relatively minor correction. In our numerical

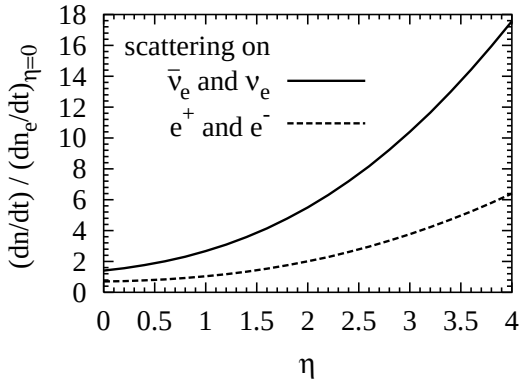

Fig. 3.10.— Thermally averaged scattering rate for ν_μ on $e^\pm$ as a function of η_e (lower line) and for ν_μ on ν_e and $\bar{\nu}_e$ (upper line) as a function of η_{ν_e}. The rates are normalized to the scattering rate on $e^\pm$ at $\eta_e = 0$. We used $T = 12$ MeV and $\eta_{\nu_\mu} = 0$.

studies we will indeed find that this process has only a small effect on the neutrino spectra and fluxes.

3.7 Other Reactions

Interactions that also take place inside a SN, but are unimportant for our purpose, are absorption and emission of ν_e and $\bar{\nu}_e$ by nuclei as well as scattering of neutrinos on nuclei. In the vicinity of the neutrino sphere all nuclei are disintegrated. Reactions on nuclei take place at larger radii and are therefore important for the heating process behind the stalled shock wave.

Throughout the past literature, oftentimes the plasmon process was taken into account as a source for neutrino pairs. The plasmon is an excitation of the medium that can emit a $\nu\bar{\nu}$ pair once it decays. In the relevant area close to the neutrino sphere this process is several orders of magnitude less frequent than the other pair processes.

Chapter 4

Setting the Stage for Neutrino Transport

Proto-neutron star atmospheres are characterized by their radial profiles of temperature, nucleon density, and the number of electrons per nucleon. In order to probe a variety of possible atmospheric structures we use two self-consistent profiles obtained by hydrodynamic simulations and, in addition, power-law parameterizations with constant electron fractions. After defining the optical depth and an effective mean free path for thermalizing processes we calculate the thermalization depths, i.e., the last points of interaction for all the thermalizing processes in each of the background models. This simple approach is a powerful test of the relative importance of various neutrino-matter interactions and their dependence on stellar parameters.

4.1 Characterizing Proto-Neutron Stars

All the neutrino interaction rates with the background medium depend on the density of scatterers and their temperature. Both density ρ and temperature T are functions of the radius. In the region relevant for neutrino spectra formation we assume that the proto-neutron star consist only of

- protons
- neutrons
- electrons
- positrons
- neutrinos of all flavors.

In order to calculate every interaction rate for all radii, we need the number density and the chemical potential for each of these matter constituents as a function of radius in addition to the temperature. As mentioned earlier no muons and taus are present. Therefore, usually we set the chemical potential of ν_μ to zero. Only in the case of weak magnetism a small ν_μ degeneracy develops and we obtain a chemical potential for ν_μ.

Our neutron-star atmospheres are characterized by $T(r)$, $\rho(r)$, and the electron fraction per baryon $Y_\mathrm{e}(r)$. Since $m_\mathrm{e} \ll m_\mathrm{n,p}$, the density is given by the number densities of neutrons and protons times their masses

$$\rho(r) = n_\mathrm{n}\, m_\mathrm{n} + n_\mathrm{p}\, m_\mathrm{p} \ . \tag{4.1}$$

In addition we use

$$Y_\mathrm{e}(r) = \frac{n_\mathrm{p}}{n_\mathrm{n} + n_\mathrm{p}} \tag{4.2}$$

to obtain the densities of neutrons and protons. By solving

$$n_\mathrm{n,p}(r) = \int \mathrm{d}\epsilon\, f_\mathrm{n,p}(\epsilon, \mu_\mathrm{n,p}) = \int \mathrm{d}\epsilon\, \frac{\epsilon^2}{1 + \exp(\frac{\epsilon - \mu_\mathrm{n,p}}{T})} \ , \tag{4.3}$$

we obtain the chemical potentials of protons and neutrons μ_n and μ_p.

Similarly, we determine μ_e by

$$n_\mathrm{B} Y_\mathrm{e} = n_{\mathrm{e}^-} - n_{\mathrm{e}^+} = \int \mathrm{d}\epsilon\, (f(\epsilon, \mu_\mathrm{e}) - f(\epsilon, -\mu_\mathrm{e})) \ . \tag{4.4}$$

A vanishing electron fraction does not mean that there are no electrons present, but rather that there is an equal thermal distribution of electrons and positrons.

After all other chemical potentials are known, μ_{ν_e} is given by Equation (3.16)

$$\mu_{\nu_\mathrm{e}} = \mu_\mathrm{e} + \mu_\mathrm{p} - \mu_\mathrm{n} \ .$$

This completes the set of thermodynamic quantities needed for the transport of neutrinos in a SN core.

4.2 Proto-Neutron-Star Profiles

One possibility for our study of the influence of neutrino interactions and the stellar background model on the emerging neutrino spectra is to use proto-neutron star atmospheres that were obtained by self-consistent hydrodynamic

simulations. As a first example we use a model representative for the accretion phase; henceforth we will refer to it as the "Accretion-Phase Model I" (Fig. 4.1). It was provided to us by O. E. B. Messer and was already used in Raffelt (2001) for a more schematic study. Based on the Woosley & Weaver $15\,M_\odot$ progenitor model labeled s15s7b, the Newtonian collapse simulation was performed with the SN code developed by Mezzacappa et al. (2001). The snapshot is taken at 324 ms after bounce when the shock is at about 120 km, i.e., the proto-neutron star still accretes matter. In this simulation the traditional microphysics for ν_μ transport was included, i.e., iso-energetic scattering on nucleons, e^+e^- annihilation and $\nu_\mu e^-$ scattering.

As another self-consistent example (Accretion-Phase Model II, Fig. 4.2) we obtained a 150 ms post bounce model from M. Rampp (personal communication) that uses a very similar progenitor (s15s7b2). The simulation includes an approximate general relativistic treatment in spherical symme-

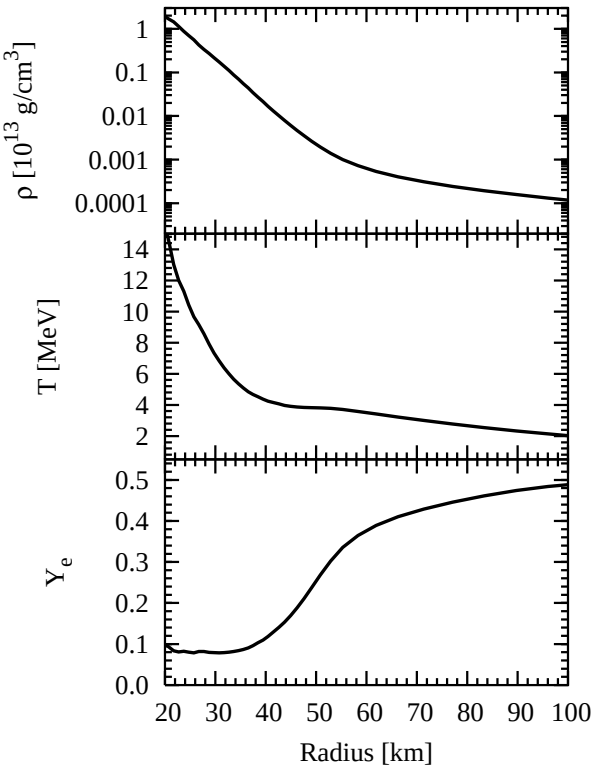

Fig. 4.1.— Accretion-Phase Model I, a SN model 324 ms after bounce from a Newtonian calculation (O.E.B. Messer, personal communication).

try as described by Rampp & Janka (2002). The three neutrino flavors are transported with all relevant interactions except $\nu_e\bar{\nu}_e \rightarrow \nu_\mu\bar{\nu}_\mu$ (Section 7.1 and Rampp et al. 2002).

When we use these self-consistent models with the same microphysics that was used in the original models by Messer and Rampp we find good agreement with their results. Changing the microphysical input then enables us to study the influence of the various interaction processes (Chapter 3) on the emerging neutrino spectra in a systematic way, which has never been done before. Since we are simulating a static proto-neutron star and also vary the input physics, our simulations are not self consistent. However, once our findings are implemented in the self-consistent hydrodynamic simulations they qualitatively find the same results as we do (Buras et al. 2003b).

The self-consistently obtained stellar background models are in the relevant range to a good approximation just power laws for the radial dependence of temperature and density. As a different approach we can thus parameterize

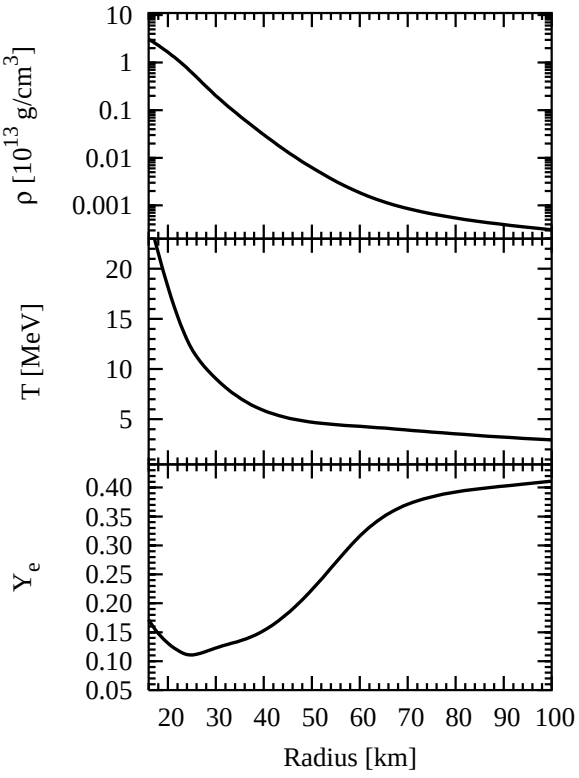

Fig. 4.2.— Accretion-Phase Model II, a SN core at 150 ms post bounce from a general-relativistic simulation. (M. Rampp, personal communication).

the profiles in a simple way and thereby study the influence of the stellar profiles. Especially steep profiles that are characteristic for the late phase of the proto-neutron star are not available to us from self-consistent simulations.

We use two power-law profiles of the form

$$\rho = \rho_0 \left(\frac{r_0}{r}\right)^p, \quad T = T_0 \left(\frac{r_0}{r}\right)^q, \tag{4.5}$$

with a constant electron fraction per baryon Y_e. We adjust parameters such that $\langle\epsilon\rangle \approx$ 20–25 MeV for the emerging neutrinos to obtain model atmospheres in the ball park of results from proto-neutron star evolution calculations. We define a "steep" power-law model, corresponding to the one used by Raffelt (2001), and a "shallow" one; the characteristics are given in Table 4.1. The shallow model could be characteristic of a SN core during the accretion phase while the steep model is more characteristic for the neutron-star cooling phase. The constant electron fraction Y_e is another parameter that allows us to investigate the relative importance of the leptonic processes as a function of the assumed Y_e.

Table 4.1. Characteristics of power-law models.

	Steep	Shallow
p	10	5
q	2.5	1
q/p	0.25	0.2
ρ_0 [10^{14} g cm^{-3}]	2.0	0.2
T_0 [MeV]	31.66	20.0
r_0 [km]	10	10

4.3 Optical Depth vs. Thermalization Depth

By comparing the optical depths due to different neutrino interactions we can assess the relative importance of the neutrino processes in the stellar background model. In principle the optical depth τ is defined as the integral of the inverse mfp λ^{-1} (see e.g. Shapiro & Teukolsky 1983, Suzuki 1989):

$$\tau_i(r,\epsilon) = \int_r^\infty dr' \frac{1}{\lambda_i(r',\epsilon)} = \int_r^\infty dr' \sigma_i(\epsilon)\, n_i(r')\,, \tag{4.6}$$

where i stands for any interaction channel, σ_i is the corresponding cross section, and n_i the number density. The optical depth specifies how frequently a specific process occurs on a neutrino's way out of the SN core.

Since we want to know how efficient a certain process is at exchanging energy we have to take into account the qualitatively different nature of the neutrino-matter interactions. The relevant interaction processes fall into three classes:

1. **Creation processes**, that are able to keep neutrinos in LTE. They can create and absorb neutrinos and therefore also contribute to the energy exchange between neutrinos and the background medium.

2. **Scattering with large energy transfer**. In this case the neutrinos scatter on particles with a low mass compared to the neutrino's momentum (i.e., $e^{\pm}$ and neutrinos).

3. **Scattering on nucleons**. Here the energy transfer is very small in a single scattering, The fact that allows for the effective mfp description discussed in the previous section.

All three classes contribute to the opacity, but only the first two classes of reactions can exchange large amounts of energy in single interactions.

Making use of this qualitative difference between nucleon scattering and the other interactions we can define the location (thermalization depth) where a neutrino of given energy last exchanged energy efficiently with the medium by a reaction such as $\nu_\mu e^- \rightarrow e^- \nu_\mu$. Looking at the example of $\nu_\mu e^-$ scattering we have two different mfps, namely one for nucleon scattering λ_T and one for the energy exchanging $\nu_\mu e^-$ process λ_E. The total mfp is then given by $\lambda_{\mathrm{tot}} = 1/(\lambda_T^{-1} + \lambda_E^{-1})$. Between two energy exchanging scatterings the neutrino undergoes many isoenergetic scatterings. This yields an effective mfp for the energy exchange reaction that is larger than λ_E.

The way of a neutrino through the medium can be considered a random walk. Therefore the traveled distance scales as the square root of time that is proportional to $\sqrt{N}$, where N represents the number of interactions. For each reaction the probability of energy exchange is $\lambda_{\mathrm{tot}}/\lambda_E$, so the inverse is the number of reactions until the next energy exchange. Altogether the traveled distance from one energy-exchange reaction to the other corresponds to the effective mfp of the energy exchanging process:

$$\lambda_E^{\mathrm{eff}} = \lambda_{\mathrm{tot}} \sqrt{\frac{\lambda_E}{\lambda_{\mathrm{tot}}}} = \sqrt{\frac{\lambda_E}{\lambda_T^{-1} + \lambda_E^{-1}}} \tag{4.7}$$

With the effective mfp we can then calculate the optical depth for thermalization

$$\tau_{\rm therm}(r,\epsilon) = \int_r^\infty dr' \sqrt{\frac{1}{\lambda_E(r',\epsilon)}\left[\frac{1}{\lambda_T(r',\epsilon)} + \frac{1}{\lambda_E(r',\epsilon)}\right]}\,. \tag{4.8}$$

When the optical depth becomes less than of order unity, the corresponding process is no longer relevant. The corresponding radius is referred to as the thermalization depth:

$$\tau_{\rm therm}(R_{\rm therm}) = \frac{2}{3}\,, \tag{4.9}$$

where $R_{\rm therm}$ depends on the neutrino energy ϵ.

With this concept we can determine the energy-dependent sphere where a certain class of reactions becomes inefficient. For a specific neutrino energy the corresponding radius is given by the largest $R_{\rm therm}$ of any reaction in the class. For the first class this sphere corresponds to the number sphere, where particle creation freezes out, as defined in Section 2.5. The second class of reactions freezes out at the radius that determines the energy sphere.

For the third class, i.e., neutrino-nucleon scattering, we are not able to obtain the thermalization depth. In each reaction the energy transfer is very small, thus many reactions are necessary to thermalize the neutrino. We can therefore not determine the location of the transport sphere, i.e., the radius at that neutrino-nucleon scattering becomes inefficient.

As we show in the next section, due to the energy dependence it is not possible to define a unique neutrino sphere. Even for $\nu_{\rm e}$ and $\bar{\nu}_{\rm e}$, where the β-processes dominate and therefore the only relevant sphere is their number sphere, its location is strongly energy dependent. The other flavors are emitted at their number sphere, lose energy in elastic scattering up to their transport sphere, and then diffuse before they start streaming freely from their transport sphere. Compared to $\nu_{\rm e}$ and $\bar{\nu}_{\rm e}$ one would refer to the number sphere as neutrino sphere of ν_μ. The spectrum emitted at this neutrino sphere, however, is very different from the emitted spectrum.

In order to illustrate the ν_μ transport let us consider bremsstrahlung and iso-energetic scattering on nucleons only. For nucleon bremsstrahlung the energy dependence is rather weak and at the same time the density dependence is very strong. Therefore, to a good approximation one may picture the bremsstrahlung-number sphere as a blackbody surface that injects neutrinos into the scattering atmosphere and absorbs those scattered back (Raffelt 2001). With iso-energetic scattering on nucleons, the neutrino flux and spectrum emerging from the transport sphere is then easily understood in terms of the energy-dependent transmission probability of the blackbody spectrum

launched at the number sphere, that is in this simple picture equal to the energy sphere. The transport cross section scales as ϵ^2, implying that the transmitted flux spectrum is shifted to lower energies relative to the temperature at the energy sphere. This simple "filter effect" accounts surprisingly well for the emerging flux spectrum (Raffelt 2001). For typical conditions the mean flux energies are 50–60% of those corresponding to the blackbody conditions at the energy sphere.

Moreover, it is straightforward to understand that the effective temperature of the emerging flux spectrum is not overly sensitive to the exact location of the number sphere. If the pair processes are somewhat more effective, the number sphere is at a larger radius with a lower medium temperature. However, the scattering atmosphere has a smaller optical depth so that the higher-energy neutrinos are less suppressed by the filter effect, partly compensating the smaller energy-sphere temperature. For typical situations Raffelt (2001) found that changing the bremsstrahlung rate by a factor of 3 would change the emerging neutrino energies only by some 10%. This finding suggests that the emitted average neutrino energy is not overly sensitive to the details of the pair processes.

With the complete set of interactions neutrinos undergo energy exchanging scattering reactions below the energy sphere before they enter the diffusive regime. Therefore the mean energy of the emerging flux is even less sensitive to the exact location of the number sphere than found by Raffelt (2001). In Section 6.3 we show that changing the bremsstrahlung rate by a factor of three up or down has almost no effect on the mean energy of the emerging neutrino flux.

4.4 Thermalization Depths in Our Stellar Models

We now turn to applying the concept of thermalization depths to the neutron-star atmospheres described above (Section 4.2). We consider the neutrino mfp for nucleon bremsstrahlung $\mathrm{NN} \to \mathrm{NN}\nu_\mu\bar{\nu}_\mu$, pair annihilation $\mathrm{e}^+\mathrm{e}^- \to \nu_\mu\bar{\nu}_\mu$ and $\nu_\mathrm{e}\bar{\nu}_\mathrm{e} \to \nu_\mu\bar{\nu}_\mu$, and scattering on charged leptons $\nu_\mu\mathrm{e}^\pm \to \mathrm{e}^\pm\nu_\mu$. The reaction rates used were described in Chapter 3.

In Figures 4.3 and 4.4 we give the thermalization depth R_therm as a function of neutrino energy ϵ for the two hydrodynamically self-consistent accretion-phase models. From top to bottom the panels show the results for ν_e, $\bar{\nu}_\mathrm{e}$, and ν_μ, respectively. The step-like curves represent the temperature profiles in terms of the mean neutrino energy, $\langle\epsilon_\nu\rangle = 3.15\,T$ for non-

degenerate neutrinos at the local medium temperature; the steps correspond to the radial zones of our numerical simulation. Slightly above these steps the thin line represents the mean energy of neutrinos flowing in radial direction obtained by our numerical simulation. The other curves represent $R_{\rm therm}$ for bremsstrahlung (b), e^+e^- annihilation (p), $\nu_e\bar{\nu}_e$ annihilation (n), and scattering on $e^\pm$ (s). In the case of ν_e and $\bar{\nu}_e$ we do not include bremsstrahlung and $\nu_e\bar{\nu}_e$ annihilation. Particle creation is dominated by the charged current reactions on nucleons (urca).

For the power-law models we show $R_{\rm therm}$ for ν_μ in Figures 4.5 and 4.6. The different panels correspond to the indicated values of the electron fraction Y_e. Note that Y_e represents the net electron density per baryon, i.e., the e^- density minus that of e^+ so that $Y_e = 0$ implies that there is an equal thermal population of e^- and e^+.

The ν_μ absorption rate for the bremsstrahlung process varies approximately as ϵ^{-1}, the ν_μN transport cross section as ϵ^2 so that the inverse mfp for thermalization varies only as $\epsilon^{1/2}$. This explains why $R_{\rm therm}$ for bremsstrahlung is indeed quite independent of ϵ. Therefore, bremsstrahlung alone allows one to specify a rather well-defined number sphere. The other processes depend much more sensitively on ϵ so that a mean energy sphere is much less well defined.

Both electron scattering and the leptonic pair processes are so ineffective at low energies that true LTE can not be established even for astonishingly deep locations. Bremsstrahlung easily "plugs" this low-energy hole so that one can indeed expect LTE for all relevant neutrino energies below a certain radius. For higher energies, the leptonic processes dominate and shift the energy sphere to larger radii than bremsstrahlung alone. The relative importance of the various processes depends on the density and temperature profiles as well as Y_e.

To assess the role of the various processes for the overall spectra formation one needs to specify some typical neutrino energy. One possibility would be $\langle\epsilon\rangle$ for neutrinos in LTE. Another possibility is the mean energy of the neutrino flux, in particular the mean energy of those neutrinos which actually leave the star. In Figures 4.3–4.6 the thin line represents this flux mean energy. In the case of ν_μ it is clearly visible that even after the last energy exchanging process, i.e., $e^\pm$ scattering, became ineffective the mean energy of the flux still drops. This drop is due to scattering on nucleons. Among the pair processes it is always the $\nu_e\bar{\nu}_e$ annihilation process that has the largest $R_{\rm therm}$ in the range of flux energy. However, especially in the steep power-law profile the intersection of the bremsstrahlung's and $\nu_e\bar{\nu}_e$ annihilation's thermalization depths are rather close at the mean flux energy. The e^+e^- process is always less important than $\nu_e\bar{\nu}_e$, as was already discussed in Section 3.5.

In our numerical simulations we find the same results (Chapter 6).

The final shape of the ν_μ spectra and therefore also their mean energy cannot depend much on any of the ν_μ-creation processes. The energy sphere represented by $R_{\rm therm}$ of $e^\pm$ scattering stretches in all profiles far beyond the other thermalization depths. Additionally, also the scattering on nucleons has a significant impact on the mean energies. Its importance compared to electron scattering is very difficult to guess. Recall, it is not possible to define a thermalization depth for nucleon recoils. Both processes are qualitatively very different in that neutrinos transfer only a small fraction of their energy per nucleon scattering. Numerically we have compared the importance of all processes and present our results in Chapter 6.

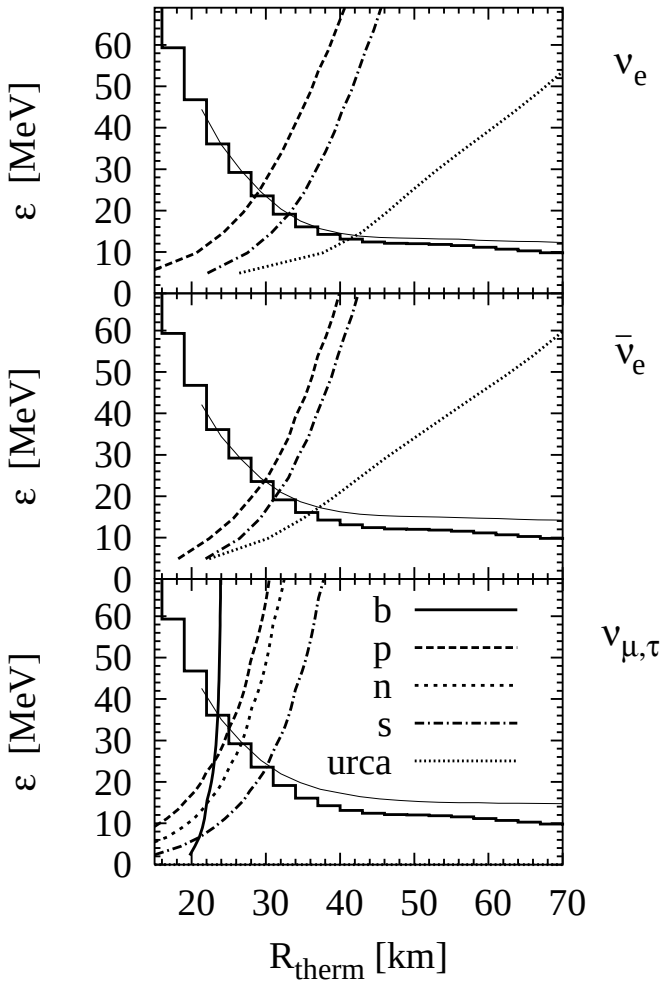

Fig. 4.3.— $R_{\rm therm}$ as a function of neutrino energy ϵ for our Accretion-Phase Model I. From top to bottom the panels show the results for $\nu_{\rm e}$, $\bar{\nu}_{\rm e}$, and ν_μ. Energy exchanging processes: bremsstrahlung (solid line), e^+e^- annihilation (dashed), $\nu_{\rm e}\bar{\nu}_{\rm e}$ annihilation (dotted), and scattering on $e^\pm$ (dash-dotted). "Urca" denotes the charged-current reaction of $\nu_{\rm e}$ and $\bar{\nu}_{\rm e}$ on nucleons. The steps represent $\langle\epsilon\rangle = 3.15\,T$; the thin line close to $3.15\,T$ is the mean energy of the flux $\langle\epsilon\rangle_{\rm flux}$, cf. Chapter 5.

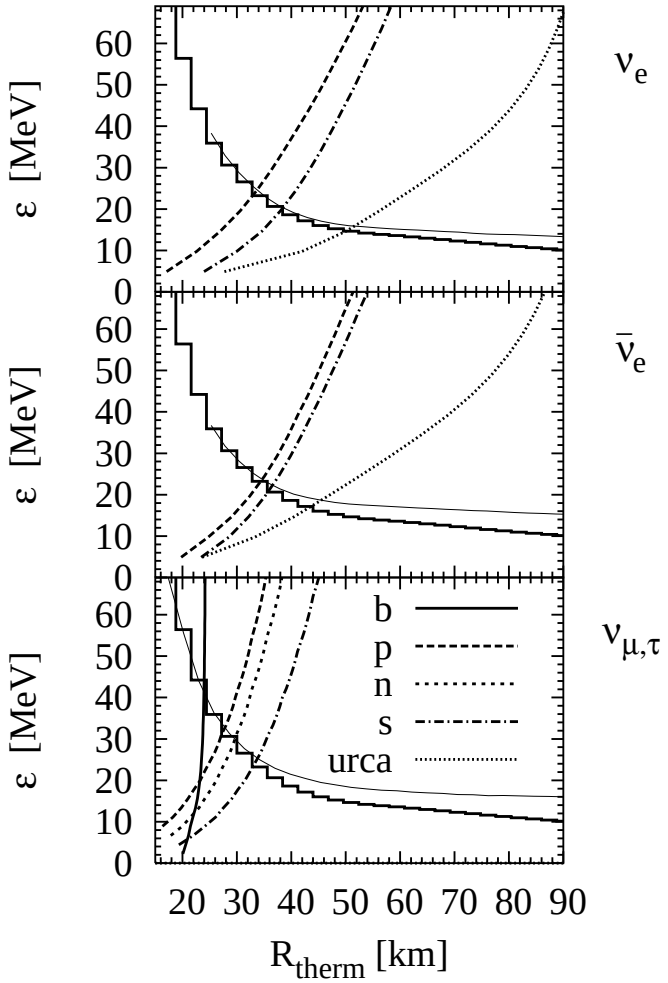

Fig. 4.4.— Same as Figure 4.3 for the Accretion-Phase Model II.

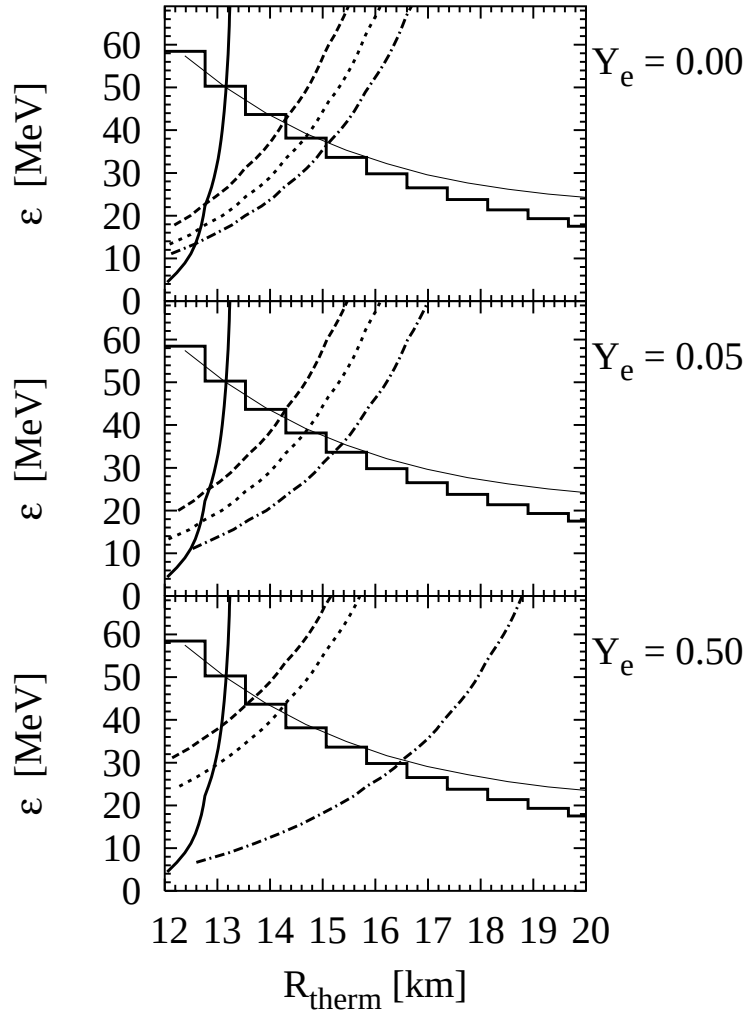

Fig. 4.5.— $R_{\rm therm}$ for ν_μ in the steep power-law model with the indicated values of $Y_{\rm e}$. This figure corresponds to the bottom panel of Figure 4.3.

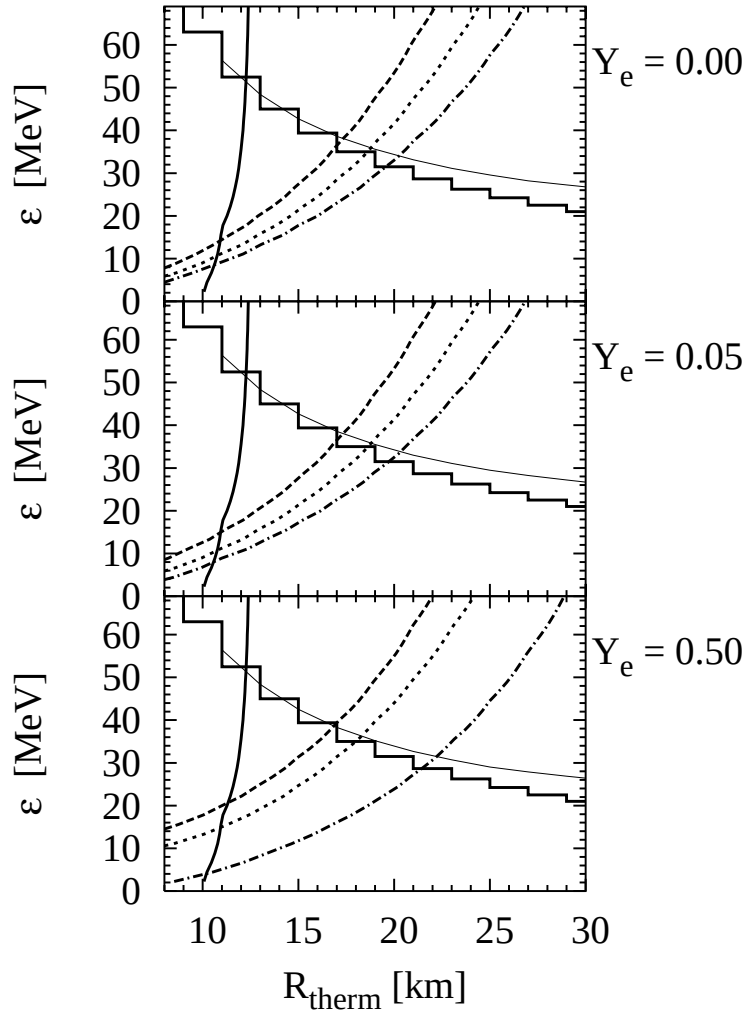

Fig. 4.6.— Same as Fig. 4.5 for the shallow power-law model.

Chapter 5

Characterizing Non-Thermal Neutrino Spectra

The neutrino fluxes emerging from a SN core are not thermal. There are numerous ways to describe spectral characteristics with a few parameters, for example energy moments. For many applications it is useful to have an analytic description of the spectra. Throughout the literature it is common to use an nominal Fermi-Dirac distribution. We present a simpler two-parameter fit that describes our Monte Carlo data better, and compare both descriptions.

5.1 Global Parameters

While a SN core can be crudely understood as a blackbody source for neutrinos of all flavors, the escaping fluxes are not strictly thermal. A number of observables have been defined in the literature in order to describe the properties of these spectra.

Let us assume $f(\epsilon, \mu)$ is the distribution of neutrinos as a function of energy ϵ and $\mu = \cos\theta$, where θ is the angle between the radial direction and the direction of motion. Far away from the SN core neutrinos stream freely in radial direction, therefore $\mu = 1$.

As the most intuitive quantity characterizing the spectrum the mean energy is commonly used,

$$\langle\epsilon\rangle = \frac{\int_0^\infty d\epsilon\, \epsilon \int_{-1}^{+1} d\mu\, f(\epsilon,\mu)}{\int_0^\infty d\epsilon \int_{-1}^{+1} d\mu\, f(\epsilon,\mu)}\,. \tag{5.1}$$

In this ratio the numerator is the energy density and the denominator is the number density.

Within the number sphere neutrinos are in LTE, but in the outer regions some net flux of neutrinos develops. Therefore, it is often useful to extract spectral characteristics for those neutrinos which are actually flowing by removing the isotropic part of the distribution. Specifically, we define the mean flux energy by

$$\langle\epsilon\rangle_{\rm flux} = \frac{\int_0^\infty d\epsilon\,\epsilon\,\int_{-1}^{+1} d\mu\,\mu\,f(\epsilon,\mu)}{\int_0^\infty d\epsilon\,\int_{-1}^{+1} d\mu\,\mu\,f(\epsilon,\mu)}\,. \tag{5.2}$$

Outside the transport sphere all neutrinos will flow essentially in the radial direction, implying that the angular distribution becomes a delta-function in the forward direction so that $\langle\epsilon\rangle_{\rm flux} = \langle\epsilon\rangle$. In the trapping regions the two averages are very different because the distribution function is dominated by its isotropic term. However, for most discussions only the emerging spectra are relevant and both definitions of the mean energy, Equations (5.1) and (5.2) are equivalent. The right hand side of Equation (5.2) then corresponds to the ratio of luminosity to number flux.

Deep inside the core, below the number sphere neutrinos are in LTE. With a vanishing chemical potential their distribution function is given by

$$f(\epsilon,\mu) = \frac{\epsilon^2}{1+\exp(\epsilon/T)} \tag{5.3}$$

and therefore

$$\langle\epsilon\rangle = \frac{7\pi^4}{180\,\zeta_3}\,T \approx 3.1514\,T\,. \tag{5.4}$$

We use this relation to compare the numerically obtained mean energy to the medium temperature, cf. e.g. Figure 4.3.

Since the emerging spectra are not thermal, additional characteristics are useful. A rather general way to characterize the spectrum beyond mean values is by its energy moments (Janka & Hillebrandt 1989a)

$$\langle\epsilon^n\rangle = \frac{\int_0^\infty d\epsilon\,\epsilon^n\,\int_{-1}^{+1} d\mu\,f(\epsilon,\mu)}{\int_0^\infty d\epsilon\,\int_{-1}^{+1} d\mu\,f(\epsilon,\mu)}\,. \tag{5.5}$$

Usually, values are given only up to n=2 in the literature, i.e., the mean energy and the second moment.

With the first two moments an easy way to see by how much a spectrum deviates from being thermal is the pinching parameter, defined by Raffelt (2001). It is basically the ratio of the first two moments

$$p \equiv \frac{1}{a}\,\frac{\langle\epsilon^2\rangle}{\langle\epsilon\rangle^2}\,, \tag{5.6}$$

normalized such that a Fermi-Dirac distribution with vanishing chemical potential yields $p = 1$. Therefore,

$$a \equiv \frac{\langle\epsilon^2\rangle_{\rm FD}}{\langle\epsilon\rangle^2_{\rm FD}} = \frac{486000\,\zeta_3\zeta_5}{49\,\pi^8} \approx 1.3029\,. \tag{5.7}$$

For a Maxwell-Boltzmann distribution this quantity would be 4/3. A spectrum that is thermal up to its second moment has $p = 1$, while $p < 1$ signifies a pinched spectrum (high-energy tail suppressed), $p > 1$ an anti-pinched spectrum (high-energy tail enhanced).

In some publications the root-mean-square energy $\langle\epsilon\rangle_{\rm rms}$ is given instead of the average energy. The rms-energy involves the ratio of third and first energy moment

$$\langle\epsilon\rangle_{\rm rms} = \sqrt{\frac{\int_0^\infty d\epsilon \int_{-1}^{+1} d\mu\, \epsilon^3 f(\epsilon,\mu)}{\int_0^\infty d\epsilon \int_{-1}^{+1} d\mu\, \epsilon\, f(\epsilon,\mu)}} = \sqrt{\frac{\langle\epsilon^3\rangle}{\langle\epsilon\rangle}}\,. \tag{5.8}$$

This characteristic spectral energy is useful for estimating the energy transfer from neutrinos to the stellar medium in reactions with cross sections proportional to ϵ^2. However, comparing the mean energy defined in Equation (5.1) and the rms-energy is difficult, because the relation of both quantities depends on the spectral shape.

5.2 Analytic Fits

For applications like neutrino oscillations it is useful to have an analytic fit to the SN neutrino spectra. We present a two-parameter fit that reproduces the first five or more moments of our numerically obtained spectra to a very good accuracy (Section 7.3). In addition to the overall normalization we introduce the parameters α and $\bar\epsilon$ by defining

$$f_\alpha(\epsilon) = \frac{1}{c}\left(\frac{\epsilon}{\bar\epsilon}\right)^\alpha \mathrm{e}^{-(\alpha+1)\,\epsilon/\bar\epsilon}\,, \tag{5.9}$$

with the normalization

$$c = \int_0^\infty \mathrm{d}\epsilon\; f_\alpha(\epsilon) = (\alpha+1)^{-(\alpha+1)}\;\Gamma(\alpha+1)\;\bar\epsilon\,. \tag{5.10}$$

The average energy is always $\langle\epsilon\rangle = \bar\epsilon$, while α controls the pinching of the function. Just like the mean energy all observables discussed in the previous section can be expressed in terms of α and $\bar\epsilon$ by simple analytic relations.

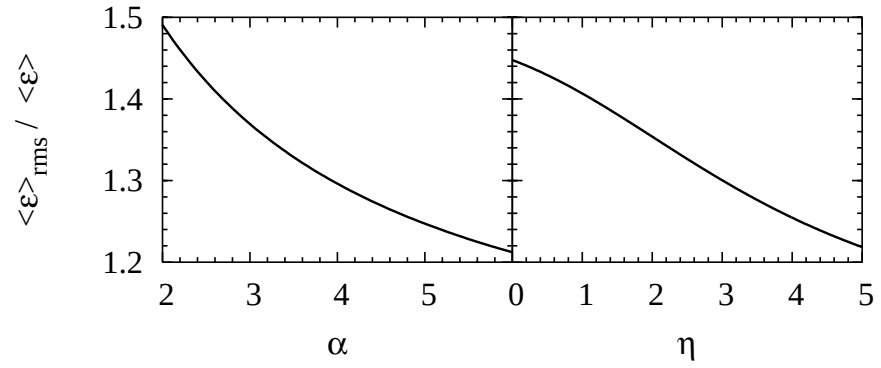

Fig. 5.1.— The ratio of rms energy and mean energy. The left panel shows the dependence on α as given in Equation (5.14); in the right panel we plot the dependence on η.

The pinching parameter p is closely related to the width

$$w = \sqrt{\langle\epsilon^2\rangle - \langle\epsilon\rangle^2} = \sqrt{a\,p - 1}\,\langle\epsilon\rangle = \sqrt{\frac{1}{1+\alpha}}\,\bar{\epsilon}\,, \tag{5.11}$$

with $a \approx 1.3029$ as defined in Equation (5.7). The relation for the pinching parameter can be read off Equation (5.11),

$$a\,p = \frac{\langle\epsilon^2\rangle}{\langle\epsilon\rangle^2} = \frac{2+\alpha}{1+\alpha}\,. \tag{5.12}$$

For the more general case of the ratios of arbitrary neighboring moments we find

$$\frac{\langle\epsilon^n\rangle}{\langle\epsilon^{n-1}\rangle} = \frac{n+\alpha}{1+\alpha}\,\bar{\epsilon}\,, \tag{5.13}$$

that can be easily generalized to arbitrary ratios of moments with Equation (5.10).

Taking the ratio of third and first energy moment yields the rms-energy

$$\langle\epsilon\rangle_{\rm rms} = \sqrt{\frac{(2+\alpha)(3+\alpha)}{(1+\alpha)^2}}\,\bar{\epsilon}\,. \tag{5.14}$$

As shown in in the left panel of Figure 5.1, $\langle\epsilon\rangle_{\rm rms}$ is always some 25–45% larger than $\langle\epsilon\rangle$ in the range of $\alpha = 2$–5, that turns out to be the parameter range obtained by numerical simulations. Therefore, the two different energy averages contain information on the spectral shape.

From any three moments it is possible to obtain the normalization, α, and $\bar{\epsilon}$. From all our studies we found that the spectra are very well described by these three parameters.

In the literature one frequently encounters a nominal Fermi-Dirac distribution characterized by a temperature T and a degeneracy parameter η according to

$$f_\eta(\epsilon) = \frac{\epsilon^2}{1 + \exp\left(\frac{\epsilon}{T} - \eta\right)} \tag{5.15}$$

as a representation of the SN neutrino spectrum (Janka & Hillebrandt 1989a). The functional form is motivated by the equilibrium distribution of neutrinos inside the star. The values of the parameters T and η, however, are not easy to interpret, because the emerging spectra are not thermal.

The functional form of f_η is more complicated than f_α. Most calculations involving f_η have to be carried out numerically and/or approximately. In Figure 5.2 we show $\langle \epsilon/T \rangle$ and p as a function of η. Up to second order,

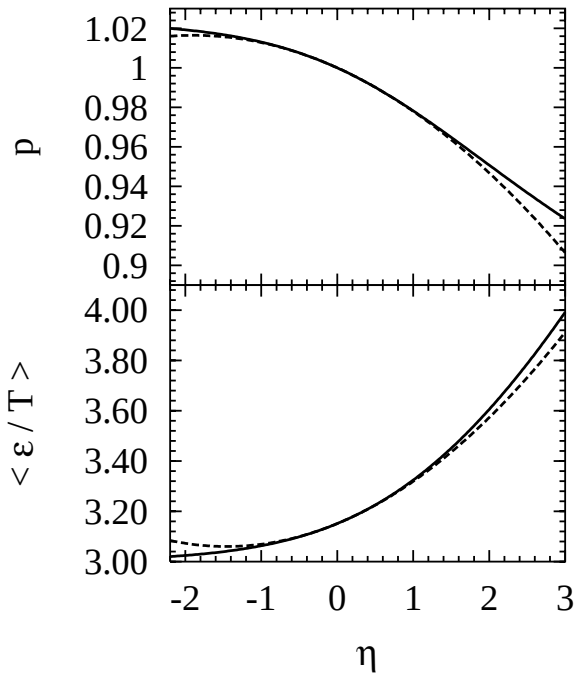

Fig. 5.2.— Mean energy and pinching parameter as a function of the degeneracy parameter for a Fermi-Dirac distribution. As dashed lines we show the expansions given in Equation (5.16).

expansions are

$$\begin{aligned} \langle\epsilon/T\rangle &\approx 3.1514 + 0.1250\,\eta + 0.0429\,\eta^2 \\ p &\approx 1 - 0.0174\,\eta - 0.0046\,\eta^2\,. \end{aligned} \tag{5.16}$$

These expansions are shown in Figure 5.2 as dashed lines.

There are no analytic expressions for the energy moments and therefore also the rms-energy can only be obtained numerically. For the special case of $\eta = 0$ the expression is

$$\langle\epsilon\rangle_{\rm rms} = \sqrt{\frac{930}{441}}\,\pi\,T \approx 4.5622\,T\,. \tag{5.17}$$

With Equation (5.4) this corresponds to $\langle\epsilon\rangle \approx 0.691\langle\epsilon\rangle_{\rm rms}$, but recall that SN neutrino spectra are not thermal spectra and $\eta \neq 0$. The numerically obtained dependence of the ratio of rms and mean energy is displayed in the right panel of Figure 5.1. It is rather similar to the case of the α fit.

In view of analytic simplicity the α fit is certainly superior, but the shapes of both functions are rather similar. The numerically determined spectra are similarly well described by both f_η and f_α. As we show in the following for a reasonable range for the parameters both functions differ by no more than about 10%.

In the upper panel of Figure 5.3 we show $f_\alpha(\epsilon)$, the integral normalized to unity, for several values of α. The broadest curve is for $\alpha = 2$ while for the narrower ones the width given in Equation (5.11) was decreased in 10% decrements as shown in Table 5.1. The middle panel of Figure 5.3 shows the corresponding curves $f_\eta(\epsilon)$ with the η-values given in Table 5.1. The broadest curves in each panel are identical and correspond to $\epsilon^2\exp(-3\epsilon/\bar{\epsilon})$ with a width $w_0 = \langle\epsilon\rangle/\sqrt{3}$.

Table 5.1. Parameters for fit-functions of Figure 5.3.

Width	α	η
$w_0 = \langle\epsilon\rangle/\sqrt{3}$	2.	$-\infty$
$0.9\,w_0$	2.7037	1.1340
$0.8\,w_0$	3.6875	2.7054
$0.7\,w_0$	5.1225	4.4014
$0.6\,w_0$	7.3333	6.9691
$0.5\,w_0$	11.	13.892

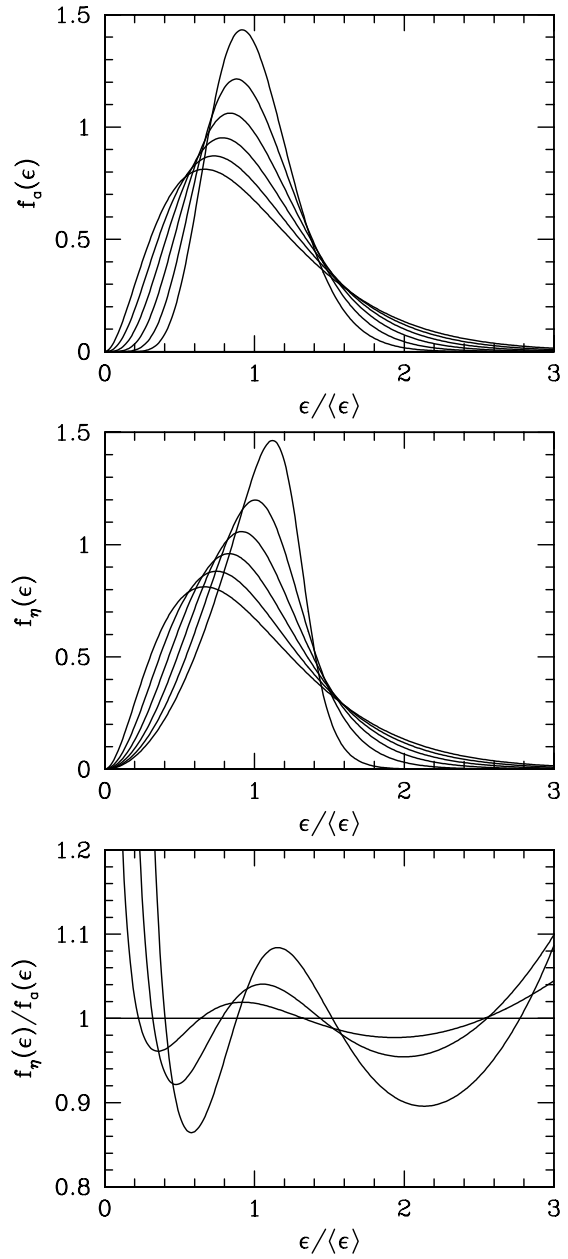

Fig. 5.3.— Normalized fit functions. *Upper panel:* α-fit according to Equation (5.9). *Middle panel:* Fermi-Dirac fit according to Equation (5.15). In both panels the broadest curve corresponds to $f(\epsilon) = \epsilon^2 \exp(-3\epsilon/\bar{\epsilon})$, i.e., to $\alpha = 2$ and $\eta = -\infty$, respectively. For the other curves the width was decreased in decrements of 10%, see Table 5.1. *Bottom panel:* Ratio of the fits f_α/f_η for the first four cases.

The limiting behavior of $f_\alpha(\epsilon)$ for large α is $\delta(\epsilon - \bar{\epsilon})$ while for $f_\eta(\epsilon)$ the limiting width is $w_0/\sqrt{5} \approx 0.44721\, w_0$. Evidently the curves $f_\alpha(\epsilon)$ can accommodate a much broader range of widths than the curves $f_\eta(\epsilon)$.

We find that the neutrino spectra are always fit with parameters in the range $2 \lesssim \alpha \lesssim 5$ or $0 \lesssim \eta \lesssim 4$ (Section 7.1), i.e. with a width above about $0.75\, w_0$. In the bottom panel of Figure 5.3 we show the ratios of the fit functions for the widths down to $0.7\, w_0$. From this plot we find that except for the lowest energies and very high energies the two fit functions are equivalent to better than 10%. Therefore, the two types of fits are largely equivalent for most practical purposes.

On the basis of a few high-statistics Monte Carlo runs we show in Section 7.3 that the numerical spectra are actually better approximated over a broader range of energies by the "power-law" fit functions $f_\alpha(\epsilon)$. In addition, these functions are more flexible at representing the high-energy tail of the spectrum that is most relevant for studying the Earth effect in neutrino oscillations.

Chapter 6

Relative Importance of Neutral-Current Reactions

We briefly introduce our Monte Carlo code, that was developed to study neutrino transport in proto-neutron-star atmospheres. For the proto-neutron-star atmospheres presented in Section 4.2 we show our results that were obtained by switching on and off various neutral-current interaction processes.

The traditional set of processes included in ν_μ transport turns out to be a rather poor approximation. Contrary to what had been assumed in the past, nucleon-nucleon bremsstrahlung and the $\nu_e\bar{\nu}_e$ pair process are the main sources for $\nu_\mu\bar{\nu}_\mu$ production. Above the number sphere the spectra are shaped by electron scattering and scattering on recoiling nucleons. The traditional $e^+e^- \rightarrow \nu_e\bar{\nu}_e$ process and scattering on $\nu_e/\bar{\nu}_e$ turn out to be rather negligible.

These results and those of Chapter 7 represent a major part of this dissertation and were already published in a similar form as:
M. T. Keil, G. G. Raffelt, and H. T. Janka, "Monte Carlo study of supernova neutrino spectra formation," Astrophys. J. in press, astro-ph/0208035.

6.1 Monte Carlo Setup

For the stellar background models introduced in Section 4.2 we have run our Monte Carlo code using various sets of neutrino-matter interactions. In Appendix B we give a detailed description of the code. Our main interest is to assess the impact of the various neutrino interactions on the flux and spectrum formation. Since neutrinos are in LTE below the number sphere, it is sufficient to simulate the neutrino transport starting slightly below that radius where we have to specify a boundary condition.

At that lower boundary of our proto-neutron-star atmosphere we always

impose a blackbody boundary condition. We assume neutrinos to be in LTE, i.e., at the local temperature and the appropriate chemical potential. For numerical runs discussed in this chapter the latter is taken to vanish, because only ν_μ are involved and weak magnetism is discussed in the next chapter. As a consequence of this inner boundary condition, the luminosity emerging at the surface is generated within the computational domain and calculated by our Monte Carlo transport. A small flux across the inner boundary develops because of the negative gradients of temperature and density in the atmosphere. Its magnitude depends on the radial resolution of the proto-neutron-star atmosphere and is therefore an artifact of the numerical implementation. However, for our setups this flux is small compared to the luminosity at the surface and therefore the emerging neutrino spectra do not depend on the lower boundary condition.

The shallow energy dependence of the thermalization depth of the nucleon bremsstrahlung implies that whenever we include this process it is not difficult to choose a reasonable location for the lower boundary. Taking the latter too deep in the star is very CPU-expensive as one spends most of the simulation for calculating frequent scatterings of neutrinos that are essentially in LTE.

The outer boundary is determined by the requirement that neutrinos stream freely. In the outer regions the transport is not CPU-expensive. Therefore, the exact location of the outer boundary is not very crucial. However, we always use a grid of 30 equally spaced radial zones and can thus obtain better spatial resolution by choosing the outer boundary fairly low.

We always include ν_μN scattering as the main opacity source. For energy exchange, we switch on or off the processes given in Table 6.1. We never include inelastic nucleon scattering $\nu_\mu\mathrm{NN} \rightarrow \mathrm{NN}\nu_\mu$ as this process is never

Table 6.1. Neutral-current processes included in our ν_μ tranport.

Process	Label
bremsstrahlung	b
nucleon recoil	r
scattering on e^+ and e^-	s
e^+e^- pair annihilation	p
$\nu_e\bar{\nu}_e$ annihilation	n
scattering on ν_e and $\bar{\nu}_e$	sn

important relative to recoil (Raffelt 2001). For confirming that scattering on ν_e and $\bar{\nu}_e$ is really unimportant if $\nu_\mu e^\pm$ is included (Section 3.6) we used the Accretion-Phase Model I. In all other models we ignore this process. We also neglect $\nu_\mu\nu_\mu$ or $\nu_\mu\bar{\nu}_\mu$ scattering even though such processes may have a larger rate than some of the included leptonic processes. Processes of this type do not exchange energy between the neutrinos and the background medium. They are therefore not expected to affect the emerging fluxes and should also have a minor effect on the emitted spectra. We study weak magnetism in Chapter 7.

6.2 Accretion-Phase Model I

Our first goal is to assess the relative importance of different energy-exchange processes for the ν_μ transport. As a first example we begin with our Accretion-Phase Model I. The results from our numerical runs are summarized in Table 6.2, where for each run we give $\langle\epsilon\rangle_{\rm flux}$, $\langle\epsilon^2\rangle_{\rm flux}$, our fit parameter α determined by Equation (5.12), and the pinching parameter $p_{\rm flux}$ for the emerging flux spectrum, defined in Equation (5.6). We fitted the temperature and degeneracy parameter of an effective Fermi-Dirac spectrum producing the same first two energy moments, and give the luminosity. Only $\langle\epsilon\rangle_{\rm flux}$, $\langle\epsilon^2\rangle_{\rm flux}$, and the luminosity were obtained from the numerical simulations. All other characteristics were calculated from these first two energy moments.

The first row contains the muon neutrino flux characteristics of the original Boltzmann transport calculation by Messer. To make a connection to these results we ran our code with the same input physics, i.e., $\nu_\mu e^\pm$ scattering (s) and e^+e^- annihilation (p). There remain small differences between the original spectral characteristics and ours. These can be caused by differences in the implementation of the neutrino processes, by the limited number of energy and angular bins in the Boltzmann solver, the coarser resolution of the radial grid in our Monte Carlo runs, and by our simple blackbody lower boundary condition. We interpret the first two rows of Table 6.2 as agreeing sufficiently well with each other that a detailed understanding of the differences is not warranted. Henceforth we will only discuss differential effects within our own implementation.

In the next row (bsp) we include nucleon bremsstrahlung which has the effect of increasing the luminosity by a sizable amount without affecting much the spectral shape. This suggests that bremsstrahlung is important as a source for $\nu_\mu\bar{\nu}_\mu$ pairs, but that the spectrum is then shaped by the energy-exchange in scattering with $e^\pm$. In the next row (bp) we switch off $e^\pm$ scattering so that no energy is exchanged except by pair-producing processes. The

spectral energy indeed increases significantly. However, the biggest energy-exchange effect in the scattering regime is nucleon recoil. In the next two rows we include recoil (brp) and then additionally $e^{\pm}$ scattering (brsp), both lowering the spectral energies and also the luminosities.

The picture of all relevant processes is completed by adding $\nu_e\bar{\nu}_e$ pair annihilation (brspn), which is similar to e^+e^- pair annihilation, but a factor of 2–3 more important (Section 3.5). The luminosity is again increased, an effect which is understood in terms of our blackbody picture for the number and energy spheres. In the lower panel of Figure 4.3 we see that $R_{\rm therm}$ moves to larger radii once "n" is switched on, the radiating surface of the "blackbody" increases and more pairs are emitted. For both "p" and "n" $R_{\rm therm}$ is strongly energy dependent and therefore it is impossible to define a sharp thermalization radius. Switching off "r" again (bspn) shows that also with "n" included, "r" really dominates the mean energy and shaping of the spectrum.

Table 6.2. Monte Carlo results for Accretion-Phase Model I.

Energy exchange					$\langle\epsilon\rangle_{\rm flux}$	$\langle\epsilon^2\rangle_{\rm flux}$	α	$p_{\rm flux}$	T	η	L_ν
original run					17.5	388.	2.7	0.97	5.2	1.1	14.4
–	–	s	p	–	16.6	362.	2.2	1.01	5.3	−0.3	15.8
b	–	s	p	–	16.3	351.	2.1	1.02	5.4	−2.2	19.1
b	–	–	p	–	17.8	419.	2.1	1.02	5.9	−1.9	20.1
b	r	–	p	–	15.1	285.	3.0	0.96	4.3	1.6	18.6
b	r	s	p	–	14.2	255.	2.8	0.98	4.2	1.1	14.8
b	r	s	p	n	14.4	264.	2.7	0.97	4.3	1.2	17.6
b	–	s	p	n	16.6	358.	2.3	1.00	5.2	0.2	21.7
–	–	s	p	n	16.9	369.	2.4	0.99	5.3	0.4	20.2
b	r	s	–	–	14.0	251.	2.6	0.99	4.3	0.6	13.1
b	r	s	–	n	14.4	263.	2.7	0.97	4.3	1.2	17.0
–	r	s	p	–	14.5	265.	2.8	0.97	4.3	1.2	13.0
–	r	s	p	n	14.7	269.	3.1	0.96	4.2	1.7	16.8
b	r	sn	p	n	14.3	260.	2.7	0.97	4.3	1.2	17.9

Note. — The Energy exchange is specified in Table 6.1. We give $\langle\epsilon\rangle_{\rm flux}$ and T in MeV, $\langle\epsilon^2\rangle_{\rm flux}$ in MeV^2, and L_ν in 10^{51} erg s^{-1}.

To study the relative importance of the different pair processes, we switch off the leptonic ones (row "brs") and compare this to only the leptonic processes (row "rspn"). In this stellar model both types contribute significantly. Comparing then "brsp" with "brsn" shows that among the leptonic processes "n" is clearly more important than "p".

The last row (brsnpn) includes in addition to all other processes scattering on ν_e and $\bar{\nu}_e$. As already shown in Section 3.5, this process is about half as important as scattering on $e^{\pm}$ and its influence on the neutrino flux and spectra is negligible. We show this case for completeness but do not include scattering on ν_e and $\bar{\nu}_e$ for any of our further models.

In order to illustrate some of the cases of Table 6.2 we show in the upper panel of Figure 6.1 several flux spectra from high-statistics Monte Carlo runs. Starting again with the input physics of the original hydrodynamic

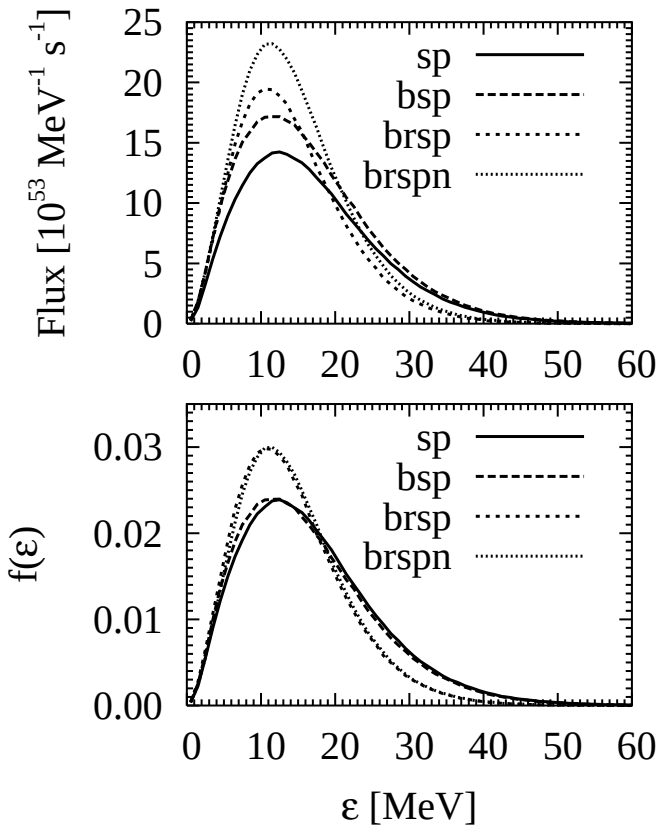

Fig. 6.1.— High-statistics spectra for Accretion-Phase Model I with different input physics as in Table 6.2. *Upper panel:* Differential particle fluxes. *Lower panel:* Spectra normalized to equal particle fluxes.

simulation (sp) we add bremsstrahlung (b), recoil (r), and finally $\nu_e\bar{\nu}_e$ pair annihilation (n). Each of these processes has a significant and clearly visible influence on the curves. The pair-creation processes ("b" and "n") hardly change the spectral shape but increase the number flux, whereas recoil (r) strongly modifies the spectral shape. In the lower panel of Figure 6.1 we show the same curves, normalized to equal particle fluxes. In this representation it is particularly obvious that the pair processes do not affect the spectral shape.

The very different impact of pair processes and nucleon recoils has a simple explanation. The thermalization depth for the pair processes is deeper than that of the energy-exchanging reactions, i.e., the number sphere is below the energy sphere. Therefore, the particle flux is fixed more deeply in the star while the spectra are still modified by energy-exchanging reactions in the scattering atmosphere.

6.3 Steep Power Law

As another example we study the steep power-law model defined in Equation (4.5) and Table 4.1. This model is supposed to represent the outer layers of a late-time proto-neutron star but without being hydrostatically self-consistent. It connects directly with Raffelt (2001), where the same profile was used in a plane parallel setup, studying bremsstrahlung and nucleon recoil. The results of our runs are displayed in Table 6.3 and agree very nicely with those obtained by Raffelt (2001), corresponding to our cases "b" and "br".

For investigating the importance of leptonic processes, we run our code with a variety of neutrino interactions and in addition assume a constant electron fraction Y_e throughout the whole stellar atmosphere. This assumption is somewhat artificial, but gives us the opportunity to study extreme cases in a controlled way. In the relevant region $Y_e = 0.5$ yields the highest possible electron density. In addition we study the electron fraction being one order of magnitude smaller, $Y_e = 0.05$, and finally the extreme case with an equal number of electrons and positrons, $Y_e = 0$.

The first leptonic process we consider is e^+e^- pair annihilation. Comparing the rows "bp" with the row "b" shows a negligible effect on the spectrum, but a rise in luminosity. Increasing Y_e brings the luminosity almost back to the "b" case, because the electron degeneracy rises and the positron density decreases so that the pair process becomes less important.

Adding scattering on $e^\pm$ forces the transported neutrinos to stay closer to the medium temperature, i.e., reduces their mean energy. Of course, the

scattering rate increases with the number density of electrons and positrons, i.e., for higher Y_e we get lower spectral energies. For the luminosity the situation is more complicated. Since the neutrino flux energies decrease when we switch on $e^{\pm}$ scattering we would expect a lower luminosity. However, the opacity of the medium to neutrinos is strongly energy dependent and low energy neutrinos can escape more easily than high-energy ones, increasing the number flux. On balance, the "bsp" luminosities are larger compared to the "bp" ones.

To compare the scattering on $e^{\pm}$ with that on nucleons, we turn off "s" again and instead switch on recoil (r). Qualitatively, the energy exchange is very different from the earlier case. In the scattering on $e^{\pm}$ a neutrino can exchange a large amount of energy, while for scattering on nucleons the energy exchange is small. But since neutrino-nucleon scattering is the dominant source of opacity that keeps the neutrinos inside the star, the scatterings are very frequent. This leads to a stronger suppression in the high-energy tail of the neutrino spectrum and therefore to a visibly smaller mean flux energy

Table 6.3. Monte Carlo results for the steep power-law model.

Energy exchange					Y_e	$\langle\epsilon\rangle_{\rm flux}$	$\langle\epsilon^2\rangle_{\rm flux}$	α	$p_{\rm flux}$	T	η	L_ν
b	–	–	–	–	—	25.8	962.	1.2	1.11	—	—	21.0
b	r	–	–	–	—	19.5	487.	2.6	0.98	6.0	0.7	14.5
b	–	–	p	–	0	25.4	890.	1.6	1.06	—	—	23.8
b	–	–	p	–	0.05	25.6	908.	1.6	1.06	—	—	23.2
b	–	–	p	–	0.5	25.5	917.	1.4	1.08	—	—	21.6
b	–	s	p	–	0	24.2	787.	1.9	1.03	—	—	24.5
b	–	s	p	–	0.05	23.8	753.	2.0	1.02	—	—	24.5
b	–	s	p	–	0.5	21.3	591.	2.3	1.00	6.8	−0.3	23.1
b	r	–	p	–	0.5	20.0	507.	2.7	0.98	6.0	1.0	16.8
b	r	s	p	–	0	20.3	518.	2.9	0.97	5.9	1.4	19.7
b	r	s	p	–	0.05	20.3	518.	2.9	0.97	5.9	1.4	19.5
b	r	s	p	–	0.5	19.6	488.	2.7	0.98	5.9	1.1	18.7
b	r	s	p	n	0	20.7	535.	3.0	0.96	5.8	1.8	23.9
b×3	r	s	p	n	0.05	20.3	522.	2.7	0.97	6.0	1.3	24.2
b	r	s	p	n	0.05	20.6	530.	3.0	0.96	5.9	1.7	23.8
b×0.3	r	s	p	n	0.05	20.7	534.	3.1	0.96	5.8	1.8	23.4
b	r	s	p	n	0.5	19.8	499.	2.7	0.97	5.9	1.2	21.4

and lower effective spectral temperature, but higher α and higher effective degeneracy. Many nucleon scatterings, however, are needed to downgrade the high-energy neutrinos (different from $e^{\pm}$ scattering). Therefore neutrinos stay longer at high energies and experience a larger opacity and a larger amount of backscattering. This suppresses the neutrino flux significantly.

In the runs including both scattering reactions (brsp), we find a mixture of the effects of $e^{\pm}$ and nucleon scatterings and an enhanced reduction of the mean flux energy.

Finally, adding the neutrino pair process yields almost no change in energy and pinching, but an increased luminosity as expected from the analogous case in Section 6.2. Although this profile is rather steep, leptonic pair processes are still important (Figure 4.5).

In order to estimate the sensitivity to the exact treatment of nucleon bremsstrahlung we have performed one run with the bremsstrahlung rate artificially enhanced by a factor of 3, and one where it was decreased by a factor 0.3. All other processes were included. The emerging fluxes and spectra indeed do not depend sensitively on the exact strength of bremsstrahlung as argued in Section 4.3.

6.4 Shallow Power Law

For the shallow power law (Table 6.4) almost the same discussion as for the steep case applies. As we can already infer from Figure 4.6, leptonic processes are more important. This leads to a much higher increase of the neutrino flux once "p" or "n" are included, and to stronger spectral pinching when e^+e^- annihilation is switched on. Scattering on $e^{\pm}$ downgrades the transported neutrino flux by a larger amount.

6.5 Summary

We find that the ν_μ spectra are reasonably well described by the simple picture of a blackbody sphere determined by the thermalization depth of the nucleonic bremsstrahlung process, the "filter effect" of the scattering atmosphere, and energy transfers by nucleon recoils. This is also true for the ν_μ flux in case of steep neutron-star atmospheres. For more shallow atmospheres pair annihilation (e^+e^- and $\nu_e\bar{\nu}_e$), however, yields a large contribution to the emitted ν_μ flux and $e^{\pm}$ scattering reduces the mean flux energy significantly. It is therefore important for state-of-the art transport calculations to include these leptonic processes. The traditional process $e^+e^- \rightarrow \nu_\mu\bar{\nu}_\mu$ is always sub-

dominant compared to $\nu_e\bar{\nu}_e \rightarrow \nu_\mu\bar{\nu}_\mu$. The relative importance of the various reactions depends on the stellar profile.

Neutrinos emitted from a blackbody surface and filtered by a scattering atmosphere without recoils and leptonic processes have an anti-pinched spectrum (Raffelt 2001). However, after all energy-exchanging reactions have been included we find that the spectra are always pinched. When described by our α-fit, α ranges from about 2.5 to 3.5. For an effective Fermi-Dirac distribution, the nominal degeneracy parameter η is typically in the range 1–2, depending on the profile and electron concentration.

The traditional set of neutrino interactions that is commonly included in hydrodynamic SN simulations is not sufficient to account for ν_μ spectra formation. Nucleon recoils significantly lower the mean energy, and bremsstrahlung as well as the $\nu_e\bar{\nu}_e$ pair process cause higher luminosities compared to results obtained with the traditional interactions.

Table 6.4. Monte Carlo results for the shallow power-law model.

Energy exchange					Y_e	$\langle\epsilon\rangle_{\rm flux}$	$\langle\epsilon^2\rangle_{\rm flux}$	α	$p_{\rm flux}$	T	η	L_ν
b	–	–	–	–	—	27.7	1120.	1.2	1.12	—	—	20.3
b	r	–	–	–	—	20.1	521.	2.5	0.99	6.3	0.4	13.4
b	–	–	p	–	0	27.7	974.	2.7	0.98	8.3	1.0	43.1
b	–	–	p	–	0.05	27.9	990.	2.7	0.98	8.3	1.1	43.3
b	–	–	p	–	0.5	28.3	1019.	2.7	0.98	8.5	1.0	38.3
b	–	s	p	–	0	25.5	830.	2.6	0.98	7.6	1.1	46.2
b	–	s	p	–	0.05	25.4	815.	2.8	0.97	7.5	1.2	46.3
b	–	s	p	–	0.5	23.5	706.	2.6	0.98	7.1	1.0	44.8
b	r	–	p	–	0.5	22.5	624.	3.3	0.95	6.1	2.2	33.1
b	r	s	p	–	0	22.3	612.	3.3	0.95	6.1	2.1	39.6
b	r	s	p	–	0.05	22.2	609.	3.2	0.95	6.1	2.1	39.1
b	r	s	p	–	0.5	21.7	585.	3.1	0.95	6.1	1.9	39.2
b	r	s	p	n	0	22.2	608.	3.3	0.94	6.0	2.2	54.7
b	r	s	p	n	0.05	22.4	615.	3.4	0.94	6.1	2.3	54.9
b	r	s	p	n	0.5	21.8	587.	3.3	0.95	6.1	1.9	51.3

Chapter 7

Comparison of All Flavors

The new energy-exchange channels studied in the previous section lower the average ν_μ energies. In order to compare the ν_μ fluxes and spectra with those of ν_e and $\bar{\nu}_e$ we perform a new series of runs where we include the full set of relevant microphysics for ν_μ and also simulate the transport of ν_e and $\bar{\nu}_e$.

Our findings for ν_e and $\bar{\nu}_e$ agree with the previous literature, whereas our results for ν_μ show lower mean energies. The mean energies of $\bar{\nu}_e$ and ν_μ are almost equal. The ν_μ luminosity can differ from that of ν_e and $\bar{\nu}_e$ by up to a factor of 2. Weak magnetism causes a difference between the mean energies of ν_μ and $\bar{\nu}_\mu$ of a few per cent.

We present an overview of the results obtained by other groups and find that the more recent simulations agree rather well on the differential effects in energies and luminosities of the different flavors. These findings as well as our results suggest that assumptions commonly made for calculating oscillation effects, i.e., equal luminosities and a difference in the mean energies of $\bar{\nu}_e$ and $\bar{\nu}_\mu$ of up to a factor of 2, need to be changed.

We show results of the detailed spectral shapes obtained in our simulations. Our α fit describes the spectra slightly better than a nominal Fermi-Dirac distribution.

Parts of this chapter were already published in a similar form as:
M. T. Keil, G. G. Raffelt, and H. T. Janka, "Monte Carlo study of supernova neutrino spectra formation," Astrophys. J. in press, astro-ph/0208035.

7.1 Results from Our Monte Carlo Study

For our ν_e and $\bar{\nu}_e$ transport we employ the same microphysics as in Janka & Hillebrandt (1989a,b), i.e., charged-current reactions of $e^\pm$ with nucleons, isoenergetic scattering on nucleons, scattering on $e^\pm$, and e^+e^- pair annihilation.

In principle one should also include nucleon bremsstrahlung and the effect of nucleon recoils for the transport of $\nu_{\rm e}$ and $\bar{\nu}_{\rm e}$, but their effects will be minimal. Therefore, we preferred to leave the original working code unmodified for these flavors.

In the first three rows of Table 7.1 we give the spectral characteristics for the Accretion-Phase Model I from the original simulation of Messer. The usual hierarchy of average neutrino energies is found, i.e., $\langle\epsilon_{\nu_{\rm e}}\rangle : \langle\epsilon_{\bar{\nu}_{\rm e}}\rangle : \langle\epsilon_{\nu_\mu}\rangle = 0.86 : 1 : 1.20$. The luminosities are essentially equal between $\bar{\nu}_{\rm e}$ and $\nu_{\rm e}$ while ν_μ, $\bar{\nu}_\mu$, ν_τ, and $\bar{\nu}_\tau$ each provide about half of the $\bar{\nu}_{\rm e}$ luminosity.

Our Monte Carlo runs of this profile establish the same picture for the same input physics (label "sp"). Although our mean energies are slightly offset to lower values for all flavors relative to the original run, our energies relative to each other are $\langle\epsilon_{\nu_{\rm e}}\rangle : \langle\epsilon_{\bar{\nu}_{\rm e}}\rangle : \langle\epsilon_{\nu_\mu}\rangle = 0.84 : 1 : 1.19$ and thus very similar. However, once we include all energy exchanging processes (brspn) we find $0.84 : 1 : 1.02$ instead. Therefore, $\langle\epsilon_{\nu_\mu}\rangle$ no longer exceeds $\langle\epsilon_{\bar{\nu}_{\rm e}}\rangle$ by much. The luminosity of ν_μ is about half that of $\nu_{\rm e}$ or $\bar{\nu}_{\rm e}$ which are approximately equal, in rough agreement with the original results. Even though the additional processes lower the mean energy of ν_μ they yield a more than 10% higher ν_μ luminosity, mainly due to $\nu_{\rm e}\bar{\nu}_{\rm e}$ annihilation.

Different rates for neutrinos and anti-neutrinos arise due to the weak magnetism correction of the neutrino-nucleon scattering cross section (Section 3.3). The next two lines (wm) show results from runs where we included weak magnetism in our ν_μ transport. Weak magnetism causes a significant correction to the neutrino-nucleon cross section that mainly arises due to the large anomalous magnetic moments of protons and neutrons (Vogel & Beacom 1999, Horowitz 2002). It increases the neutrino interaction rate but lowers the rate for anti-neutrinos. It is expected to be a small correction in the SN context, but has never been implemented for ν_μ and $\bar{\nu}_\mu$ so far. Following Horowitz (2002) we add weak magnetism to our nucleon-recoil rate as given in Section 3.3.

Our Monte Carlo code transports only one species of neutrinos at a time. In order to test the impact of weak magnetism we assumed that a chemical potential for ν_μ would build up, and assumed a fixed value for the ν_μ degeneracy parameter throughout our stellar model. We then iterated several runs for ν_μ and $\bar{\nu}_\mu$ with different degeneracy parameters until their particle fluxes were equal because in a stationary state there will be no net flux of μ-lepton number.

We performed this procedure for our Accretion-Phase Model I. The mean energy of ν_μ goes down by 1% and goes up for $\bar{\nu}_\mu$ by 4%. The mean luminosities change in opposite directions by about 2–3%. Since we adjusted the particle fluxes by hand in order to fix the chemical potential, we cannot claim

Table 7.1. Comparing Monte Carlo results for different flavors.
Accretion-Phase Models

Flavor	$\langle\epsilon\rangle_{\rm flux}$	$\langle\epsilon^2\rangle_{\rm flux}$	$\frac{\langle\epsilon\rangle_{\rm flux}}{\langle\epsilon_{\bar\nu_{\rm e}}\rangle_{\rm flux}}$	α	$p_{\rm flux}$	T	η	L_ν
Accretion-Phase Model I								
Original								
ν_μ, $\bar\nu_\mu$	17.5	388.	1.20	2.7	0.97	5.2	1.1	14.4
$\bar\nu_{\rm e}$	14.6	253.	1	4.4	0.91	3.5	3.4	29.2
$\nu_{\rm e}$	12.5	190.	0.86	3.6	0.93	3.2	2.8	30.8
Our runs								
ν_μ, $\bar\nu_\mu$ (sp)	16.6	362.	1.19	2.2	1.01	5.3	−0.3	15.8
ν_μ, $\bar\nu_\mu$ (brspn)	14.3	260.	1.02	2.7	0.97	4.3	1.2	17.9
ν_μ (wm)	14.2	254.	1.01	2.9	0.96	4.1	1.6	17.4
$\bar\nu_\mu$ (wm)	14.9	281.	1.06	2.8	0.97	4.3	1.5	18.3
$\bar\nu_{\rm e}$	14.0	237.	1	3.8	0.93	3.6	2.7	31.7
$\nu_{\rm e}$	11.8	175.	0.84	2.9	0.97	3.4	1.4	31.9
Accretion-Phase Model II								
Original								
ν_μ, $\bar\nu_\mu$	17.2	380.	1.09	2.5	0.98	5.2	0.8	32.4
$\bar\nu_{\rm e}$	15.8	300.	1	4.0	0.92	4.0	3.0	68.1
$\nu_{\rm e}$	12.9	207.	0.82	3.1	0.96	3.7	1.7	65.6
Our runs								
ν_μ, $\bar\nu_\mu$	15.7	317.	1.02	2.5	0.98	4.8	0.8	27.8
$\bar\nu_{\rm e}$	15.4	283.	1	4.2	0.92	3.8	3.2	73.5
$\nu_{\rm e}$	13.0	207.	0.84	3.4	0.95	3.6	2.1	73.9

Note. — We give $\langle\epsilon\rangle_{\rm flux}$ and T in MeV, $\langle\epsilon^2\rangle_{\rm flux}$ in MeV^2, L_ν in 10^{51} erg s^{-1}.

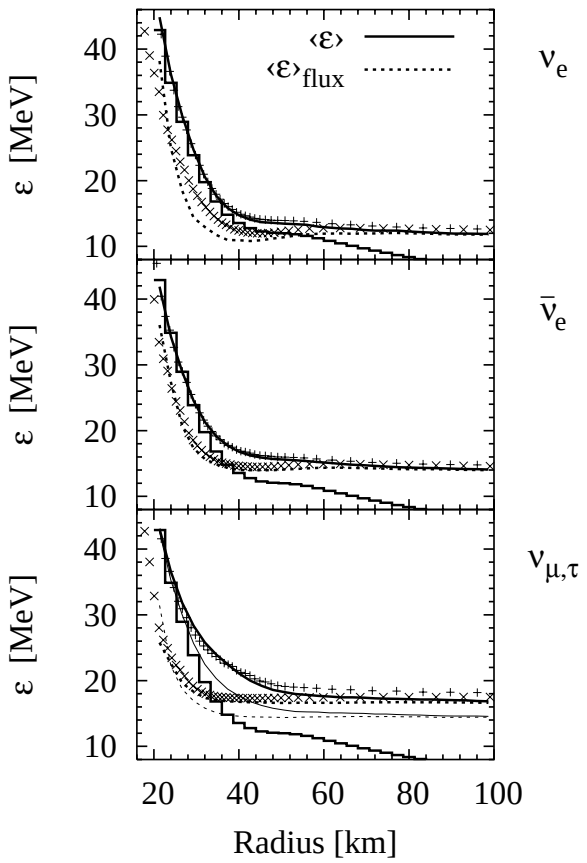

Fig. 7.1.— Comparison of the Accretion-Phase Model I calculations. Continuous lines show our Monte Carlo runs while crosses represent the original simulation by Messer. The steps correspond to $\langle\epsilon\rangle = 3.15\,T$. Thin lines in the lower panel represent our findings after including the full set of relevant interaction processes.

an effect on the luminosities.

In Figure 7.1 we compare our calculations for the Accretion-Phase Model I with those of the original simulation. The step-like curve represents the mean energy of neutrinos in LTE for zero chemical potential. The smooth solid line is the mean energy $\langle\epsilon\rangle$ from our runs, the dotted line gives $\langle\epsilon\rangle_{\rm flux}$. The crosses are the corresponding results from the original runs. In the case of ν_μ (lower panel) we show the results of our "sp" run as thick lines and the results of our "brspn" run, i.e., the complete set of interactions included, as thin lines. The boundaries of our simulation domain were the same for all flavors, namely $R_{\rm in} = 20$ km and $R_{\rm out} = 100$ km.

As another example of an accreting proto-neutron star we use the

Accretion-Phase Model II. The neutrino interactions included in this model were nucleon bremsstrahlung, scattering on $e^{\pm}$, and e^+e^- annihilation. Nucleon correlations, effective mass, and recoil were taken into account, following Burrows & Sawyer (1998, 1999), as well as weak magnetism effects (Horowitz 2002) and quenching of g_A at high densities (Carter & Prakash 2002). All these improvements to the traditional microphysics affect mainly ν_μ and to some degree also $\bar{\nu}_e$. Weak magnetism terms decrease the nucleon scattering cross sections for $\bar{\nu}_\mu$ more strongly than they modify ν_μ scatterings. In this hydrodynamic calculation, however, ν_μ and $\bar{\nu}_\mu$ were treated identically by using the average of the corresponding reaction cross sections. The effects of weak magnetism on the transport of ν_μ and $\bar{\nu}_\mu$ are therefore not included to very high accuracy. Note, moreover, that the original data come from a general relativistic hydrodynamic simulation with the solution of the Boltzmann equation for neutrino transport calculated in the comoving frame of the stellar fluid. Therefore the neutrino results are affected by gravitational redshift and, depending on where they are measured, may also be blueshifted by Doppler effects due to the accretion flow to the nascent neutron star.

Our Monte Carlo simulation in contrast was performed on a static background without general relativistic corrections. It includes bremsstrahlung, recoil, e^+e^- pair annihilation, scattering on $e^{\pm}$, and $\nu_e\bar{\nu}_e$ annihilation, i.e., our microphysics is similar but not identical with that used in the original run. As an outer radius we took 100 km; all flux parameters are measured at this radius because farther out Doppler effects of the original model would make it difficult to compare the results. Keeping in mind that we use very different numerical approaches and somewhat different input physics, the agreement in particular for ν_e and $\bar{\nu}_e$ is remarkably good. This agreement shows once more that our Monte Carlo approach likely captures at least the differential effects of the new microphysics in a satisfactory manner.

For the Accretion-Phase Model II we show the comparison with our runs in Figure 7.2. In this case, for the transport of ν_μ our inner boundary is $R_{\rm in} = 16$ km, while for ν_e and $\bar{\nu}_e$ we use $R_{\rm in} = 24$ km. For ν_e and $\bar{\nu}_e$ the charged-current processes (urca) keep these neutrinos in LTE up to larger radii than pair processes in the case of ν_μ. With our choice of $R_{\rm in}$ the neutrinos are in LTE within the innermost radial zones. In this profile our choice of boundaries reduces the CPU time needed and does not affect the results. As stated before outer boundaries were chosen to be at $R_{\rm out} = 100$ km.

The results are similar to the Accretion-Phase Model I. The luminosities are not equipartitioned but instead follow roughly $L_{\nu_e} \approx L_{\bar{\nu}_e} \approx 2\,L_{\nu_\mu}$. The ratios of mean energies are $\langle\epsilon_{\nu_e}\rangle : \langle\epsilon_{\bar{\nu}_e}\rangle : \langle\epsilon_{\nu_\mu}\rangle = 0.82 : 1 : 1.09$ in the original run and $0.84 : 1 : 1.02$ in our run.

In summary, both accretion-phase models agree reasonably well in the

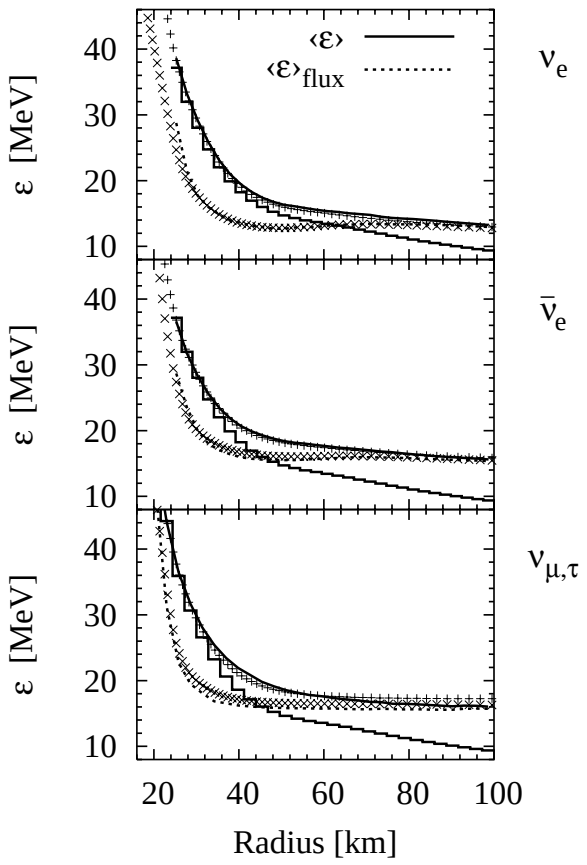

Fig. 7.2.— Same as Figure 7.1 for the Accretion-Phase Model II.

$\langle \epsilon_{\nu_e} \rangle : \langle \epsilon_{\bar{\nu}_e} \rangle$ ratio for all runs. Moreover, using traditional input physics one finds something like $\langle \epsilon_{\bar{\nu}_e} \rangle : \langle \epsilon_{\nu_\mu} \rangle = 1 : 1.20$. Depending on the implementation of the new input physics and depending on the model one finds results between $\langle \epsilon_{\bar{\nu}_e} \rangle : \langle \epsilon_{\nu_\mu} \rangle = 1 : 1.02$ and $1 : 1.09$.

In order to estimate the corresponding results for later stages of the proto-neutron star evolution we employ our steep power-law model. We vary the power q of the temperature profile within a reasonable range so that $q/p =$ 0.25–0.35, with q and p defined in Equation (4.5). Y_e is fixed by demanding roughly equal number fluxes for ν_e and $\bar{\nu}_e$ because a few seconds after bounce deleptonization should be essentially complete. The fluxes of these neutrinos depend very sensitively on Y_e so that this constraint is only reached to within about 30% without tuning Y_e to three decimal places. However, the mean energies are rather insensitive to the exact value of Y_e. This is illustrated in the first section of Table 7.2 by the steep power-law model with $q = 2.5$ where we show results for $Y_e = 0.15$ and 0.20. The number fluxes of ν_e and $\bar{\nu}_e$

Table 7.2. Comparing Monte Carlo results for different flavors.
Power-Law Models

Flavor	Y_e	$\langle\epsilon\rangle_{\rm flux}$	$\langle\epsilon^2\rangle_{\rm flux}$	$\frac{\langle\epsilon\rangle_{\rm flux}}{\langle\epsilon_{\bar{\nu}_e}\rangle_{\rm flux}}$	α	$p_{\rm flux}$	T	η	L_ν
Steep Power Law $p = 10$									
$q = 2.5$									
ν_μ, $\bar{\nu}_\mu$	0.15	20.4	525.	1.10	2.8	0.96	5.9	1.5	23.5
$\bar{\nu}_e$	0.15	18.5	413.	1	3.8	0.92	4.6	3.0	23.5
ν_e	0.15	12.7	198.	0.69	3.4	0.94	3.4	2.4	12.8
ν_μ, $\bar{\nu}_\mu$	0.2	20.4	521.	1.14	3.0	0.97	5.9	1.5	23.3
$\bar{\nu}_e$	0.2	17.9	383.	1	4.1	0.92	4.4	3.1	11.7
ν_e	0.2	13.4	218.	0.75	3.7	0.93	3.4	2.9	24.4
$q = 3.0$									
ν_μ, $\bar{\nu}_\mu$	0.1	17.7	393.	1.14	2.9	0.96	5.0	1.8	12.7
$\bar{\nu}_e$	0.1	15.5	289.	1	3.9	0.93	4.0	2.8	8.8
ν_e	0.1	10.5	132.	0.68	4.1	0.92	2.6	3.0	6.6
$q = 3.5$									
ν_μ, $\bar{\nu}_\mu$	0.07	15.8	310.	1.22	3.1	0.95	4.4	2.1	7.9
ν_μ (wm)	0.07	15.5	296.	1.19	3.3	0.94	4.2	2.3	7.7
$\bar{\nu}_\mu$ (wm)	0.07	16.5	337.	1.27	3.2	0.95	4.5	2.1	8.3
$\bar{\nu}_e$	0.07	13.0	207.	1	3.4	0.94	3.5	2.3	4.3
ν_e	0.07	9.4	103.	0.72	5.0	0.90	2.1	3.9	4.1
Shallow Power Law $p = 5$, $q = 1$									
ν_μ, $\bar{\nu}_\mu$	0.3	22.0	596.	1.14	3.3	0.94	6.0	2.2	53.9
$\bar{\nu}_e$	0.3	19.3	440.	1	4.5	0.91	4.5	3.7	85.7
ν_e	0.3	14.7	262.	0.76	3.7	0.93	3.8	2.7	56.5

differ by less than 30% for $Y_e = 0.15$, but differ by a factor of 3 for $Y_e = 0.2$. At the same time, the average spectral energies barely change.

The ratios of mean energies are not very different from those of the accretion-phase models. Of course, the absolute flux energies have no physical meaning because we adjusted the stellar profile in order to obtain realistic values. For the luminosities we find $L_{\nu_e} < L_{\nu_\mu}$, different from the accretion phase. The steep power law implies that the radiating surfaces are similar for all flavors so that it is not surprising that the flavor with the largest energies also produces the largest luminosity.

For our steepest profile we also performed runs including weak magnetism, because this should probe how much spectra are affected in late-time profiles. As already found for the Accretion-Phase Model I, the mean energy of $\bar{\nu}_\mu$ goes up by 4%, whereas in the case of ν_μ it decreases by 1%. The mean luminosities are almost unaffected. We conclude that weak-magnetism corrections are small. Transporting ν_μ and $\bar{\nu}_\mu$ separately in a self-consistent hydrodynamic simulation is probably not worth the cost in computer time.

We find that $\langle \epsilon_{\nu_\mu} \rangle$ always exceeds $\langle \epsilon_{\bar{\nu}_e} \rangle$ by a small amount, the exact value depending on the stellar model. During the accretion phase the energies seem to be almost identical, later they may differ by up to 20%. We have not found a model where the energies differ by the large amounts which are sometimes assumed in the literature. At late times when Y_e is small the microphysics governing $\bar{\nu}_e$ transport is closer to that for ν_μ than at early times. Therefore, one expects that at late times the behavior of $\bar{\nu}_e$ is more similar to ν_μ than at early times. We do not see any argument for expecting an extreme hierarchy of energies at late times for self-consistent stellar models.

We never find exact equipartition of the flavor-dependent luminosities. Depending on the stellar profile the fluxes can mutually differ by up to a factor of 2 in either direction.

7.2 Previous Literature

Studies of oscillation effects in SN neutrino spectra usually assume exactly equal neutrino luminosities for all flavors and a strong hierarchy for the mean energies. Often times they assume the difference between the mean energies of $\bar{\nu}_e$ and $\bar{\nu}_\mu$ to be about a factor of 2. We find an almost orthogonal picture in our simulations. Where does this come from?

To the best of our knowledge, except in the very recent models by Buras et al. (2003b), the microphysics employed for ν_μ transport was roughly the same in all published simulations. It included iso-energetic scattering on nucleons, e^+e^- annihilation and $\nu_\mu e^\pm$ scattering. Of course, the transport method and

the numerical implementation of the neutrino processes differ in the codes of different groups. The new results of self-consistent calculations point in the same direction as the findings from our Monte Carlo studies presented in the previous chapter. Therefore these findings are almost orthogonal to the previous assumptions oscillation studies are based on. Our representative sample of pertinent results is summarized in Table 7.3. We have also included our Accretion-Phase Models I and II and a very recent model by the Garching group including all relevant processes. Note that the simulations discussed below did not in all cases use the same stellar models and equations of state for the dense matter in the SN core.

We begin with the simulations of the Livermore group who find robust explosions by virtue of the neutron-finger convection phenomenon. Neutrino transport is treated in the hydrodynamic models with a multigroup flux-limited diffusion scheme. Mayle, Wilson, & Schramm (1987) gave detailed results for their SN simulation of a $25\,M_\odot$ star. For half a second after bounce they obtained a somewhat oscillatory behavior of the neutrino luminosities. After the prompt peak of the electron neutrino luminosity, they got $L_{\nu_\mathrm{e}} \approx L_{\bar{\nu}_\mathrm{e}} \approx 2\,L_{\nu_\mu} \approx 50$–$130 \times 10^{51}$ erg s^{-1}. After about one second the values stabilize. This calculation did not produce the "standard" hierarchy of energies. However, there is clearly a tendency that $\bar{\nu}_\mathrm{e}$ behave more similar to ν_μ at late times.

The most recent published Livermore simulation is a $20\,M_\odot$ star (Totani et al. 1998). It shows an astonishing degree of luminosity equipartition from the accretion phase throughout the early Kelvin-Helmholtz cooling phase. About two seconds after bounce the ν_μ flux falls off more slowly than the other flavors. In Table 7.3 we show representative results for an early and a late time. The mean energies and their ratios are consistent with what we would have expected on the basis of our study.

With a different numerical code, Bruenn (1987) found for a $25\,M_\odot$ progenitor qualitatively different results for luminosities and energies. At about 0.5 s after bounce the luminosities and energies became stable at the values given in Table 7.3. This simulation is an example for an extreme hierarchy of mean energies.

In Burrows (1988) all luminosities are said to be equal. In addition it is stated that for the first 5 seconds $\langle\epsilon_{\nu_\mu}\rangle \approx 24$ MeV and the relation to the other flavors is $\langle\epsilon_{\nu_\mathrm{e}}\rangle : \langle\epsilon_{\bar{\nu}_\mathrm{e}}\rangle : \langle\epsilon_{\nu_\mu}\rangle = 0.9 : 1 : 1.8$. Detailed results are only given for $\bar{\nu}_\mathrm{e}$, so we are not able to add this reference to our table. The large variety of models investigated by Burrows (1988) and the detailed results for $\bar{\nu}_\mathrm{e}$ go beyond the scope of our brief description. In a later paper Myra & Burrows (1990) studied a $13\,M_\odot$ progenitor model and found the extreme hierarchy of energies shown in our table.

Table 7.3. Flavor dependent flux characteristics from the literature.

	tpb	$\langle\epsilon_{\nu_e}\rangle$	$\langle\epsilon_{\bar{\nu}_e}\rangle$	$\langle\epsilon_{\nu_\mu}\rangle$	$\frac{\langle\epsilon_\nu\rangle}{\langle\epsilon_{\bar{\nu}_e}\rangle}$	L_{ν_e}	$L_{\bar{\nu}_e}$	L_{ν_μ}
Mayle et al. (1987)	1.0	12	24	22	0.50 : 1 : 0.92	20	20	20
Totani et al. (1998)	0.3	12	15	19	0.80 : 1 : 1.26	20	20	20
	10	11	20	25	0.55 : 1 : 1.25	0.5	0.5	1
Bruenn (1987)	0.5	10	12	25	0.83 : 1 : 2.08	3	5	16
Myra & Burrows (1990)	0.13	11	13	24	0.85 : 1 : 1.85	30	30	16
Janka & Hillebrandt (1989b)	0.3	8	14	16	0.57 : 1 : 1.14	30	220	65
Suzuki (1989)	1	9.5	13	15	0.73 : 1 : 1.15	4	4	3
	20	8	10	9	0.80 : 1 : 0.90	0.3	0.3	0.07
Suzuki (1991)	1	9.5	13	15	0.73 : 1 : 1.15	3	3	3
	15	8	9	9.5	0.89 : 1 : 1.06	0.4	0.4	0.3
Suzuki (1993)	1	9	12	13	0.75 : 1 : 1.08	3	3	3
	15	7	8	8	0.88 : 1 : 1.00	0.3	0.3	0.3
Accretion-Phase Model I (original)	0.32	13	15	18	0.86 : 1 : 1.20	31	29	14
Accretion-Phase Model I (our run)	0.32	12	14	14	0.84 : 1 : 1.02	32	32	18
Accretion-Phase Model II (original)	0.15	13	16	17	0.82 : 1 : 1.09	66	68	32
Accretion-Phase Model II (our run)	0.15	13	15	16	0.84 : 1 : 1.02	74	74	28
Buras et al. (personal comm.)	0.25	14.1	16.5	16.8	0.85 : 1 : 1.02	43	44	32

Table 7.3—Continued

	tpb	$\langle\epsilon_{\nu_e}\rangle$	$\langle\epsilon_{\bar{\nu}_e}\rangle$	$\langle\epsilon_{\nu_\mu}\rangle$	$\frac{\langle\epsilon_\nu\rangle}{\langle\epsilon_{\bar{\nu}_e}\rangle}$	L_{ν_e}	$L_{\bar{\nu}_e}$	L_{ν_μ}
The following lines show $\langle\epsilon\rangle_{\mathrm{rms}}$ instead of $\langle\epsilon\rangle$								
Mezzacappa et al. (2001)	0.5	16	19	24	0.84 : 1 : 1.26	25	25	8
Liebendörfer et al. (2001)	0.5	19	21	24	0.90 : 1 : 1.14	30	30	10

Note. — We give the time post bounce (tpb) in s, $\langle\epsilon\rangle$ in MeV, and L_ν in 10^{51} erg s^{-1}.

With the original version of our code Janka & Hillebrandt (1989b) performed their analyses for a 20 $M_\odot$ progenitor from a core-collapse calculation by Hillebrandt (1987). Of course, like our present study, these were Monte Carlo simulations on a fixed background model, not self-consistent simulations. Taking into account the different microphysics the mean energies are consistent with our present work. The mean energies of ν_e were somewhat on the low side relative to $\bar{\nu}_e$ and the $\bar{\nu}_e$ luminosity was overestimated. Both can be understood by the fact that the stellar background contained an overly large abundance of neutrons, because the model resulted from a post-bounce calculation which only included electron neutrino transport.

Suzuki (1989) studied models with initial temperature and density profiles typical of proto-neutron stars at the beginning of the Kelvin-Helmholtz cooling phase about half a second after bounce. He used the relatively stiff nuclear equation of state developed by Hillebrandt & Wolff (1985). In our table we show the results of the model C12. From Suzuki (1991) we took the model labeled C20 which includes bremsstrahlung. The model C48 from Suzuki (1993) includes multiple-scattering suppression of bremsstrahlung. Suzuki's models are the only ones from the previous literature which go beyond the traditional microphysics for ν_μ transport. It is reassuring that his ratios of mean energies come closest to the ones we find.

Over the past few years, first results from Boltzmann solvers coupled with hydrodynamic simulations have become available, for example the unpublished ones that we used as our Accretion-Phase Models I and II. For convenience we include them in Table 7.3. Further, we include a very recent accretion-phase model of the Garching group (Buras et al., personal communication) that includes the full set of microphysical input. Finally, we include two simulations similar to the Accretion-Phase Model I, one by Mezzacappa et al. (2001) and the other by Liebendörfer et al. (2001). These latter papers show rms energies instead of mean energies. Recalling that the former tend to be about 45% larger than the latter these results are entirely consistent with our accretion-phase models. Moreover, the ratios of $\langle\epsilon\rangle_{\rm rms}$ tend to exaggerate the spread between the flavor-dependent mean energies because of different amounts of spectral pinching, i.e., different effective degeneracy parameters. To illustrate this point we take the first two rows from Table 7.1 as an example. The ratio of the mean energies $\langle\epsilon_1\rangle = 17.5$ MeV and $\langle\epsilon_2\rangle = 14.6$ MeV is $\langle\epsilon_1\rangle/\langle\epsilon_2\rangle = 1.19$. Using Equation 5.14 for $\alpha_1 = 2.7$ and $\alpha_2 = 4.4$ the ratio of rms energies equals 1.31.

To summarize, the frequently assumed exact equipartition of the emitted energy among all flavors appears only in some simulations of the Livermore group and some by Suzuki. We note that the flavor-dependent luminosities tend to be quite sensitive to the detailed atmospheric structure and chemical

composition. On the other hand, the often-assumed extreme hierarchy of mean energies was only found in the early simulations of Bruenn (1987) and of Myra & Burrows (1990), possibly a consequence of the neutron-star equation of state used in these calculations.

If we ignore results which appear to be "outliers", the picture emerging from Table 7.3 is quite consistent with our own findings. For the luminosities, typically $L_{\nu_e} \approx L_{\bar{\nu}_e}$ and a factor of 2–3 between this and L_{ν_μ} in either direction, depending on the evolutionary phase. For the mean energies we read typical ratios in the range of $\langle\epsilon_{\nu_e}\rangle : \langle\epsilon_{\bar{\nu}_e}\rangle : \langle\epsilon_{\nu_\mu}\rangle = 0.8\text{–}0.9 : 1 : 1.0\text{–}1.3$. The more recent simulations involving a Boltzmann solvers show a consistent behavior and will in future provide reliable information about neutrino fluxes and spectra. There is a clear tendency that the inclusion of all relevant microphysics decreases the hierarchy of mean energies.

Analyzing detected neutrino spectra from a future galactic SN will demand very accurate predictions from self-consistent simulations. This is necessary for both, a possible measurement of neutrino oscillation parameters and also for testing the current SN paradigm.

7.3 Spectral Shape

Thus far we have characterized the neutrino spectra by a few simple parameters. However, it is extremely useful to have a simple analytic fit to the overall spectrum that can be used, for example, to simulate the response of a neutrino detector to a SN signal. To study the quality of different fit functions we have performed a few high-statistics Monte Carlo runs for the Accretion-Phase Model I and two of the steep power-law models ($p = 10$, $q = 2.5$ and 3.5) including all interaction processes. Moreover, we have performed these runs for the flavors ν_e, $\bar{\nu}_e$, and ν_μ.

In order to get smooth spectral curves we have averaged the output of 70,000 time steps. In addition we have refined the energy grid of the neutrino interaction rates. Both measures leave the previous results unaffected but increase computing time and demand for memory significantly.

In Figure 7.3 we show our high-statistics Monte Carlo spectra (MC) for the Accretion-Phase Model I together with the α-fit function $f_\alpha(\epsilon)$ defined in Equation (5.9) and the η-fit function $f_\eta(\epsilon)$ of Equation (5.15). The analytic functions can only fit the spectrum well over a certain range of energies. We have chosen to optimize the fit for the event spectrum in a detector, assuming the cross section scales with ϵ^2. Therefore, we actually show the neutrino flux spectra multiplied with ϵ^2. Accordingly, the parameters α and $\bar{\epsilon}$, as well as η and T and the normalizations are determined such that the energy moments

$\langle\epsilon^2\rangle$, $\langle\epsilon^3\rangle$, and $\langle\epsilon^4\rangle$ are reproduced by the fits.

Below each spectrum we show the ratio of our Monte Carlo results with the fit functions. In the energy range where the statistics in a detector would be reasonable for a galactic SN, say from 5–10 MeV up to around 40 MeV, both types of fits represent the Monte Carlo results nicely. However, in all cases the α-fit works somewhat better than the η-fit.

We have repeated this exercise for the steep power-law models with $q = 2.5$ and the one with $q = 3.5$ and show the results in Figures 7.5 and 7.4, respectively. The quality of the fits is comparable to the previous example.

7.4 Summary

In comparing the spectra of all neutrino flavors we find a consistent behavior of all the considered models. Once all relevant interactions are included the differences between $\bar{\nu}_\mathrm{e}$ and ν_μ spectra become rather small. Concerning mean energies from our two realistic profiles that represent the accretion phase, we always find $\langle\epsilon_{\nu_\mathrm{e}}\rangle : \langle\epsilon_{\bar{\nu}_\mathrm{e}}\rangle : \langle\epsilon_{\nu_\mu}\rangle = 0.8\text{–}0.9 : 1 : 1.0\text{–}1.09$. These findings are completely consistent with full hydrodynamic simulations that include the full set of interactions, i.e., the recent Garching-group models. For the luminosities we find good agreement, too. The runs commonly show $L_{\nu_\mathrm{e}} \approx L_{\bar{\nu}_\mathrm{e}} \approx 2\,L_{\nu_\mu}$.

For our power-law models we find somewhat stronger hierarchies in the mean energies. It is not clear if this will still hold in self-consistent simulations. There are currently no self-consistent models with an accurate treatment of the neutrino transport available that continued the calculations to the late phases where steep proto-neutron-star profiles are found.

In our collection of previous literature we found a variety of different predictions. The strong hierarchies in mean energies that were commonly assumed in the literature for calculating neutrino-oscillation effects are rather outliers. Also the exact equipartition of luminosities is not found in elaborate neutrino transport models.

The standard picture of flavor-dependent SN neutrino spectra needs to be changed. Oscillation studies should allow for large differences in the $\bar{\nu}_\mathrm{e}$ and $\bar{\nu}_\mu$ luminosities, and for almost equal mean energies of these flavors. Results of different self-consistent simulations show large variations in their absolute values. Therefore, only concepts that rely on differential effects of flavor-dependent SN neutrino spectra can have predictive power for identifying oscillation signatures.

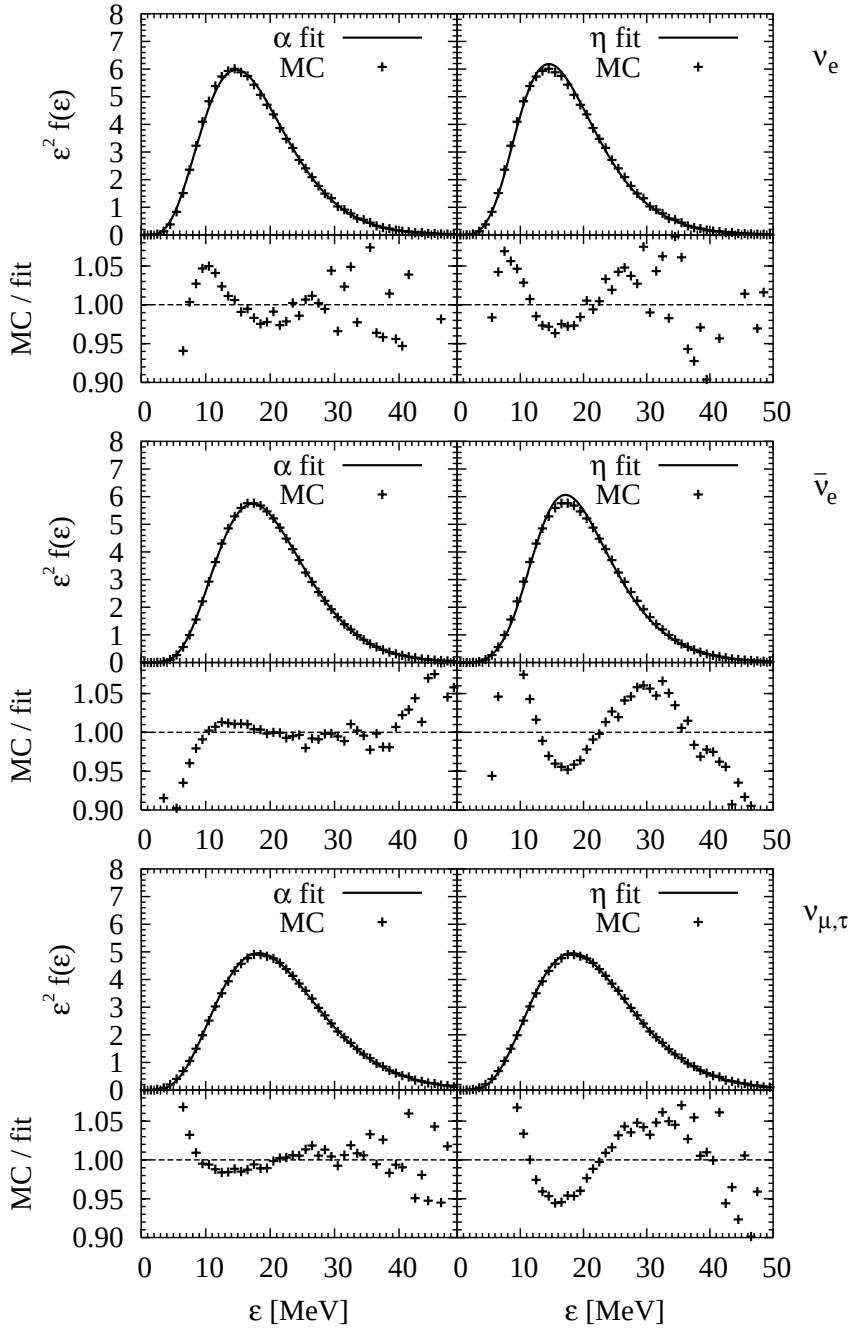

Fig. 7.3.— High-statistics spectra for Accretion-Phase Model I including all interaction processes. The Monte Carlo (MC) results are shown as crosses, the analytic fit functions as smooth lines. The left-hand panels use as fits $f_\alpha(\epsilon)$ according to Equation (5.9), the right-hand panels $f_\eta(\epsilon)$ according to Equation (5.15). Below the spectra we show the ratio between Monte Carlo and fit.

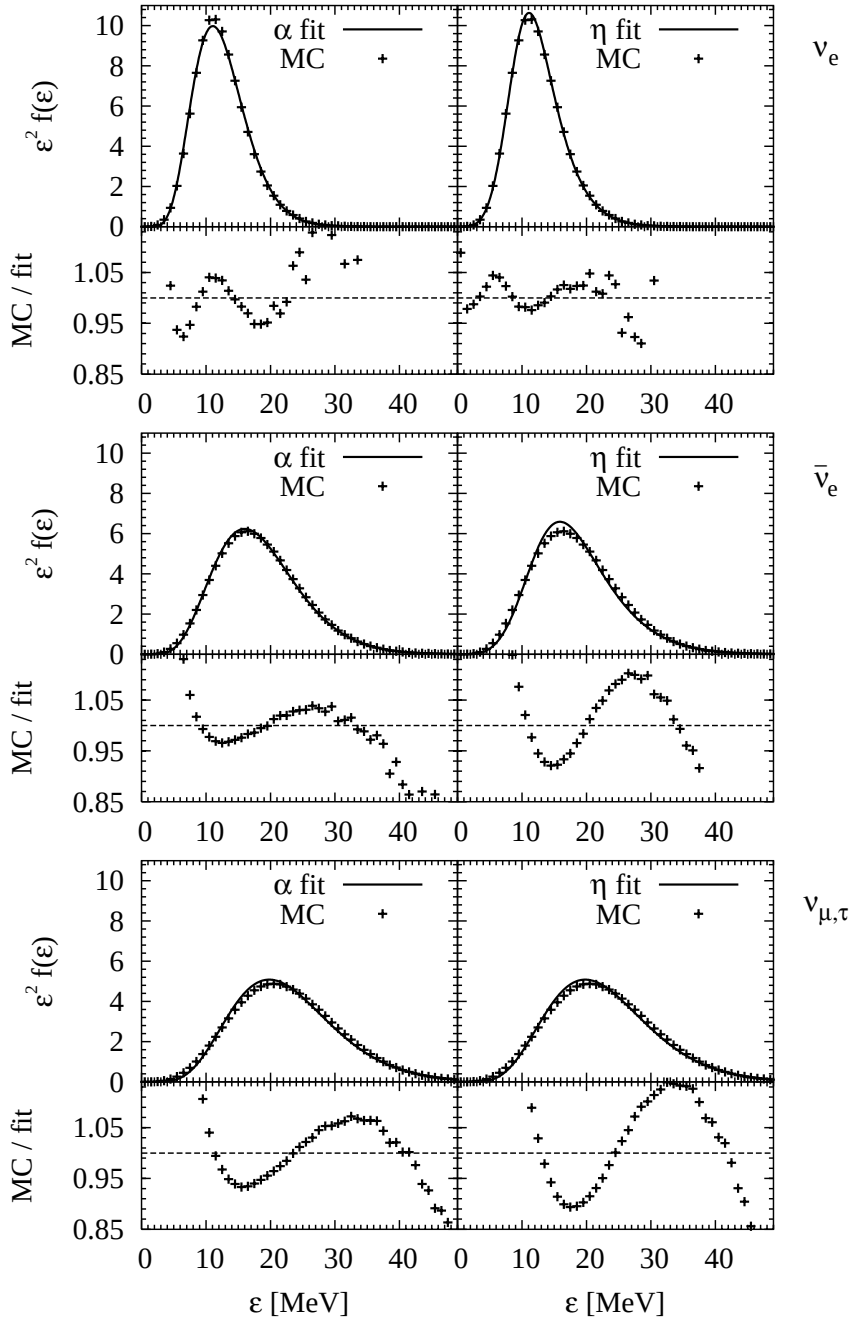

Fig. 7.4.— Same as Figure 7.3 for the $p = 10$, $q = 3.5$ power law.

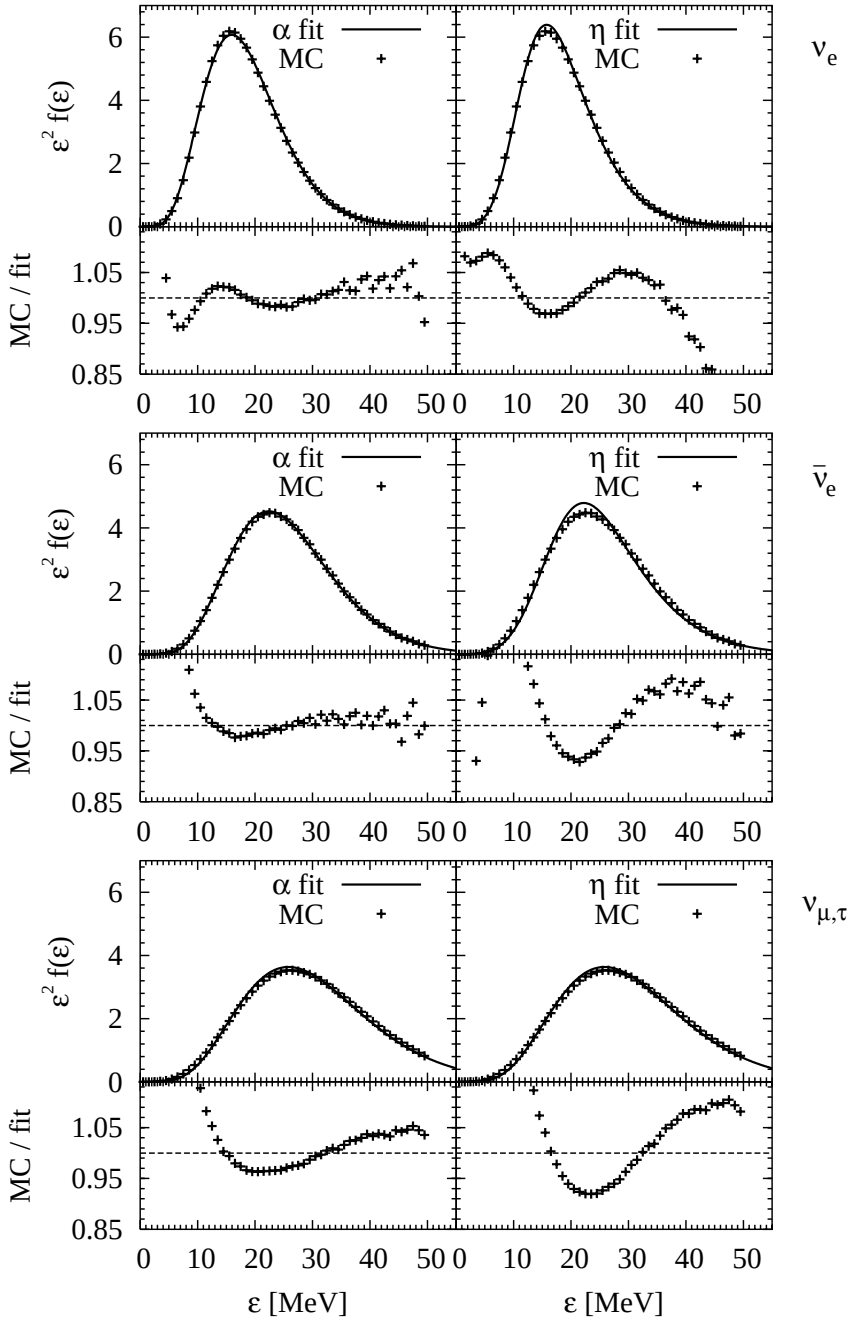

Fig. 7.5.— Same as Figure 7.3 for the $p = 10$, $q = 2.5$ power law.

Chapter 8

Detecting Oscillations of SN Neutrinos

By now, neutrino oscillations are firmly established and the next goal is to pin down the oscillation parameters that are still unknown, like the neutrino mass hierarchy and the small mixing angle θ_{13}. Taking our findings on neutrino spectra into account requires new methods for extracting information, but enables us to use ratios of observables instead of their absolute magnitude.

We present a method for identifying the effect of earth-matter oscillations in a detected SN neutrino signal by comparing the time dependence of the energy deposited in two detectors. By identifying spectral modulations with a Fourier-transform method the detection at a single detector is possible, but demands better energy resolution than the two-detector method. Finding oscillation signatures in the signal can pin down the mass hierarchy or restrict the small mixing angle.

Parts of this chapter were published in a similar form in our publications A. S. Dighe, M. T. Keil, and G. G. Raffelt,
"Detecting the neutrino mass hierarchy with a supernova at IceCube," JCAP, in press (2003), hep-ph/0303210, and "Identifying earth matter effects on supernova neutrinos at a single detector," hep-ph/0304150.

8.1 Oscillations of SN Neutrinos

More and more accurate measurements have firmly established neutrino oscillations. After many years of atmospheric- and solar-neutrino experiments and also long-baseline experiments (KamLAND and K2K) we have a good understanding of how neutrinos oscillate (Bahcall, Gonzales-Garcia, & Peña-Garay 2003, Fogli et al. 2002, Gonzales-Garcia & Nir 2002, de Holanda &

Smirnov 2003). The flavors ν_e, ν_μ, and ν_τ are in weak interaction eigenstates and therefore relevant when we talk about interactions of particles. Each of these weak eigenstates is a non-trivial superposition of three mass eigenstates ν_1, ν_2, and ν_3,

$$\begin{pmatrix} \nu_e \\ \nu_\mu \\ \nu_\tau \end{pmatrix} = U \begin{pmatrix} \nu_1 \\ \nu_2 \\ \nu_3 \end{pmatrix} , \tag{8.1}$$

where U is the leptonic mixing matrix that can be written in the canonical form

$$U = \begin{pmatrix} 1 & 0 & 0 \\ 0 & c_{23} & s_{23} \\ 0 & -s_{23} & c_{23} \end{pmatrix} \begin{pmatrix} c_{13} & 0 & e^{i\delta} s_{13} \\ 0 & 1 & 0 \\ -e^{-i\delta} s_{13} & 0 & c_{13} \end{pmatrix} \begin{pmatrix} c_{12} & s_{12} & 0 \\ -s_{12} & c_{12} & 0 \\ 0 & 0 & 1 \end{pmatrix} . \tag{8.2}$$

Here $c_{12} = \cos\theta_{12}$ and $s_{12} = \sin\theta_{12}$ etc., and δ is a phase that can lead to CP-violating effects, that are, however, irrelevant for SN neutrinos. The three matrices then just correspond to the rotation matrices in the 2-3, 1-3, and 1-2 planes, respectively.

The mass eigenstates are most convenient for describing neutrino propagation in space. If there are three different mass eigenstates there can be three different masses. The oscillation, i.e., the interference of the three eigenstates, depends on the difference of the squares of their masses. Usually, the mass-squared differences are given as $\Delta m^2_{ij} \equiv m^2_i - m^2_j$. Of course, only two of them are independent. Compared to the current limit on the absolute neutrino mass, experiments find very small mass-squared differences. Two of the three masses appear to be rather degenerate. The third mass eigenstate can then lie far above or far below this doublet. Whether the third mass eigenstate lies above or below the almost degenerate doublet is referred to as normal or inverted hierarchy, respectively. Which hierarchy is realized in nature is an open question.

The mass squared differences relevant for the atmospheric and solar neutrino oscillations show the strong hierarchy $\Delta m^2_{\rm atm} \gg \Delta m^2_\odot$. This hierarchy, combined with the observed smallness of the angle θ_{13} at CHOOZ (Apollonio et al. 1999) implies that the atmospheric neutrino oscillations essentially decouple from the solar ones and each of these is dominated by only one of the mixing angles. The atmospheric neutrino oscillations are controlled by θ_{23} that may well be maximal (45°). The solar case is dominated by θ_{12}, that is large but not maximal. To a reasonably good accuracy $\Delta m^2_{\rm atm} \approx \Delta m^2_{32}$ and $\Delta m^2_\odot \approx \Delta m^2_{21}$ and therefore $\Delta m^2_{31} \approx \Delta m^2_{32}$. From a global 3-flavor analysis of all data one finds the 3σ ranges for the mass differences and mixing angles summarized in Table 8.1.

Obviously, in the context of SNe neutrino oscillations can only be found if flavor-dependent differences in the SN neutrino fluxes and spectra are present. We denote the fluxes of $\bar{\nu}_{\rm e}$ and $\bar{\nu}_{\mu}$ at earth that would be observable in the absence of oscillations by $F^0_{\bar{\rm e}}$ and $F^0_{\bar{\mu}}$, respectively. In the presence of oscillations a $\bar{\nu}_{\rm e}$ detector actually observes

$$F^D_{\bar{\rm e}}(\epsilon) = \bar{p}^D(\epsilon) F^0_{\bar{\rm e}}(\epsilon) + \left[1 - \bar{p}^D(\epsilon)\right] F^0_{\bar{\mu}}\,, \tag{8.3}$$

where $\bar{p}^D(\epsilon)$ is the $\bar{\nu}_{\rm e}$ survival probability after propagation through the SN mantle and perhaps part of the earth before reaching the detector. Water Cherenkov detectors as well as scintillation detectors can only detect $\bar{\nu}_{\rm e}$ with a good efficiency. Therefore we give the $\bar{\nu}_{\rm e}$ flux at the detector.

When neutrinos travel in matter their oscillatory behavior can change significantly. Depending on the neutrino source the path towards a detector leads through matter surrounding the source, like in stars or in a SN and might also go through the earth. This matter has a significant population of electrons, but other leptons are absent. By charged-current interactions the medium distinguishes between electron flavor and other flavors, which implies a potential for electron neutrinos and anti-neutrinos. In other words, the medium can change its refractive index for electron (anti-)neutrinos. Since the other flavors are unaffected, the oscillatory behavior can change significantly, depending on the electron density.

A significant modification of the survival probability due to the propagation through the earth appears only for those combinations of neutrino mixing parameters shown in Table 8.2. The earth matter effect depends strongly on two parameters, the sign of Δm^2_{32} and the value of $|\theta_{13}|$ (Dighe & Smirnov

Table 8.1. Neutrino mixing parameters

Observation	Mixing angle	Δm^2 [meV^2]
Sun, KamLAND	$\theta_{12} = 27°$–$42°$	$\Delta m^2_{21} = 55$–190
Atmosphere, K2K	$\theta_{23} = 32°$–$60°$	$\lvert\Delta m^2_{32}\rvert = 1400$–$6000$
CHOOZ	$\theta_{13} < 14°$	$\Delta m^2_{31} \approx \Delta m^2_{32}$

Note. — Neutrino mixing parameters from a global analysis of all experiments (3σ ranges) by Gonzalez-Garcia & Nir (2002).

2000, Dighe 2001). The normal hierarchy corresponds to $m_1 < m_2 < m_3$, i.e., $\Delta m^2_{32} > 0$, whereas the inverted hierarchy corresponds to $m_3 < m_1 < m_2$, i.e., $\Delta m^2_{32} < 0$. Note that the presence or absence of the earth effect discriminates between values of $\sin^2\theta_{13}$ less or greater than 10^{-3}, i.e., θ_{13} less or larger than about 1.8°. Thus, the earth effect is sensitive to values of θ_{13} that are much smaller than the current limit (Table 8.1).

Let us consider those scenarios where the mass hierarchy and the value of θ_{13} are such that the earth effect appears for $\bar{\nu}_{\rm e}$. In such cases the $\bar{\nu}_{\rm e}$ survival probability $\bar{p}^D(E)$ is given by

$$\begin{aligned} \bar{p}^D &\approx \cos^2\theta_{12} - \sin 2\bar{\theta}^{\oplus}_{\rm e2}\ \sin(2\bar{\theta}^{\oplus}_{\rm e2} - 2\theta_{12}) \\ &\times \sin^2\left(\frac{\overline{\Delta m^2_{\oplus}}}{10^{-5}\,{\rm eV}^2}\,\frac{L}{1000\,{\rm km}}\,\frac{12.5\,{\rm MeV}}{\epsilon}\right), \end{aligned} \tag{8.4}$$

where the energy dependence of all quantities will always be implicit. Here $\bar{\theta}^{\oplus}_{\rm e2}$ is the mixing angle between $\bar{\nu}_{\rm e}$ and $\bar{\nu}_2$ in earth matter while $\overline{\Delta m^2_{\oplus}}$ is the mass squared difference between the two anti-neutrino mass eigenstates $\bar{\nu}_1$ and $\bar{\nu}_2$, L is the distance traveled through the earth, and ϵ is the neutrino energy. We have assumed a constant matter density inside the earth, which is a good approximation for $L < 10,500$ km, i.e., as long as the neutrinos do not pass through the core of the earth.

Table 8.2. The earth effect in a SN signal.

13-Mixing	Normal Hierarchy	Inverted Hierarchy
$\sin^2\theta_{13} \lesssim 10^{-3}$	$\nu_{\rm e}$ and $\bar{\nu}_{\rm e}$	$\nu_{\rm e}$ and $\bar{\nu}_{\rm e}$
$\sin^2\theta_{13} \gtrsim 10^{-3}$	$\bar{\nu}_{\rm e}$	$\nu_{\rm e}$

Note. — The earth effect appears for the indicated flavors in a SN signal.

8.2 Detecting Oscillations With Two Distant Detectors

8.2.1 The Basic Principle

How significant the oscillation signal in a detected SN neutrino spectrum is, basically depends on the difference between the $\bar{\nu}_e$ and $\bar{\nu}_\mu$ fluxes and the distance traveled through the earth. There is no exact prediction for the spectra emitted by a SN, but some features are established. The mean energies of $\bar{\nu}_e$ and $\bar{\nu}_\mu$ will be very similar, a difference of typically 0–20% should be expected. At the same time the number fluxes will be rather different by up to a factor 2 in any direction. The ratio of fluxes will certainly change with time, because there are two distinct phases responsible for the neutrino signal, namely the accretion phase and Kelvin-Helmholtz cooling of the proto-neutron star (Chapter 2).

With the time dependence of the flux difference it is possible to find an oscillation signature without a detailed knowledge of the original SN signal. Oscillations inside the earth depend on the flux difference and will therefore also change with time. Comparing the time dependence of a neutrino signal of two detectors yields a good chance for detecting the earth effect. The setup should be as follows: one detector sees the SN from above, i.e., without earth effect, and another detector that neutrinos reach after traveling through the earth. The chance for encountering this setup increases with the separation of the detectors. Detectors that are separated by a long distance and will be operational for many decades are the future IceCube detector in Antarctica (Ahrens et al. 2002b) and, for example, the Super-Kamiokande detector in Japan.

8.2.2 The SN Signal at IceCube

It has been recognized for a long time that neutrino telescopes detecting Cherenkov light in ice can detect a SN neutrino burst because the Cherenkov glow of the ice can be identified as time-correlated noise among all phototubes (Halzen, Jacobsen, & Zas 1994, 1996). This approach has been used by the neutrino telescope AMANDA to exclude the occurrence of a galactic SN over a recent observation period (Ahrens et al. 2002a).

The SN neutrinos streaming through the antarctic ice interact according to $\bar{\nu}_e p \rightarrow n e^+$ and some other less important reactions. The positrons, in turn, emit Cherenkov light producing a homogeneous and isotropic glow of the ice. The optical modules (OMs) that are frozen into the ice are immersed in this diffuse bath of photons and pick up a number corresponding to their

angular acceptance and quantum efficiency. Estimating the event rate of a SN signal induced by the $\bar{\nu}_{\rm e}{\rm p} \rightarrow {\rm ne}^+$ reaction yields (Dighe et al. 2003a)

$$\Gamma_{\rm events} = 62\ {\rm s}^{-1}\ \frac{L_{\bar{\nu}_{\rm e}}}{10^{52}\ {\rm erg\ s}^{-1}}\ \left(\frac{10\ {\rm kpc}}{D}\right)^2\ f_{\rm flux}\, f_{\rm det}\ , \tag{8.5}$$

where $L_{\bar{\nu}_{\rm e}}$ is the $\bar{\nu}_{\rm e}$ luminosity after flavor oscillations, and D the distance between SN and detector. The factors $f_{\rm flux}$ and $f_{\rm det}$ parameterize the flux and detector characteristics, respectively. Both factors are of order 1. For the flux we have

$$\begin{aligned} f_{\rm flux} &= \frac{15\ {\rm MeV}}{\langle\epsilon_{\bar{\nu}_{\rm e}}\rangle}\ \frac{8}{15}\ \frac{\langle\epsilon^3_{\bar{\nu}_{\rm e}}\rangle}{(15\ {\rm MeV})^3} \\ &= \frac{(3+\alpha)(2+\alpha)}{(1+\alpha)^2}\ \frac{8}{15}\ \frac{\langle\epsilon_{\bar{\nu}_{\rm e}}\rangle^2}{(15\ {\rm MeV})^2}\ , \end{aligned} \tag{8.6}$$

where we used Equation (5.13) in the last line, i.e., we applied our α parameterization. For $\alpha = 3$ and $\langle\epsilon_{\bar{\nu}_{\rm e}}\rangle = 15$ MeV the factor is 1.

The factor $f_{\rm det}$ contains the efficiency for converting the neutrino signal into photons by the ice as well as the efficiency for detecting these photons. For our purpose we assume $f_{\rm det} = 1$.

In the 4800 OMs of IceCube a SN in our galaxy would yield a total event number of about 1.5×10^6 photons if we assume the SN radiates 5×10^{52} erg. This rate needs to be compared to the background counting rate of 300 Hz per OM and thus for a duration of 10 s we expect 1.44×10^7 photons in total. Assuming Poisson fluctuations, the uncertainty of this number is 3.8×10^3, i.e., 0.1% of the SN signal. Therefore, one can determine the SN signal with a statistical sub-percent precision, ignoring for now problems of absolute detector calibration.

In order to illustrate the statistical power of IceCube to observe a SN signal we use two different numerical SN simulations. The first was performed by the Livermore group (Totani et al. 1998) that involves traditional input physics for ν_μ interactions and a flux-limited diffusion scheme for treating neutrino transport. The great advantage of this simulation is that it covers the full evolution from infall over the explosion to the Kelvin-Helmholtz cooling phase of the proto-neutron star. We show the Livermore $\bar{\nu}_{\rm e}$ and $\bar{\nu}_\mu$ lightcurves in Figure 8.1 (left panels). For all flavors these curves are also displayed in Figure 2.4.

Our second simulation was performed with the Garching code (Rampp & Janka 2002). It includes all relevant neutrino interaction rates, including nucleon bremsstrahlung, neutrino pair processes, weak magnetism, nucleon recoils, and nuclear correlation effects. The neutrino transport part is based

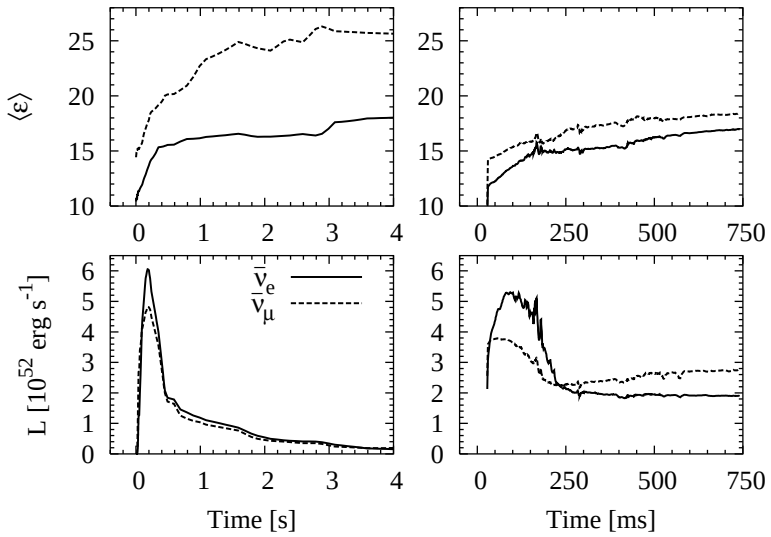

Fig. 8.1.— Supernova $\bar{\nu}_e$ and $\bar{\nu}_\mu$ light curves and average energies. *Left:* Livermore simulation (Totani et al.1999). *Right:* Garching simulation (Raffelt et al. 2003).

on a Boltzmann solver. The neutrino-radiation hydrodynamics program allows one to perform spherically symmetric as well as multi-dimensional simulations. The progenitor model is a $15\,M_\odot$ star with a $1.28\,M_\odot$ iron core. The period from shock formation to 468 ms after bounce was evolved in two dimensions. The subsequent evolution of the model is simulated in spherical symmetry. At 150 ms the explosion sets in, although a small modification of the Boltzmann transport was necessary to allow this to happen (Janka et al. 2003). Recall that unmanipulated full-scale models with an accurate treatment of the microphysics currently do not obtain explosions (Section 2.4). This run will be continued beyond the current epoch of 750 ms post bounce; we here use the preliminary results currently available (Raffelt et al. 2003). We show the Garching $\bar{\nu}_e$ and $\bar{\nu}_\mu$ lightcurves in Figure 8.1 (right panels).

We take the Livermore simulation to represent traditional predictions for flavor-dependent SN neutrino fluxes and spectra that were used in many previous discussions of SN neutrino oscillations. The Garching simulation is taken to represent a situation when the $\bar{\nu}_\mu$ interactions are more systematically included so that the flavor-dependent spectra and fluxes are more similar than had been assumed previously. We think it is useful to juxtapose the IceCube response for both cases.

Another difference is that in Livermore the accretion phase lasts longer. Since the explosion mechanism is not finally settled, it is not obvious which

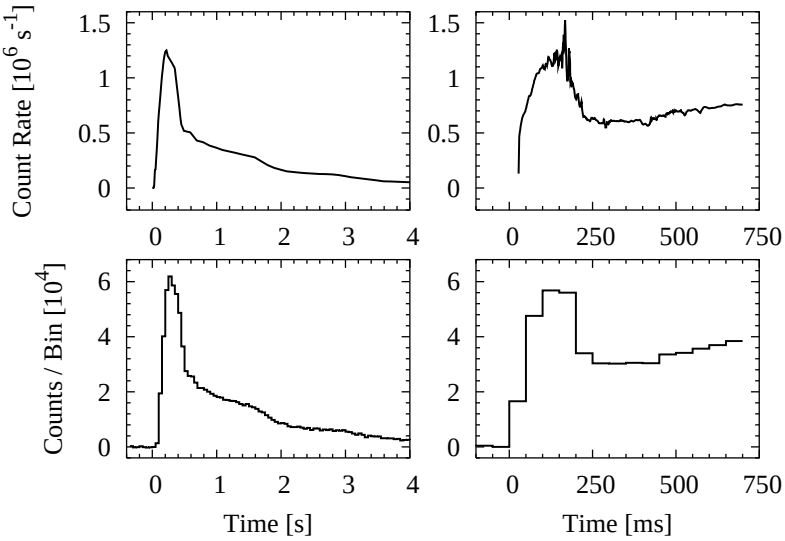

Fig. 8.2.— Supernova signal in IceCube assuming a distance of 10 kpc, based on the Livermore simulation (left) and the Garching one (right), in both cases ignoring flavor oscillations. In the bottom panels we have used 50 ms bins and have added noise from a background rate of 300 Hz per OM.

case is more realistic. Moreover, there could be differences between different SNe. The overall features are certainly comparable between the two simulations.

In Figure 8.2 we show the expected counting rates in IceCube as given in Equation (8.5) for an assumed distance of 10 kpc and 4800 OMs for the Livermore (left) and Garching (right) simulations. We also show this signal in 50 ms bins where we have added noise from a background of 300 Hz per OM. The baseline is at the average background rate so that negative counts correspond to downward background fluctuations.

One could easily identify the existence and duration of the accretion phase and thus test the standard delayed-explosion scenario. One could also measure the overall duration of the cooling phase and thus exclude the presence of significant exotic energy losses. Therefore, many of the particle-physics limits based on the SN 1987A neutrinos (Raffelt 1999) could be supported with a statistically serious signal. If the SN core were to collapse to a black hole after some time, the sudden turn-off of the neutrino flux could be identified. In short, when a galactic SN occurs, IceCube is a powerful stand-alone neutrino detector, providing us with a plethora of information that is of fundamental astrophysical and particle-physics interest.

8.2.3 The Oscillation Signal at Ice Cube

In order to calculate the extent of the earth effect for IceCube, we will assume that the relevant mixing parameters are $\Delta m^2_{12} = 6 \times 10^{-5}$ eV^2 and $\sin^2(2\theta_{12}) = 0.9$. We further assume that the source spectra are given by the functional form of our α fit Equation (5.9). The values of the parameters α and $\langle\epsilon\rangle$ for both the $\bar{\nu}_e$ and $\bar{\nu}_\mu$ spectra are in general time dependent.

In Figure 8.3 we show the variation of the expected IceCube signal with earth-crossing length L for the two sets of parameters detailed in Table 8.3. The first could be representative of the accretion phase, the second of the cooling signal. We use the two-density approximation for the earth density profile, where the core has a density of 11.5 g cm^{-3} and a radius of 3,500 km, while the density of the earth mantle was taken to be 4.5 g cm^{-3}. We observe that for short distances, corresponding to near-horizontal neutrino trajectories, the signal varies strongly with L. Between about 3,000 and 10,500 km it reaches an asymptotic value that we call the "asymptotic mantle value." For Case (a), this value corresponds to about 1.5% depletion of the signal, whereas for (b) it corresponds to about 6.5% depletion.

Beyond an earth-crossing length of about 10,500 km, the neutrinos have to cross the earth core with another large jump in density. The core ef-

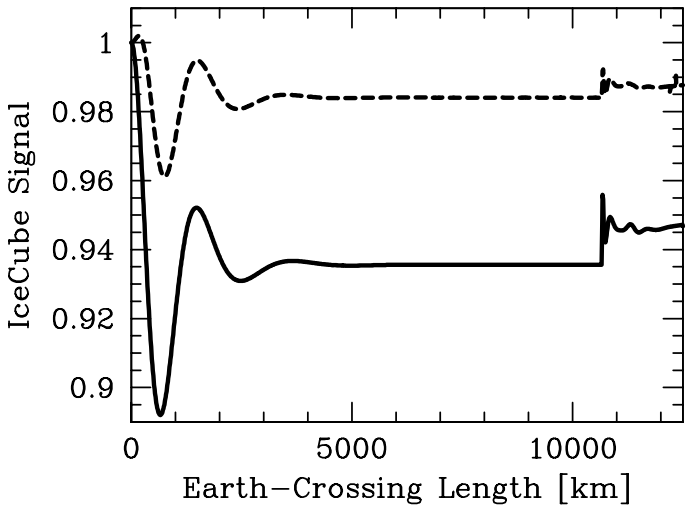

Fig. 8.3.— Variation of the expected IceCube signal with neutrino earth crossing length L for the assumed flux and mixing parameters of Table 8.3. The signal is normalized to 1 when no earth effect is present, i.e. for $L = 0$. The dashed line is for the case representing the accretion phase, the solid line for the cooling phase.

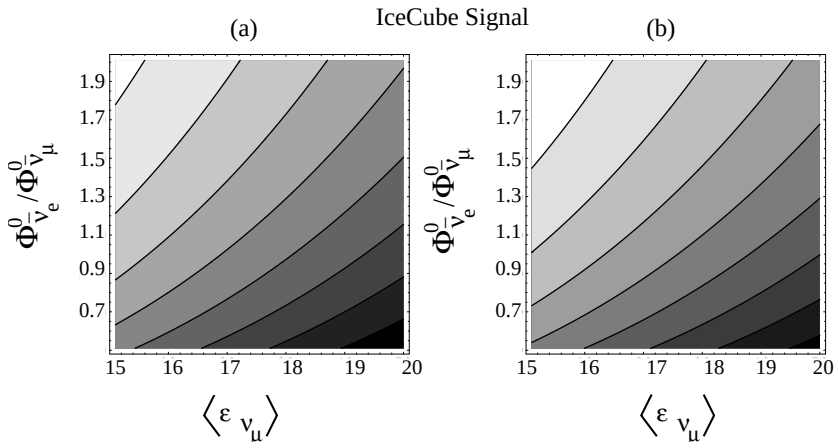

Fig. 8.4.— Asymptotic IceCube signal modification by the earth effect. The fixed flux parameters are (a) $\langle\epsilon_{\bar{\nu}_e}\rangle = 15$ MeV, $\alpha_{\bar{\nu}_e} = 4.0$, and $\alpha_{\bar{\nu}_\mu} = 3.0$ and (b) $\langle\epsilon_{\bar{\nu}_e}\rangle = 15$ MeV, $\alpha_{\bar{\nu}_e} = \alpha_{\bar{\nu}_\mu} = 3.0$. The contours are equally spaced starting from 1.02 (light) in 0.02 decrements to smaller values (darker).

fects change the asymptotic mantle value by roughly 1% as can be seen in Figure 8.3. We neglect the core effects in the following analysis, and the "asymptotic value" always refers to the asymptotic mantle value.

For the largest part of the sky the earth effect either appears with this asymptotic value ("neutrinos coming from below"), or it does not appear at all ("neutrinos from above"). Therefore, we now focus on the asymptotic value and study how the signal modification depends on the assumed flux parameters. In Table 8.4 we show the signal modification for $\langle\epsilon_{\bar{\nu}_e}\rangle = 15$ MeV, $\alpha_{\bar{\nu}_e} = 4.0$, and $\alpha_{\bar{\nu}_\mu} = 3.0$ as a function of $\langle\epsilon_{\bar{\nu}_\mu}\rangle$ and the flux ratio $\Phi^0_{\bar{\nu}_e}/\Phi^0_{\bar{\nu}_\mu}$. In Table 8.5 we show the same with $\alpha_{\bar{\nu}_e} = \alpha_{\bar{\nu}_\mu} = 3.0$. The results are shown in the form of contour plots in Figure 8.4.

Even for mildly different fluxes or spectra the signal modification is several

Table 8.3. Flux parameters for two representative cases.

Example	Phase	$\langle\epsilon_{\bar{\nu}_e}\rangle$ [MeV]	$\langle\epsilon_{\bar{\nu}_\mu}\rangle$ [MeV]	$\alpha_{\bar{\nu}_e}$	$\alpha_{\bar{\nu}_\mu}$	$\Phi^0_{\bar{\nu}_e}/\Phi^0_{\bar{\nu}_\mu}$	Asymptotic Earth Effect
(a)	Accretion	15	17	4	3	1.5	−1.5%
(b)	Cooling	15	18	3	3	0.8	−6.5%

Table 8.4. Asymptotic IceCube signal modification by the earth effect

Flux ratio	$\langle \epsilon_{\bar{\nu}_\mu} \rangle$ [MeV]					
$\Phi^0_{\bar{\nu}_e}/\Phi^0_{\bar{\nu}_\mu}$	15	16	17	18	19	20
2.0	1.026	1.014	1.002	0.988	0.974	0.960
1.9	1.023	1.011	0.999	0.985	0.971	0.956
1.8	1.021	1.009	0.995	0.982	0.967	0.952
1.7	1.018	1.005	0.992	0.978	0.963	0.948
1.6	1.015	1.002	0.988	0.974	0.959	0.944
1.5	1.012	0.998	0.984	0.969	0.954	0.939
1.4	1.008	0.994	0.980	0.965	0.949	0.934
1.3	1.004	0.990	0.975	0.960	0.944	0.928
1.2	1.000	0.985	0.970	0.954	0.938	0.922
1.1	0.995	0.980	0.964	0.948	0.932	0.915
1.0	0.989	0.974	0.957	0.941	0.925	0.908
0.9	0.983	0.967	0.950	0.934	0.917	0.901
0.8	0.976	0.959	0.942	0.925	0.909	0.892
0.7	0.967	0.950	0.933	0.916	0.899	0.883
0.6	0.958	0.940	0.923	0.906	0.889	0.873
0.5	0.946	0.928	0.911	0.894	0.877	0.862

Note. — The fixed flux parameters are $\langle \epsilon_{\bar{\nu}_e} \rangle = 15$ MeV, $\alpha_{\bar{\nu}_e} = 4.0$, and $\alpha_{\bar{\nu}_\mu} = 3.0$.

Table 8.5. Same as Table 8.4 with $\alpha_{\bar{\nu}_e} = \alpha_{\bar{\nu}_\mu} = 3.0$.

Flux ratio	$\langle \epsilon_{\bar{\nu}_\mu} \rangle$ [MeV]					
$\Phi^0_{\bar{\nu}_e}/\Phi^0_{\bar{\nu}_\mu}$	15	16	17	18	19	20
2.0	1.036	1.024	1.012	1.000	0.986	0.972
1.9	1.033	1.022	1.010	0.996	0.983	0.968
1.8	1.031	1.019	1.006	0.993	0.979	0.964
1.7	1.028	1.016	1.003	0.989	0.975	0.960
1.6	1.025	1.013	0.999	0.985	0.971	0.955
1.5	1.022	1.009	0.995	0.981	0.966	0.951
1.4	1.019	1.005	0.991	0.976	0.961	0.945
1.3	1.015	1.001	0.986	0.971	0.955	0.940
1.2	1.010	0.996	0.981	0.965	0.949	0.933
1.1	1.006	0.991	0.975	0.959	0.943	0.927
1.0	1.000	0.985	0.969	0.952	0.936	0.919
0.9	0.994	0.978	0.961	0.945	0.928	0.911
0.8	0.986	0.970	0.953	0.936	0.919	0.903
0.7	0.978	0.961	0.944	0.926	0.910	0.893
0.6	0.968	0.950	0.933	0.916	0.899	0.882
0.5	0.956	0.938	0.920	0.903	0.886	0.870

percent, by far exceeding the statistical uncertainty of the IceCube signal, although the absolute calibration of IceCube may remain uncertain to within several percent. However, the signal modification will vary with time during the SN burst. During the early accretion phase that is expected to last for a few 100 ms and corresponds to a significant fraction of the overall signal, the $\bar{\nu}_\mu$ flux may be almost a factor of 2 smaller than the $\bar{\nu}_\mathrm{e}$ flux, but it will be slightly hotter and less pinched (Raffelt et al. 2003). This corresponds to Case (a) of Table 8.3; it is evident from Figure 8.3 and Table 8.4 that this implies that the earth effect is very small. During the Kelvin-Helmholtz cooling phase the flux ratio is reversed with more $\bar{\nu}_\mu$ being emitted than $\bar{\nu}_\mathrm{e}$, but still with the same hierarchy of energies. This corresponds to Case (b); in this case the earth effect could be about 6%. This time dependence may allow one to detect the earth effect without a precise absolute detector calibration.

In order to illustrate the time dependence of the earth effect we show in Figure 8.5 the expected counting rate in IceCube for both the Livermore (left panels) and Garching (right panels) simulations. In the upper panels we show the expected counting rate with flavor oscillations in the SN mantle, but no earth effect (solid lines), or with the asymptotic earth effect (dashed lines) that obtains for a large earth-crossing path. Naturally the differences are very small so that we show in the lower panels the ratio of these curves, i.e., the expected counting rate with/without earth effect as a function of time for both Livermore and Garching. While for the Livermore simulation there is a large earth effect even at early times, the change from early to late times in both cases is around 4–5%. Therefore, the most model-independent signature is a time variation of the earth effect during the SN neutrino signal.

In order to demonstrate the statistical significance of these effects we integrate the expected signal for both simulations separately for the accretion phase and the subsequent cooling phase; the results are shown in Table 8.6. For both simulations the earth effect itself and its change with time is statistically highly significant. Due to more schematic input physics the Livermore model overestimates the differences between $\bar{\nu}_\mathrm{e}$ and $\bar{\nu}_\mu$ spectra. However, the relative change of the earth effect during accretion and cooling is not vastly different between the two simulations. Recalling that the absolute detector calibration may be very uncertain so that one has to rely on the temporal variation of the earth effect, the difference between Livermore and Garching becomes much smaller. We expect that it is quite generic that the temporal change of the earth effect is a few percent of the overall counting rate.

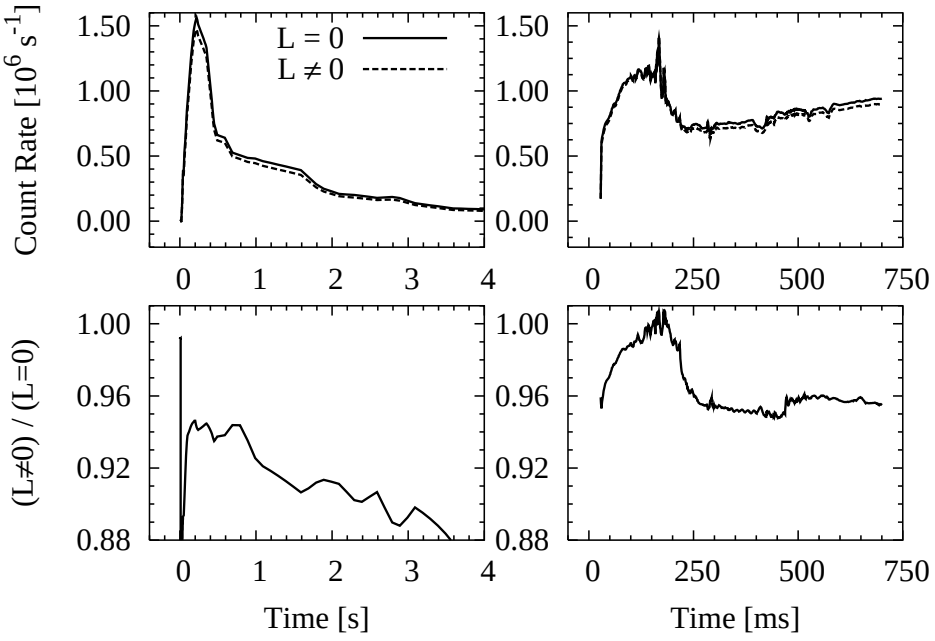

Fig. 8.5.— Earth effect in IceCube. The upper panels show the expected counting rate based on the Livermore (left) and Garching (right) models, including flavor oscillations. The solid line is without earth effect ($L = 0$), the dashed line with asymptotic earth effect ($L \neq 0$). The lower panels show the ratio between these curves, i.e., the ratio of counting rates with/without earth effect.

Table 8.6. IceCube Cherenkov counts for the numerical SN models.

	Livermore		Garching	
	Accretion	Cooling	Accretion	Cooling
Integration time [s]	0–0.500	0.500–3	0–0.250	0.250–0.700
SN Signal [Counts]				
No Earth Effect	519,080	818,043	173,085	407,715
Asymptotic Earth Effect	488,093	751,137	171,310	390,252
Difference	30,987	66,906	1,775	17,463
Fractional Difference	−5.97%	−8.18%	−1.03%	−4.28%
Background [Counts]	720,000	4,320,000	360,000	648,000
$\sqrt{\text{Background}}$/Signal	0.16%	0.25%	0.35%	0.20%

8.2.4 Super- or Hyper-Kamiokande and IceCube

One can measure the earth effect in IceCube only in conjunction with another high-statistics detector. We do not attempt to simulate in detail the SN signal in this other detector but simply assume that it can be measured with a precision about as good as in IceCube. One candidate is Super-Kamiokande, a water Cherenkov detector that would measure around 10^4 events from a galactic SN at a distance of 10 kpc. Therefore, the statistical precision for the total neutrino energy deposition in the water is around 1% and thus worse than in IceCube. Even though Super-Kamiokande will measure a larger number of Cherenkov photons than IceCube, a single neutrino event will cause an entire Cherenkov ring to be measured, i.e., the photons are highly correlated. Therefore, in the estimated statistical $\sqrt{N}$ fluctuation of the signal, the fluctuating number N is that of the detected neutrinos. If the future Hyper-Kamiokande is built, its fiducial volume would be about 30 times that of Super-Kamiokande. In this case the statistical signal precision exceeds that of IceCube for the equivalent observable.

We denote the equivalent IceCube signal measured by Super- or Hyper-Kamiokande as $N_{\rm SK}$ and the IceCube signal as $N_{\rm IC}$. If the distances traveled by the neutrinos before reaching these two detectors are different, the earth effect on the neutrino spectra may be different, which will reflect in the ratio $N_{\rm SK}/N_{\rm IC}$. Of course, in the absence of the earth effect this ratio equals unity by definition.

The geographical position of IceCube with respect to Super- or Hyper-Kamiokande at a northern latitude of 36.4° is well-suited for the detection of the earth effect through a combination of the signals. Using Figure 8.3 we can already draw some qualitative conclusions about the ratio $N_{\rm SK}/N_{\rm IC}$. Clearly, $N_{\rm SK}/N_{\rm IC} = 1$ if neutrinos do not travel through the earth before reaching either detector. If the distance traveled by neutrinos through the earth is more that 3,000 km for both detectors, the earth effects on both $N_{\rm SK}$ and $N_{\rm IC}$ are nearly equal and their ratio stays around unity. If the neutrinos come "from above" for SK and "from below" for IceCube, or vice versa, the earth matter effect will shift this ratio from unity.

In Figure 8.6, we show contours of $N_{\rm SK}/N_{\rm IC}$ for the SN position in terms of the location on earth where the SN is at the zenith. The map is an area preserving Hammer-Aitoff projection so that the sizes of different regions in the figure gives a realistic idea of the "good" and "bad" regions of the sky. In order to generate the contours we use the parameters of Case (b) in Table 8.3 so that the asymptotic suppression of the signal is about 6.5%. The sky falls into four distinct regions depending on the direction of the neutrinos relative to either detector as described in Table 8.7. When the neutrinos come from

above for both detectors (Region D) there is no earth effect. If they come from below in both (Region C), the earth effect is large in both. Depending on the exact distance traveled through the earth, the event ratio can be large, but generally fluctuates around 1. In the other regions where the neutrinos come from above for one detector and from below for the other (Regions A and B) the relative effect is large.

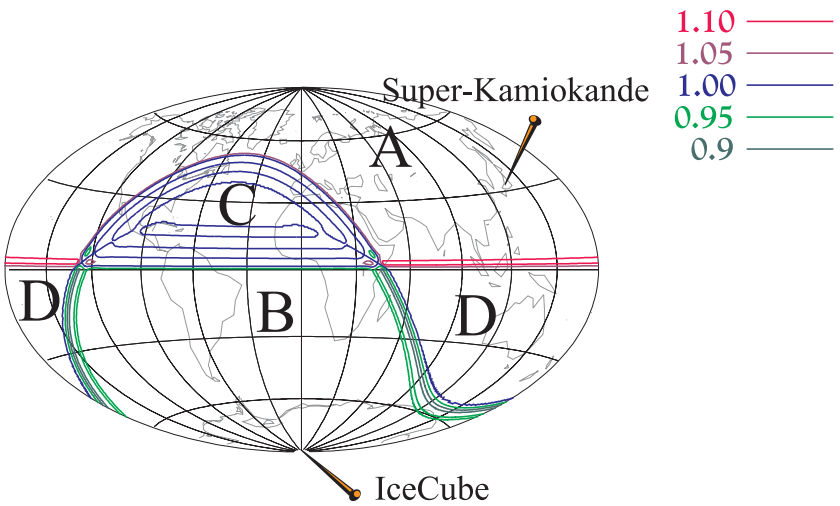

Fig. 8.6.— Contours of $N_{\rm SK}/N_{\rm IC}$ on the map of the sky projected on the earth. The regions A, B, C, D are described in Table 8.7.

Table 8.7. Regions in Figure 8.6 for the earth effect in IceCube and Super-Kamiokande.

Region	Sky fraction	Neutrinos come from		$N_{\rm SK}/N_{\rm IC}$
		IceCube	Super-K	
A	0.35	below	above	1.070
B	0.35	above	below	0.935
C	0.15	below	below	Fluctuations around 1
D	0.15	above	above	1

8.3 Detecting the Earth-Matter Effect at a Single Detector

According to Equation (8.4) the modulations imprinted on the detected spectra are proportional to $\sin^2(\#/\epsilon)$. Therefore the prefactor # should appear as a dominant frequency in the Fourier transform of the inverse energy spectrum (Dighe et al. 2003b), because in inverse-energy space the modulations of the SN neutrino spectrum are nearly equispaced.

The equidistant peaks in the modulation of the inverse-energy spectrum are a necessary feature of the earth effects. Indeed, the net $\bar{\nu}_e$ flux at the detector may be written using (8.3) and (8.4) in the form

$$F_{\bar{e}}^D = \sin^2\theta_{12}F_{\bar{\mu}}^0 + \cos^2\theta_{12}F_{\bar{e}}^0 + \Delta F^0\bar{A}_\oplus \sin^2(\overline{\Delta m^2_\oplus}L/\epsilon) \quad , \tag{8.7}$$

where $\Delta F^0 \equiv (F_{\bar{e}}^0 - F_{\bar{\mu}}^0)$ depends only on the primary neutrino spectra, whereas $\bar{A}_\oplus \equiv -\sin 2\bar{\theta}^\oplus_{e2}\ \sin(2\bar{\theta}^\oplus_{e2} - 2\theta_{12})$ depends only on the mixing parameters and is independent of the primary spectra. The last term in (8.7) is the earth oscillation term that contains a frequency $k_\oplus \equiv 2\overline{\Delta m^2_\oplus}L$ in ϵ^{-1}, with the coefficient $\Delta F^0\bar{A}_\oplus$ being a comparatively slowly varying function of ϵ^{-1}. The first two terms in (8.7) are also slowly varying functions of ϵ^{-1}, and hence contain frequencies in ϵ^{-1} that are much smaller than $k_\oplus$.

The frequency $k_\oplus$ is completely independent of the primary neutrino spectra, and indeed can be determined to a good accuracy from the knowledge of the solar oscillation parameters, the earth matter density, and the direction of the SN. If this frequency component is isolated from the inverse-energy spectrum of $\bar{\nu}_e$, the earth effects would be identified.

Due to the energy dependence of the prefactors of the oscillation term $\Delta F^0\bar{A}_\oplus$ and of $\Delta m^2_\oplus$ in Equation (8.7) the peak in the Fourier-transformed spectrum gets a certain width around $k_\oplus$. This peak can be clearly identified if the earth effect is present.

In an experiment there are two effects obscuring the signal. One is the statistical fluctuations of the signal and the other is the smearing of the modulation signal by the energy resolution of the detector. Higher statistics as well as better energy resolution enhance the oscillation signature. A prescription for identifying the prominent peak on top of the background can be found in Dighe et al. (2003b). If the direction of the SN is known we can estimate $k_\oplus$ and by that simplify the peak identification.

Once the peak is identified this is a clear signal of earth-matter effects. As stated in Section 8.2.4 an identification of the earth-matter effect will severely restrict the neutrino mixing parameter space, since the effects are present only with the combinations of the neutrino mass hierarchy and the

mixing angle θ_{13} given in Table 8.2. In particular, if $\sin^2\theta_{13}$ is measured at a laboratory experiment to be greater than 10^{-3}, then the earth effects on the $\bar{\nu}_e$ spectrum imply the normal mass hierarchy. However, if the earth effects are not detected, it does not rule out any neutrino mixing parameters, owing to the current uncertainties in the primary fluxes.

With the position of the peak it is even possible to determine $\Delta m^2_\odot$ to an accuracy of a few percent and therefore much better than the current limits, that are $\Delta m^2_\odot = (5.5\text{–}19) \times 10^{-5}$ eV^2. The Fourier-transform method will measure $\Delta m^2_\odot$ to a precision of 10%, comparable to what can be reached by KamLAND (de Gouvea & Peña-Garay, 2001).

8.4 Summary

With our new findings for the SN neutrino spectra methods for identifying oscillation signatures in an observed neutrino spectrum need to be changed. We presented two very promising concepts for detecting the earth-matter effect. For the IceCube detector in Antarctica earth matter-effects are present in the signal of a future galactic SN on the level of a few percent. If the IceCube signal can be compared with another high-statistics signal, notably in Super-Kamiokande or Hyper-Kamiokande, the earth effect becomes clearly visible as a difference between the detectors. As one is looking for a signal modification in the range of a few percent, the absolute detector calibration may not be good enough in one or both of the instruments. However, for typical numerical SN simulations the effect is time dependent and most notably differs between the early accretion phase and the subsequent neutron star cooling phase. Therefore, one would have to search for a temporal variation of the relative detector signals of a few percent. The large number of optical modules in IceCube renders this task statistically possible. In fact depending on the differences in flavor-dependent fluxes, the statistical accuracy of Super-Kamiokande may turn out to be the limiting factor. This limitation is not significant for Hyper-Kamiokande.

The unique location of IceCube in Antarctica implies that for about 70% of the sky this detector sees the SN through the earth when Super- and Hyper-Kamiokande see it from above, or the other way round, i.e., the chances of a relative signal difference between the detectors are large. If both detectors were to see the SN from above or both through the earth, the comparison of the signals would would not reveal the earth effect.

Once future detectors like Hyper-Kamiokande or large scintillation detectors become available a powerful way of identifying earth-matter effects is through the Fourier transform of the inverse-energy spectrum. In the inverse-

energy spectrum modulations due to earth matter will be approximately equispaced and therefore appear as a single peak in the Fourier transformed spectrum. With this method one can unambiguously prove the existence of earth-matter oscillations and even measure $\Delta m^2_\odot$ to a accuracy of a few percent.

Identifying the earth-matter effects in the neutrino signal of a future galactic SN would restrict the parameter space for neutrino oscillations severely. If, in addition, the magnitude of the mixing angle θ_{13} can be established to be large in the sense of $\sin^2\theta_{13} \gtrsim 10^{-3}$ by a long-baseline experiment (Barger et al. 2001, Cervera et al. 2000, Freund et al. 2001), it implies the normal mass hierarchy.

On the other hand, if $\sin^2\theta_{13} \lesssim 10^{-3}$ has been established, the earth effect is unavoidable whatever the hierarchy is. Not observing it for such a small θ_{13} would imply that the primary SN neutrino fluxes and spectra are more similar than indicated by state-of-the-art numerical simulations. For $\sin^2\theta_{13} \gtrsim 10^{-3}$ not observing the earth-matter effects does not allow one to draw conclusions, because it can be due the original SN spectra and fluxes, or due to the neutrino mass hierarchy.

Chapter 9

Discussion and Summary

It has been known for some time that the "traditional" set of ν_μ-matter interactions employed by hydrodynamic SN simulations was incomplete. In addition to the ingredients that were known to be missing, i.e., nucleon bremsstrahlung and nucleon recoil, we showed that $\nu_e\bar{\nu}_e$ annihilation into $\nu_\mu\bar{\nu}_\mu$ is always more important than the traditional e^+e^- annihilation process by a factor of 2–3.

In a systematic approach we studied the formation of neutrino spectra and fluxes in a SN core. Using a Monte Carlo code for neutrino transport, we varied the microscopic input physics as well as the underlying static proto-neutron star atmosphere. We used two background models from self-consistent hydrodynamic simulations, and several power-law models with varying power-law indices for the density and temperature and different constant values for the electron fraction Y_e.

The ν_μ transport opacity is dominated by neutral-current scattering on nucleons. In addition, there are number-changing processes (nucleon bremsstrahlung, leptonic pair annihilation) and energy-changing processes ($\nu_\mu e^\pm$ and $\nu_\mu\nu_e$, $\nu_\mu\bar{\nu}_e$ scattering). Recoil in nucleon scattering allows for a small energy exchange in each collision. The ν_μ spectra and fluxes are roughly accounted for if one includes one significant channel of pair production and one for energy exchange in addition to ν_μN scattering. For example, the traditional set of microphysics (iso-energetic ν_μN scattering, e^+e^- annihilation, and $\nu_\mu e^\pm$ scattering) yields crudely comparable spectra and fluxes to a calculation where pairs are produced by nucleon bremsstrahlung and energy is exchanged by nucleon recoil. The overall result is robust to within 30% against the detailed choice of microphysics.

However, in view of neutrino oscillations, where flavor-dependent flux differences are important, state-of-the-art simulations should aim at a high precision for the fluxes and spectral energies. Therefore, one needs to include

bremsstrahlung, leptonic pair annihilation, neutrino-electron scattering, and energy transfer in neutrino-nucleon collisions. As expected, the traditional e^+e^- annihilation process is always much less important than $\nu_e\bar{\nu}_e$ annihilation. None of the reactions studied here can be neglected except perhaps the traditional e^+e^- annihilation process, and $\nu_\mu\nu_e$ and $\nu_\mu\bar{\nu}_e$ scattering.

The existing treatments of the nuclear-physics aspects of the $NN \to NN\nu\bar{\nu}$ bremsstrahlung process are rather schematic. We find, however, that the ν_μ fluxes and spectra do not depend sensitively on the exact strength of the bremsstrahlung rate. Therefore, while a more adequate treatment of bremsstrahlung remains desirable, the final results are unlikely to be much affected.

The transport of ν_μ and $\bar{\nu}_\mu$ is usually treated identically. However, weak-magnetism effects render the ν_μN and $\bar{\nu}_\mu$N scattering cross sections somewhat different (Horowitz 2002), causing a small ν_μ chemical potential to build up. We find that the differences between the average energies of ν_μ and $\bar{\nu}_\mu$ are only a few percent and can thus be neglected for most purposes.

Including all processes works in the direction of making the fluxes and spectra of ν_μ more similar to those of $\bar{\nu}_e$ compared to a calculation with the traditional set of input physics. During the accretion phase the neutron-star atmosphere is relatively expanded, i.e., the density and temperature gradients are relatively shallow. Our investigation suggests that during this phase $\langle\epsilon_{\nu_\mu}\rangle$ is only slightly larger than $\langle\epsilon_{\bar{\nu}_e}\rangle$, perhaps by a few percent or 10% at most. This result agrees with the first hydrodynamic simulation including all of the relevant microphysics except $\nu_e\bar{\nu}_e$ annihilation (Accretion-Phase Model II) provided to us by M. Rampp. For the luminosities of the different neutrino species one finds $L_{\bar{\nu}_e} \approx L_{\nu_e} \approx 2\,L_{\nu_\mu}$. The smallness of L_{ν_μ} is not surprising because the effective radiating surface is much smaller than for $\bar{\nu}_e$.

During the Kelvin-Helmholtz cooling phase the neutron-star atmosphere will be more compact, the density and temperature gradients will be steeper. Therefore, the radiating surfaces for all species will become more similar. In this situation L_{ν_μ} may well become larger than $L_{\bar{\nu}_e}$. However, the relative luminosities depend sensitively on the electron concentration. Therefore, without a self-consistent hydrostatic late-time model it is difficult to claim this luminosity cross-over with confidence.

The ratio of the spectral energies is most sensitive to the temperature gradient relative to the density gradient. In our power-law models we used $\rho \propto r^{-p}$ and $T \propto r^{-q}$. Varying q/p between 0.25 and 0.35 we find that $\langle\epsilon_{\bar{\nu}_e}\rangle : \langle\epsilon_{\nu_\mu}\rangle$ varies between $1 : 1.10$ and $1 : 1.22$. Noting that the upper range for q/p seems unrealistically large we conclude that even at late times the spectral differences should be small; 20% sounds like a safe upper limit. However, the power-law models might overestimate the spread of mean energies, as can

be inferred from comparing the shallow power-law model with the realistic accretion-phase models. We stress that there is no physical reason for the inequality $\langle\epsilon_{\bar{\nu}_e}\rangle < \langle\epsilon_{\nu_\mu}\rangle$. It may well be that at some point the mean energies are equal or even cross over.

The statements about the relative neutrino energies in the previous literature fall into two classes. One group of workers, using the traditional set of microphysics, found spectral differences between $\bar{\nu}_e$ and ν_μ on the 25% level, a range which largely agrees with our findings in view of the different microphysics. Other papers claim ratios as large as $\langle\epsilon_{\bar{\nu}_e}\rangle : \langle\epsilon_{\nu_\mu}\rangle = 1 : 1.8$ or even exceeding $1 : 2$. We have no explanation for these latter results. At least within the framework of our simple power-law models we do not understand which parameter could be reasonably adjusted to reach such extreme spectral differences.

In a high-statistics neutrino observation of a future galactic SN one may well be able to discover signatures of flavor oscillations. However, when studying these questions one has to allow for the possibility of very small spectral differences, and conversely, for the possibility of large flux differences. This situation is almost orthogonal to what has often been assumed in papers studying possible oscillation signatures. A realistic assessment of the potential of a future galactic SN to disentangle different neutrino mixing scenarios should allow for the possibility of very small spectral differences among the different flavors of anti-neutrinos. The spectral differences between ν_e and $\nu_{\mu,\tau}$ are always much larger, but a large SN neutrino (as opposed to anti-neutrino) detector does not exist.

Previous analyses on oscillation effects in the neutrino flux of a SN not only assumed equipartition of the luminosities and a large hierarchy in mean energies, but also heavily relied on the absolute magnitude of model predictions. Comparing such predictions with results from an observation has little predictive power due to uncertainties in the models, e.g., the nuclear equation of state. Reliable methods involve only relative flux differences and small relative differences in energies. With such rather model independent assumptions one can unambiguously identify oscillation effects.

We proposed a method for identifying earth-matter effects by comparing the SN neutrino signal of two detectors. One detector records the signal from above, the other through the earth. If the energy deposited per unit volume in both detectors differs, the earth-matter effect is detected. Surprisingly, the future IceCube detector at the South Pole, will be able to determine the deposited energy with a precision comparable to the discussed Hyper-Kamiokande detector. The unique location has the advantage that with Super- or Hyper-Kamiokande as a co-detector the likelihood for encountering the required setup (exactly one line of sight through the earth)

is 70 %. If the earth-matter effect is detected we can infer the hierarchy of neutrino masses to be normal if $\sin^2\theta_{13} \gtrsim 10^{-3}$ is established by other experiments. For $\sin^2\theta_{13} \lesssim 10^{-3}$ the earth effect will always be present. In any case, a positive signal allows for strong conclusions whereas the reasons for a not observing an effect can either be due to smaller flux differences from the SN or oscillation parameters.

Our second proposed mechanism, namely identifying the earth effect at a single detector would, together with the first method, enhance the covered area of the sky to 85 %. A detector like the proposed Hyper-Kamiokande or a future large scintillation detector will record the neutrinos from a galactic SN with such a high accuracy that the Fourier transform of the inverse-energy spectrum can reveal modulations induced by the earth effect. It would even be possible to determine the solar mass splitting at the level of accuracy that will be reached by KamLAND.

These methods have the advantage of being independent of the exact original fluxes and spectra. We just assume that a difference between the $\bar{\nu}_\mathrm{e}$ and $\bar{\nu}_\mu$ fluxes is present. For the two-detector setup we propose to use the time variation of the flux difference as the observable in order to get rid of systematic uncertainties in the absolute detector normalization. This time dependence is found in all numerical simulations. The physical reason is that neutrino emission is first powered by the accretion of infalling material and later on by proto-neutron star cooling.

With this first systematic study of all relevant neutrino-matter interactions we were able to significantly improve the understanding of flavor-dependent SN neutrino emission. Our findings essentially mark a change of paradigm for oscillation studies involving SN neutrinos. The mean energies of ν_μ and $\bar{\nu}_\mathrm{e}$ are almost equal whereas the luminosities differ by up to a factor of 2, contrary to the previous paradigm. The new picture allows one to detect neutrino-oscillation effects, for example with two distant detectors by comparing the time variation of the deposited energy, or in a single detector by identifying the modulations of the spectrum with the help of a Fourier transform. These concepts rely on robust features of SN simulations instead of comparing predictions with measurements, like previous methods. The detection of a SN by itself will be a very valuable astrophysics observation and can additionally contribute to particle physics.

Appendix A

Abbreviations

ν_μ	—	unless specified differently, ν_μ stands for ν_μ, ν_τ, $\bar{\nu}_\mu$, and $\bar{\nu}_\tau$
$\bar{\nu}_\mu$	—	unless specified differently, $\bar{\nu}_\mu$ stands for $\bar{\nu}_\mu$ and $\bar{\nu}_\tau$
CM	—	center of momentum
LTE	—	local thermal equilibrium
$M_\odot$	—	solar mass
mfp	—	mean free path
SN	—	supernova
Y_e	—	electron fraction per baryon
Y_L	—	lepton fraction per baryon

Appendix B

Monte Carlo Code

B.1 General Concept

Our Monte Carlo code is based on that developed by Janka (1987) where a detailed description of the numerical aspects can be found. The code was first applied to calculations of neutrino transport in SNe by Janka & Hillebrandt (1989a,b) and Janka (1991). It uses Monte Carlo methods to follow the individual destinies of sample neutrinos (particle "packages" with suitably attributed weights to represent a number of real neutrinos) on their way through the star from the moment of creation or inflow to their absorption or escape through the inner or outer boundaries. The considered stellar background is assumed to be spherically symmetric and static, and the sample neutrinos are characterized by their weight factors and by continuous values of energy, radial position, and direction of motion, represented by the cosine of the angle relative to the radial direction. The rates of neutrino interactions with particles of the stellar medium can be evaluated by taking into account Fermion blocking effects according to the local phase-space distributions of neutrinos (Janka & Hillebrandt 1989b).

As background stellar models we use the ones described in Sec. 4.2. They are defined by radial profiles of the density ρ, temperature T, and electron fraction $Y_{\rm e}$, i.e. the number of electrons per baryon. The calculations span the range between some inner radius $R_{\rm in}$ and outer radius $R_{\rm out}$. These bound the computational domain which is divided into 30 equally spaced radial zones. In each zone ρ, T, and $Y_{\rm e}$ are taken to be constant. $R_{\rm in}$ is chosen at such high density and temperature that the neutrinos are in LTE in at least the first radial zone. $R_{\rm out}$ is placed in a region where the neutrinos essentially stream freely. At $R_{\rm in}$ neutrinos are injected isotropically according to LTE. While a small net flux across the inner boundary develops, the neutrinos emerging

from the star are generated almost exclusively within our computational domain. If $R_{\rm in}$ is chosen so deep that the neutrinos are in LTE, the assumed boundary condition for the flux will not affect the results.

The stellar medium is assumed to be in thermodynamic equilibrium with nuclei being completely disintegrated into free nucleons. Based on ρ, T, and $Y_{\rm e}$ we calculate all the required thermodynamic quantities, notably the number densities, chemical potentials, and temperatures of protons, neutrons, electrons, positrons, and the relevant neutrinos. Except for runs that include weak magnetism, the chemical potentials for ν_μ and ν_τ are taken to be zero. Next we compute the interaction rates in each radial zone for all included processes. In the simulations discussed in the present work, fermion phase-space blocking is calculated from the neutrino equilibrium distributions instead of the computed phase-space distributions. This simplification saves a lot of CPU time because otherwise the rates have to be re-evaluated whenever the distribution of neutrinos has changed after a transport time step. The approximation is justified because phase-space blocking is most important in regions where neutrinos frequently interact and thus are close to LTE. Test runs without this approximation show that the results are not affected within our numerical accuracy.

At the start of a Monte Carlo run, 800,000 test neutrinos are randomly distributed in the model according to the local equilibrium distributions. Each test neutrino represents a certain number of real neutrinos. In this initial setup the number of real neutrinos is determined by LTE. Then transport is started. The time step is fixed at $\Delta t = 10^{-7}$ s; recall that the interaction rates do not change. At the beginning of each step neutrino creation takes place. The number of test particles that can be created is given by the number of neutrinos that were lost through the inner and outer boundaries plus those absorbed by the medium. Based on Δt, the production rates, and the fact that the inner boundary radiates neutrinos, we calculate the number of neutrinos that are produced in one time step and distribute them among the available test neutrinos by attributing suitable weight factors. The sample particles are created within the medium or injected at the inner boundary in appropriate proportions.

During a time step the path of each test particle through the stellar atmosphere is followed by Monte Carlo sampling. With random numbers and stored tables of the total interaction rates we decide whether it flies freely or interacts. If it interacts it can scatter or it can be absorbed; in the last case we turn to the next particle. For scattering we determine the new momentum and position and the time of flight before the interaction took place and continue with the process until the time step is used up. Particles leaving through the lower or upper boundaries are eliminated from the transport.

After a certain number of time steps (typically around 15,000) the neutrino distribution reaches a stationary state and further changes occur only due to statistical fluctuations. At that stage we start averaging the output quantities over the next 500 time steps.

B.2 Structure of the Code

Thermodynamic Properties of the Medium For each radial zone the number of baryons is computed by the given medium density. Using the given temperature T and Y_e together with the number density of baryons n_B and the fact that electrons and positrons are in LTE we obtain the chemical potential of electrons and positrons by numerically solving Equation (4.4). With μ and T the number densities of electrons and positrons are calculated. In the same way the properties of protons and neutrons are determined.

Main Part: The Time-Step Loop The main part of the program consists of a loop that processes one time step after the other. Each timestep corresponds to 10^{-7}s of neutrino transport. Since we use blocking factors of neutrinos in LTE as an approximation to the real neutrino occupation, we only calculate the interaction rates in the first time step and store them in arrays. From these rates the cumulated probabilities are obtained. In the time-step loop specific rates are obtained from the arrays by linear interpolation.

Injection and Creation of Neutrinos In each time step the number of sample neutrinos that were absorbed or left the model through the inner or outer boundary during the preceding timestep is now available for injection at the inner boundary and emission events in the medium. According to the likelihood of each event these sample neutrinos are divided into one group that is injected at the inner boundary and various others that correspond to the creation mechanisms inside the medium. With the same likelihoods the number of real neutrinos that would be produced in the time step is calculated and equally distributed among the sample neutrinos as their weights. Neutrinos injected at the lower boundary get R_in as their radial position, a random energy according to the LTE distribution in the first cell, and an angle according to the distribution of neutrinos freely streaming off a sphere. The creation mechanisms inside the medium are the charged current interactions $\mathrm{e^-p} \rightarrow \nu_\mathrm{e}\mathrm{n}$ and $\mathrm{e^+n} \rightarrow \bar{\nu}_\mathrm{e}\mathrm{p}$ for ν_e and $\bar{\nu}_\mathrm{e}$, $\mathrm{e^+e^-} \rightarrow \nu\bar{\nu}$ for all flavors, and $\mathrm{NN} \rightarrow \mathrm{NN}\nu_\mu\bar{\nu}_\mu$, $\nu_\mathrm{e}\bar{\nu}_\mathrm{e} \rightarrow \nu_\mu\bar{\nu}_\mu$ for ν_μ. By Monte Carlo methods we obtain the radial position, energy, and angle versus the radial direction.

Transport After all new neutrinos are created transport starts. The number of neutrinos to be transported equals the number of neutrinos that remained in the star plus the injected and created neutrinos. The transport loop then takes one neutrino after the other through the star until their time is used up or they leave the model. Neutrinos that remained inside the model from the preceding timestep have the whole time $\Delta t = 10^{-7}$s. Since injected and created neutrinos appear at some random time their transport time step lasts only $r\Delta t$ where r is a uniformly distributed random number between 0 and 1. Then the time until the first interaction (T_{IA}) is obtained with the help of the highest total interaction rate for the energy of the transported neutrino. If T_{IA} lies outside Δt we store the neutrino properties after it freely traveled until the end of Δt and jump to the next one. If the interaction takes place within the available time we have to decide which interaction takes place. The interaction rates are also density dependent, i.e. for most locations inside the star we underestimated T_{IA} by using the upper limit of the total rate. Therefore, when deciding which interaction takes place one of the "interactions" leaves the neutrino properties unchanged and in fact is no interaction at all. This compensates for the too low estimate T_{IA} locally.

Before we go to the interaction we first calculate the new position of the neutrino at the point of interaction. If it leaves the model through the inner or outer boundary on its way to that point it is eliminated and we jump to the next one. In case it stays within the area of interest we use the interaction rates at the interaction point to decide which process takes place. Then according to that process the new energy and angle versus radial direction of the outgoing neutrino are determined and stored. If Δt is not used up we determine a new T_{IA} and go on until Δt is used up.

After all neutrinos used up their time or left the star we go over to the next time step.

Bibliography

J. Ahrens et al. [AMANDA Collaboration], 2002a,
"Search for supernova neutrino-bursts with the AMANDA detector,"
Astropart. Phys. **16** (2002) 345 [astro-ph/0105460].

J. Ahrens et al. [The IceCube Collaboration], 2002b,
"IceCube: The next generation neutrino telescope at the South Pole,"
astro-ph/0209556.

M. Apollonio et al. [CHOOZ Collaboration],
"Limits on neutrino oscillations from the CHOOZ experiment,"
Phys. Lett. B **466** (1999) 415 [hep-ex/9907037].

M. Apollonio et al., 2002,
"Oscillation physics with a neutrino factory,"
hep-ph/0210192.

J. N. Bahcall, M. C. Gonzalez-Garcia, and C. Peña-Garay,
"Solar neutrinos before and after KamLAND,"
JHEP **02**, 009 (2003) [hep-ph/0212147].

V. D. Barger, S. Geer, R. Raja, and K. Whisnant,
"Exploring neutrino oscillations with superbeams,"
Phys. Rev. D **63** (2001) 113011 [hep-ph/0012017].

V. Barger, D. Marfatia, and B. P. Wood,
"Inverting a supernova: Neutrino mixing, temperatures and binding energy,"
Phys. Lett. B **547** (2002) 37 [hep-ph/0112125].

J. F. Beacom, R. N. Boyd, and A. Mezzacappa,
"Black hole formation in core collapse supernovae and time-of-flight measurements of the neutrino masses,"
Phys. Rev. D **63** (2001) 073011 [astro-ph/0010398].

H. A. Bethe and J. R. Wilson,
"Revival Of A Stalled Supernova Shock By Neutrino Heating,"
Astrophys. J. **295** (1985) 14.

R. M. Bionta et al.,
"Observation Of A Neutrino Burst In Coincidence With Supernova Sn1987a In The Large Magellanic Cloud,"
Phys. Rev. Lett. **58** (1987) 1494.

S. W. Bruenn,
"Stellar Core Collapse: Numerical Model And Infall Epoch,"
Astrophys. J. Suppl. **58** (1985) 771.

S. W. Bruenn,
"Neutrinos From Sn1987a And Current Models Of Stellar Core Collapse,"
Phys. Rev. Lett. **59** (1987) 938.

S. W. Bruenn, A. Mezzacappa, and T. Dineva,
"Dynamic and diffusive instabilities in core collapse supernovae,"
Phys. Rept. **256** (1995) 69.

R. Buras, H. T. Janka, M. T. Keil, G. G. Raffelt, and M. Rampp, 2003a,
"Electron-neutrino pair annihilation: A new source for muon and tau neutrinos in supernovae,"
Astrophys. J. **587** (2003) 320 [astro-ph/0205006].

R. Buras, M. Rampp, H. T. Janka, and K. Kifonidis, 2003b,
"Improved Models of Stellar Core Collapse and Still no Explosions: What is Missing?,"
astro-ph/0303171.

A. Burrows,
"Convection and the mechanism of type II supernovae,"
Astrophys. J. **318** (1987) L57.

A. Burrows,
"Supernova Neutrinos,"
Astrophys. J. **334** (1988) 891.

A. Burrows and R. F. Sawyer,
"The effects of correlations on neutrino opacities in nuclear matter,"
Phys. Rev. C **58** (1998) 554 [astro-ph/9801082].

A. Burrows and R. F. Sawyer,
"Many-Body Corrections To Charged-Current Neutrino Absorption Rates In Nuclear Matter,"
Phys. Rev. C **59** (1999) 510 [astro-ph/9804264].

G. W. Carter and M. Prakash,
"The quenching of the axial coupling in nuclear and neutron-star matter,"
Phys. Lett. B **525** (2002) 249 [nucl-th/0106029].

A. Cervera, A. Donini, M. B. Gavela, J. J. Gomez Cadenas, P. Hernandez, O. Mena, and S. Rigolin,
"Golden measurements at a neutrino factory,"
Nucl. Phys. B **579** (2000) 17
Erratum-ibid. B **593** (2001) 731, [hep-ph/0002108].

S. H. Chiu and T. K. Kuo,
"Effects of neutrino temperatures and mass hierarchies on the detection of supernova neutrinos,"
Phys. Rev. D **61** (2000) 073015 [hep-ph/9909461].

A. S. Dighe and A. Y. Smirnov,
"Identifying the neutrino mass spectrum from the neutrino burst from a supernova,"
Phys. Rev. D **62** (2000) 033007 [hep-ph/9907423].

A. S. Dighe, 2001,
"Earth matter effects on the supernova neutrino spectra,"
hep-ph/0106325.

A. S. Dighe, M. T. Keil, and G. G. Raffelt, 2003a,
"Detecting the neutrino mass hierarchy with a supernova at IceCube,"
JCAP, in press (2003), hep-ph/0303210.

A. S. Dighe, M. T. Keil, and G. G. Raffelt, 2003b,
"Identifying earth matter effects on supernova neutrinos at a single detector,"
hep-ph/0304150.

G. Dutta, D. Indumathi, M. V. Murthy, and G. Rajasekaran,
"Neutrinos from stellar collapse: Comparison of the effects of three and four flavor mixings,"
Phys. Rev. D **62** (2000) 093014 [hep-ph/0006171].

G. L. Fogli, E. Lisi, A. Marrone, D. Montanino, A. Palazzo, and A. M. Rotunno,
"Solar neutrino oscillation parameters after first KamLAND results,"
hep-ph/0212127.

M. Freund, P. Huber and, M. Lindner,
"Systematic exploration of the neutrino factory parameter space including errors and correlations,"
Nucl. Phys. B **615** (2001) 331 [hep-ph/0105071].

G. M. Fuller, W. C. Haxton, and G. C. McLaughlin,
"Prospects for detecting supernova neutrino flavor oscillations,"
Phys. Rev. D **59** (1999) 085005 [astro-ph/9809164].

M. C. Gonzalez-Garcia and Y. Nir,
"Developments in neutrino physics,"
hep-ph/0202058.

A. de Gouvea and C. Peña-Garay,
"Solving the solar neutrino puzzle with KamLAND and solar data,"
Phys. Rev. D **64** (2001) 113011 [hep-ph/0107186].

F. Halzen, J. E. Jacobsen, and E. Zas,
"Possibility That High-Energy Neutrino Telescopes Could Detect Supernovae,"
Phys. Rev. D **49** (1994) 1758.

F. Halzen, J. E. Jacobsen, and E. Zas,
"Ultra-Transparent Antarctic Ice as a Supernova Detector,"
Phys. Rev. D **53** (1996) 7359 [astro-ph/9512080].

S. Hannestad and J. Madsen,
"Neutrino decoupling in the early universe,"
Phys. Rev. D **52** (1995) 1764 [astro-ph/9506015].

S. Hannestad and G. Raffelt,
"Supernova neutrino opacity from nucleon nucleon bremsstrahlung and related processes,"
Astrophys. J. **507** (1998) 339 [astro-ph/9711132].

M. Herant, S. A. Colgate, W. Benz, and C. Fryer,
"Neutrinos And Supernovae,"
Los Alamos Sci. **25** (1997) 164-179.

W. Hillebrandt, 1987,
"Stellar collapse and supernova explosions,"
in: "High Energy Phenomena around Collapsed Stars," Procs. NATO ASI, 2–13 Sept. 1985, Cargèse, Corsica, France, edited by D. Pacini (Reidel, Dordrecht), p. 73.

W. Hillebrandt and R. G. Wolff, 1985,
"Models of type II supernova explosions,"
in: Nucleosynthesis: Challenges and New Developments, edited by W.D. Arnett and J.W. Truran University of Chicago Press, Chicago, p. 131.

K. Hirata et al. [KAMIOKANDE-II Collaboration],
"Observation Of A Neutrino Burst From The Supernova Sn1987a,"
Phys. Rev. Lett. **58** (1987) 1490.

P. C. de Holanda and A. Y. Smirnov,
"LMA MSW solution of the solar neutrino problem and first KamLAND results,"
JCAP **02**, 001 (2003) [hep-ph/0212270].

C. J. Horowitz and G. Li,
"Charge-conjugation violating neutrino interactions in supernovae,"
Phys. Rev. D **61** (2000) 063002 [astro-ph/9908219].

C. J. Horowitz,
"Weak magnetism for antineutrinos in supernovae,"
Phys. Rev. D **65** (2002) 043001 [astro-ph/0109209].

P. Huber, M. Lindner, and W. Winter,
"Superbeams versus neutrino factories,"
Nucl. Phys. B **645** (2002) 3 [hep-ph/0204352].

P. Huber, M. Lindner, T. Schwetz, and W. Winter,
"Reactor neutrino experiments compared to superbeams,"
hep-ph/0303232.

H.-T. Janka, 1987,
"Monte-Carlo-Verfahren für den Neutrinotransport in Supernovae,"
Diploma Thesis, Technical University Munich

H.-T. Janka and W. Hillebrandt, 1989a,
"Neutrino emission from type II supernovae—an analysis of the spectra,"
Astron. Astrophys. **224** (1989) 49

H.-T. Janka and W. Hillebrandt, 1989b,
"Monte Carlo simulations of neutrino transport in type II supernovae,"
Astron. Astrophys. Suppl. Ser., **78** (1989) 375

H.-T. Janka, 1991,
"Neutrino transport in type-II supernovae and protoneutron stars by Monte Carlo Methods,"
Ph.D. Thesis, Technical University Munich, MPA-Report 587

H.-T. Janka, 1993,
"Neutrinos from type-II supernovae and the neutrino-driven supernova mechanism,"
in: Proc. Vulcano Workshop 1992 Frontier Objects in Astrophysics and Particle Physics, 18–23 May 1992, Vulcano, Italy, edited by F. Giovannelli and G. Mannocchi (Società Italiana di Fisica, Bologna), p. 345

H. T. Janka, W. Keil, G. Raffelt, and D. Seckel,
"Nucleon spin fluctuations and the supernova emission of neutrinos and axions,"
Phys. Rev. Lett. **76** (1996) 2621 [astro-ph/9507023].

H. T. Janka, R. Buras, K. Kifonidis, T. Plewa, and M. Rampp, 2002,
"Core Collapse and Then? The Route to Massive Star Explosions,"
astro-ph/0212316.

B. Jegerlehner, F. Neubig, and G. Raffelt,
"Neutrino Oscillations and the Supernova 1987A Signal,"
Phys. Rev. D **54** (1996) 1194 [astro-ph/9601111].

M. Kachelriess, A. Strumia, R. Tomas, and J. W. Valle,
"SN1987A and the status of oscillation solutions to the solar neutrino problem,"
Phys. Rev. D **65** (2002) 073016 [hep-ph/0108100].

M. T. Keil, G. G. Raffelt, and H. T. Janka, 2002,
"Monte Carlo study of supernova neutrino spectra formation,"
Astrophys. J. in press,
astro-ph/0208035.

W. Keil, H. T. Janka, and E. Müller,
"Ledoux-convection in protoneutron stars: A clue to supernova nucleosynthesis?,"
Astrophys. J. **473** (1996) L111 [astro-ph/9610203].

M. Liebendorfer, A. Mezzacappa, F. K. Thielemann, O. E. Messer, W. R. Hix, and S. W. Bruenn,
"Probing the gravitational well: No supernova explosion in spherical symmetry with general relativistic Boltzmann neutrino transport,"
Phys. Rev. D **63** (2001) 103004 [astro-ph/0006418].

C. Lunardini and A. Y. Smirnov, 2001a,
"Neutrinos from SN1987A, Earth matter effects and the LMA solution of the solar neutrino problem,"
Phys. Rev. D **63** (2001) 073009 [hep-ph/0009356].

C. Lunardini and A. Y. Smirnov, 2001b,
"Supernova neutrinos: Earth matter effects and neutrino mass spectrum,"
Nucl. Phys. B **616** (2001) 307 [hep-ph/0106149].

C. Lunardini and A. Y. Smirnov, 2003,
"Probing the neutrino mass hierarchy and the 13-mixing with supernovae,"
hep-ph/0302033.

R. Mayle, J. R. Wilson, and D. N. Schramm,
"Neutrinos From Gravitational Collapse,"
Astrophys. J. **318** (1987) 288.

R. Mayle, D. N. Schramm, M. S. Turner, and J. R. Wilson,
"Constraints on Dirac neutrinos from SN1987A,"
Phys. Lett. B **317** (1993) 119 [astro-ph/9301005].

A. Mezzacappa, A. C. Calder, S. W. Bruenn, J. M. Blondin, M. W. Guidry, M. R. Strayer, and A. S. Umar 1998a,
"The Interplay between ProtoNeutron Star Convection and Neutrino Transport in Core-Collapse Supernovae,"
Astrophys. J. **493** (1998) 848

A. Mezzacappa, M. Liebendorfer, O. E. Messer, W. R. Hix, F. K. Thielemann, and S. W. Bruenn,
"The Simulation of a Spherically Symmetric Supernova of a 13 Solar Mass Star with Boltzmann Neutrino Transport, and Its Implications for the Supernova Mechanism,"
Phys. Rev. Lett. **86** (2001) 1935 [astro-ph/0005366].

H. Minakata and H. Nunokawa,
"Inverted hierarchy of neutrino masses disfavored by supernova 1987A,"
Phys. Lett. B **504** (2001) 301 [hep-ph/0010240].

H. Minakata, H. Nunokawa, R. Tomas, and J. W. Valle,
"Probing supernova physics with neutrino oscillations,"
Phys. Lett. B **542** (2002) 239 [hep-ph/0112160].

E. S. Myra and A. Burrows,
"Neutrinos from type II supernovae: The first 100 milliseconds,"
Astrophys. J. **364**, (1990), 222

Nobel e-Museum, 2002,
Internet URL: http://www.nobel.se

J. A. Pons, S. Reddy, M. Prakash, J. M. Lattimer, and J. A. Miralles,
"Evolution of protoneutron stars,"
Astrophys. J. **513** (1999) 780 [astro-ph/9807040].

W. H. Press, S. A. Teukolsky, W. T. Vetterling, and B. P. Flannery, 1992,
"Numerical Recipes in Fortran 77," Second
Edition, Vol. 1, (Cambridge University Press)

G. G. Raffelt,
"Stars As Laboratories For Fundamental Physics: The Astrophysics Of Neutrinos, Axions, And Other Weakly Interacting Particles,"
Chicago, USA: Univ. Pr. (1996)

G. G. Raffelt,
"Particle physics from stars,"
Ann. Rev. Nucl. Part. Sci. **49** (1999) 163 [hep-ph/9903472].

G. G. Raffelt,
"Mu- And Tau-Neutrino Spectra Formation In Supernovae,"
Astrophys. J. **561** (2001) 890 [astro-ph/0105250].

G. G. Raffelt,
"Physics with supernovae,"
Nucl. Phys. Proc. Suppl. **110** (2002) 254 [hep-ph/0201099].

G. G. Raffelt, M. T. Keil, R. Buras, H. T. Janka, and M. Rampp, 2003,
"Supernova neutrinos: Flavor-dependent fluxes and spectra,"
astro-ph/0303226.

M. Rampp and H. T. Janka,
"Spherically symmetric simulation with Boltzmann neutrino transport of core collapse and post-bounce evolution of a 15 solar mass star,"
Astrophys. J. **539** (2000) L33 [astro-ph/0005438].

M. Rampp and H. T. Janka,
"Radiation hydrodynamics with neutrinos: Variable Eddington factor method for core-collapse supernova simulations,"
Astron. Astrophys. **396** (2002) 361 [astro-ph/0203101].

M. Rampp, R. Buras, H.-T. Janka, and G. Raffelt, 2002,
"Core-collapse supernova simulations: Variations of the input physics,"
in: Procs. 11th Workshop on Nuclear Astrophysics, Ringberg Castle, Tegernsee, Germany, Feb. 11–16, 2002, MPA-Report P13 (Max-Planck-Institut für Astrophysik, Garching), p. 119 [astro-ph/0203493]

S. Reddy, M. Prakash, and J. M. Lattimer,
"Neutrino interactions in hot and dense matter,"
Phys. Rev. D **58** (1998) 013009 [astro-ph/9710115].

S. Reddy, M. Prakash, J. M. Lattimer, and J. A. Pons,
"Effects of strong and electromagnetic correlations on neutrino interactions in dense matter,"
Phys. Rev. C **59** (1999) 2888 [astro-ph/9811294].

S.L. Shapiro, and S.A. Teukolsky,
"Black holes, white dwarfs and neutron stars: The physics of compact objects"
John Wiley & Sons, New York (1983)

A. Y. Smirnov, D. N. Spergel, and J. N. Bahcall,
"Is Large Lepton Mixing Excluded?,"
Phys. Rev. D **49** (1994) 1389 [hep-ph/9305204].

H. Suzuki, 1989,
"Neutrino burst from supernova explosion and proto neutron star cooling,"
Ph.D. Thesis, University of Tokyo

H. Suzuki,
"Neutrino emission from protoneutron star with modified Urca and nucleon bremsstrahlung processes,"
Num. Astrophys. Japan, **2**, (1991), 267

H. Suzuki, 1993,
"Supernova neutrinos—Multigroup simulations of neutrinos from protoneutron star,"
in: Proc. International Symposium on Neutrino Astrophysics: Frontiers of Neutrino Astrophysics, 19–22 Oct. 1992, Takayama, Japan, edited by Y. Suzuki and K. Nakamura (Universal Academy Press, Tokyo)

K. Takahashi and K. Sato,
"Earth effects on supernova neutrinos and their implications for neutrino parameters,"
Phys. Rev. D **66** (2002) 033006 [hep-ph/0110105].

K. Takahashi, M. F. E. El Eid, and W. Hillebrandt,
"Beta transition rates in hot and dense matter,"
Astron. Astrophys. **67**, (1978), 185

T. A. Thompson, A. Burrows, and J. E. Horvath,
"Mu and tau neutrino thermalization and production in supernovae: Processes and timescales,"
Phys. Rev. C **62** (2000) 035802 [astro-ph/0003054].

T. A. Thompson, A. Burrows, and P. A. Pinto, 2002,
"Shock breakout in core-collapse supernovae and its neutrino signature,"
astro-ph/0211194.

T. Totani, K. Sato, H. E. Dalhed, and J. R. Wilson,
"Future detection of supernova neutrino burst and explosion mechanism,"
Astrophys. J. **496** (1998) 216 [astro-ph/9710203].

D. L. Tubbs and D. N. Schramm,
"Neutrino Opacities At High Temperatures And Densities,"
Astrophys. J. **201** (1975) 467.

P. Vogel and J. F. Beacom,
"The angular distribution of the reaction anti-nu/e + p $\rightarrow$ e+ + n,"
Phys. Rev. D **60** (1999) 053003 [hep-ph/9903554].

J. R. Wilson, 1985,
in Numerical Astrophysics, ed. J. M. Centrella, J. M. LeBlanc, & R. L. Bowers (Jones and Bartlett Publ., Boston), 422.

J. R. Wilson and R. W. Mayle,
"Convection in core collapse supernovae,"
Phys. Rept. **163** (1988) 63.

J. R. Wilson and R. W. Mayle,
"Report On The Progress Of Supernova Research By The Livermore Group,"
Phys. Rept. **227** (1993) 97.

W. R. Yueh and J. R. Buchler, 1976a,
"Scattering functions for neutrino transport,"
Astrophys. Space Sci. , **39**, (1976), 429.

W. R. Yueh and J. R. Buchler, 1976b,
"Neutrino Processes in Dense Matter,"
Astrophys. Space Sci. , **41**, (1976), 221.